Vrije Universiteit Brussel

FACULTEIT INGENIEURSWETENSCHAPPEN

Experimental study of organ pipe behavior using optical measurement techniques

Greet Van de Perre

Promotor: Steve Vanlanduit

Abstract

Sound production in organ pipes is a complex matter, which has not entirely been understood until now. Even today, the craftsmanship of organ building is mainly characterized by tradition and experience. However, a better understanding of the physics of the sound production would allow organ builders to produce a pipe with a desired sound character in a more efficient way.

Because of their non-intrusive character, optical measurement techniques are ideally suited for the study of the flow behavior in organ pipes. Furthermore, the use of a camera with a high temporal resolution allows the analysis of the highly transient phenomena, rather than focusing on one single snapshot. In literature, especially the Schlieren technique has shown to be a good method to visualize the flow in the pipe mouth. In this thesis, the theory behind this technique was studied, followed by the design of such a configuration. A performance analysis was made, in order to maximize the quality of the obtained image. This configuration was then used to visualize the flow in the mouth of an organ pipe. Both the transient state, which includes the sound initiation, and the so-called quasi steady state, characterized by a steady speaking pipe, were considered. Measurements were performed for different mouth geometries, wherefore the emitted sound spectrum was previously determined by means of acoustical measurements. Similar results as previously published in literature were found.

To study the advantages and disadvantages of different optical techniques for this application, similar measurements were performed using the Particle Image Velocimetry (PIV), and, in a non-classical way, the Laser Doppler Vibrometry (LDV) technique. The PIV technique showed to be a good visualization technique only for the very first moments of jet formation, while the LDV technique provided interesting images for the whole time period, for both the pipe mouth and the resonator.

Samenvatting

Geluidsproductie in orgelpijpen is een complex gegeven, dat tot op vandaag nog niet volledig is begrepen. Het vervaardigen van orgelpijpen is nog steeds hoofdzakelijk gebaseerd op traditie en ervaring. Nochtans zou een beter inzicht in de fysische processen gerelateerd aan de geluidsproductie orgelbouwers toelaten om op een efficiëntere manier een pijp met een welbepaalde klankkleur te vervaardigen.

Optische meettechnieken zijn, omwille van het feit dat ze de stroming niet beïnvloeden, ideaal voor het bestuderen van het stromingsgedrag in orgelpijpen. Het gebruik van een camera met hoge tijdsresolutie laat bovendien toe om de hoog transiënte verschijnselen te bestuderen, terwijl andere meettechnieken eerder een momentopname zouden vastleggen. In de literatuur wordt vooral de Schlieren techniek vermeld als goede visualisatie methode voor deze toepassing. Deze techniek werd grondig bestudeerd, en een Schlieren meetopstelling werd gebouwd. Een performantie analyse liet toe de kwaliteit van de verkregen beelden op punt te stellen. Deze opstelling werd vervolgens gebruikt om de stroming in de mond van een orgelpijp te visualiseren, waarbij zowel de initiële transiënt als het stationaire gedrag werd bestudeerd. Deze metingen werden uitgevoerd voor verschillende mond geometrieën, waarvoor het uitgestraalde geluidsspectrum voordien werd onderzocht door middel van akoestische metingen. De bekomen resultaten zijn vergelijkbaar met deze gepubliceerd in de literatuur.

Omdat elke meettechniek is gekarakteriseerd door voor- en nadelen, werden gelijkaardige metingen uitgevoerd met de Particle Image Velocimetry (PIV) en, op een eerder onconventionele manier, met de Laser Doppler Vibrometry (LDV) techniek. Interessante beelden werden met de PIV techniek enkel verkregen voor de eerste momenten in de ontwikkeling van de jet, terwijl de LDV techniek een goede methode bleek voor het visualiseren van de gehele tijdsperiode, voor zowel de pijpmond als de resonator.

Résumé

La production de son dans les tuyaux de l'orgue est un phénomène complexe qui, jusqu'à aujourd'hui, n'a pas encore été complètement compris. La fabrication de ces tuyaux se fait encore par expérience et par tradition. Toutefois, une meilleure compréhension des phénomènes physiques relatés à la production du son permettrait aux constructeurs de dimensionner des pipes plus efficaces et de moduler plus précisément le timbre souhaité.

Parce que les techniques optiques sont non-destructives, elles conviennent parfaitement pour étudier les flux d'air dans les tuyaux d'orgue. Par ailleurs, l'utilisation d'un camera à haute résolution temporelle permet d'étudier les comportements transitoires, contrairement à d'autres techniques de mesure qui saisiraient plutôt une prise momentanée. Dans la littérature, c'est surtout la strioscopie qui est mentionnée comme technique de visualisation la plus appropriée pour cette application. Dans cette thèse, les aspects théoriques de cette technique ont été étudiés, et un dispositif de mesure a été construit. Une analyse de performance a permis d'optimiser la qualité des images obtenues à l'écran. Ce dispositif a ensuite été utilisé pour visualiser le flux dans la bouche d'un tuyau d'orgue. Tant le comportement initial transitoire que l'état stationnaire ont ainsi été étudiés. Ces mesures ont été réalisées pour des géométries de bouche différentes, dont le spectre acoustique avait été préalablement caractérisé par des mesures acoustiques. Les résultats obtenus sont similaires à ceux publiés dans la littérature.

Parce que chaque technique de mesure est caractérisée par des avantages et désavantages, des mesures semblables ont été réalisées par Particle Image Velocimetry (PIV) ainsi que, d'une façon plutôt inconventionnelle, avec la technique Laser Doppler Vibrometry (LDV). La technique PIV a produit de bons résultats seulement durant les premiers instants du développement du flux, tandis que la technique LDV s'est avérée être une bonne méthode pour la visualisation durant toute la période, aussi bien pour la bouche du tuyau que pour la partie résonante.

Prologue

Music has been an important part of life since thousands of years. The oldest known musical instrument dates back to approximately 40 000 BC, while singing is supposed to exist even longer. Despite this long existence, a lot of phenomena concerning the sound production in musical instruments are not clarified yet. Therefore, several people, both academici and music-lovers, are doing research on that topic. Jean-Paul De Greef is one of them; as builder of both house- and church organs, he is interested in the fact, how an organ pipe actually produces sound. After performing a lot of research himself, he carried this question to the Vrije Universiteit Brussel.

I myself have always been interested in music. Since I was little, I have played the violin and the piano, and joined several orchestras. As subject for my final year dissertation, I initially chose to work on the Schlieren technique. The fact of making invisible things like shock waves and airflows visible, really appealed to me. Since I was still looking for an application to apply my designed Schlieren configuration to, the choice of taking a closer look on organ pipe behavior was easily done.

Therefore, I would like to thank Mr. De Greef, for giving this interesting twist to my thesis, and providing me the information of his research. Of course, many thanks to my promoter, Prof. dr. Vanlanduit, for all the help and guidance. For the Schlieren and PIV experiments, I could always count on the help of Alexandru Nila; thank you for all the problem solving and tips you gave me. Thanks to Bart Ribbens of the Artesis Hogeschool Antwerpen, for providing the parabolic mirrors required for the Schlieren configuration, and Prof. dr. ir. Hirschberg, for the time he spent discussing my measurements. Finally, I should not forget to thank Jean-Paul Schepens and Alain Wery, for all the help with the practical aspects of performing experiments, and Stijn De Grijse, for the construction of my Plexiglas organ pipe; without it not much would have been measured.

Table of contents

List of figures

List of tables

List of symbols

Symbol	Definition	SI unit
λ_s	Wavelength of the standing wave	m
f_s	Frequency of the standing wave	Hz
T_s	Period of the standing wave	s
v	Phase speed of the wave	m/s
L	Length of the resonator	m
h	Flue height	m
b	Mouth width	m
θ	Labium angle	°
z	Transversal wedge offset	m
v_j	Jet velocity	m/s
n	Index of refraction	/
c	Speed of light	m/s
ρ	Density	kg/m^3
ε	Angle of ray deflection	°
m	Magnification	/
B	Luminance of the light source	cd/m^2
E	Illuminance on the screen	lux
D	Diameter light source	m
λ_l	Wavelength of the illuminating light	m
f_l	Frequency of the illuminating light	Hz
D_{cc}	Diameter of confusion	m
a	Unobstructed source height in the cutoff plane	m
Δa	Displacement of the light source in the cutoff plane	m
f_i	Focal length of the i-th field mirror	m
h_s	Source slit height	m
b_s	Source slit width	m
g	Distance Schlieren object - screen	m
S	Sensitivity	/
C	Contrast	/

1   Introduction

Until now, the mechanisms of sound production in organ pipes are not completely understood. The craftsmanship of organ building is more characterized by tradition and experience than by physical knowledge. A lot of research is being done on this topic, because a better understanding of the physics of the sound production would allow organ builders to dimension the pipes in advance, and reach a desired sound character without extensive trial and error. [1], [2]

In the nineteenth century, both Helmholtz [3] and Rayleigh [4] investigated the mechanism of organ pipe sound generation. Both formulated statements about the interaction of the jet with the resonator, but Rayleigh concluded that for fuller explanations, a better knowledge of jet mechanics was needed. A lot of research has been done on the edgetone phenomenon by, amongst others, Brown [5], [6] and Powell [7], [8]. A conceptual model of the organ pipe was developed by Cremer [9], Ising [10] and Bechert [11], and later by Coltman [12], who disagreed on the findings of the aforementioned. Further development of these models was done by Elder [13] and Fletcher [14]. Fabre [15], Verge [16] and Dequand [17] all devoted a PhD on the aeroacoustics in recorder-like instruments and contributed, in close collaboration with Hirschberg, to the improvement of the modeling of organ pipes.

The initial development of the flow, called the attack transient, has shown to be very important in the subjective perception of a sound. Therefore, the characteristics of the attack transient were intensively investigated, not only by Verge [16], [18], but also by Fletcher [19] and Paál, Angster and Miklós [1], [20]. In many cases, the Schlieren technique was used for the visualization of the jet development. Laser-Doppler Anemometry measurements were performed by Paál, Angster and Miklós [1] to obtain velocity data.

As soon as quasi steady oscillations are generated in the pipe mouth, the quasi steady state is set in. The flow behavior in this part of the sound was also a subject of extensive research. Dequand et al. [21] performed acoustic measurements to analyze the influence of the mouth geometry on the produced sound. Stereoscopic Particle Image Velocimetry was used by Johansson [22] for the determination of the velocity field at the exterior of the pipe mouth. And as for the transient state, the Schlieren technique has shown to be a suitable method to visualize the flow in the pipe mouth by several researchers.

This thesis focuses on the use of the Schlieren technique for the visualization of the flow in the pipe mouth of a flue organ pipe. In the next chapter, the fundamental principles of sound production in such pipes are discussed. As the sound is produced by the interaction of a jet-edge system with a resonator, these two components were first studied separately, followed by a discussion of the complete system. The third chapter describes the theory behind the different Shadowgraph and Schlieren techniques, while the fourth chapter illustrates the practical considerations to be taken into account when setting up a Schlieren measurement configuration. The Schadowgraph technique is closely related to the Schlieren technique, but requires less optical components and is easier to set up. Therefore, in order to get acquainted with this kind of optical measurements, first the Shadowgraph technique was discussed and experimentally tested. However, the organ pipe measurements were performed using the Schlieren technique, since it produces more sensitive images. Chapter four contains the results of the visualization of a classic Schlieren object, namely the flow above a candle, measured with each of the techniques discussed in the previous chapter. The influence of the components and their positions on the obtained image was analyzed, in order to maximize the quality of it. All this practical experience was taken into account when setting up the configuration for the organ pipe measurements, which are discussed in chapter five. This chapter contains the reenactment of a selection of measurements, published in the literature summarized above, next to a new input in the investment of flow visualization in organ pipes. A representative transparent organ pipe was made of Plexiglas. First of all, acoustic measurements were performed to characterize the produced sound. Hereby, the influence of the blowing pressure and mouth geometry on the sound spectrum was investigated. In what follows, both the attack transient and the quasi steady state are analyzed using the Schlieren technique. Also here, the effect of the mouth geometry was considered. Because every measuring technique has its advantages and disadvantages, similar measurements were performed using the Particle Image Velocimetry and the Laser Doppler Vibrometry. Application of this last technique for the visualization of the flow in the mouth of the organ pipe was not published in literature before, and therefore, this thesis proposes a new way to investigate the organ pipe behavior. The results of each of the three optical techniques were compared and the

benefits were highlighted. Because the flow behavior is better observable on moving images than on separate, stationary pictures, a CD containing al discussed Schlieren and PIV measurements was added. The exact content of this CD is listed in Appendix B. Chapter six concludes this thesis, by means of an overview of the performed study, measurements and findings. Because a knowledge of optical components, and the possible aberrations occurring in optical systems, is indispensible when using the Schlieren technique, an appendix on geometric optical optics is included (Appendix A).

2 Sound production in organ pipes
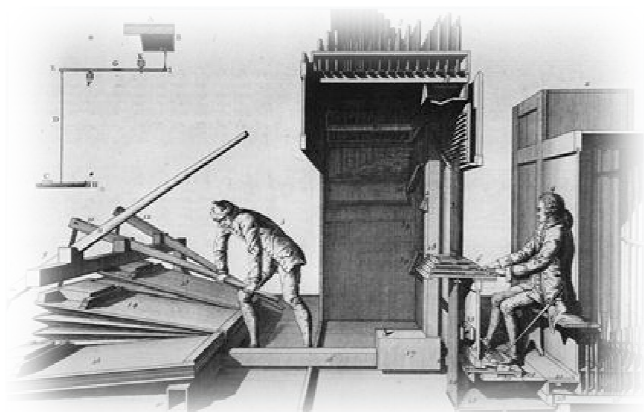
2.1   Introduction

The pipe organ produces sound by driving pressurized air through one or more pipes, selected by a keyboard. Unlike similar wind instruments as the recorder or the traverse flute, no holes are provided, so each organ pipe produces one single pitch. Two kinds of organ pipes exist: the reed pipe (Figure 1) and the flue pipe (Figure 2). In the former case, an airflow emerging from the tip of the pipe makes a brass reed vibrate. This reed is clamped to a so called shallot by a tuning wire at a certain location in order to achieve the desired vibration frequency. The produced sound is then amplified by the upper part of the pipe, serving as a resonator. This study however focuses on latter type of pipes. A flue pipe produces sound in a similar way as the recorder or transverse flute; pressurized air driven through a flue in the foot of the pipe, hits a wedge (called the labium or lip) and causes the air in the pipe to resonate. Thus in contrast to the reed pipes, a flue pipe does not contain any moving parts.
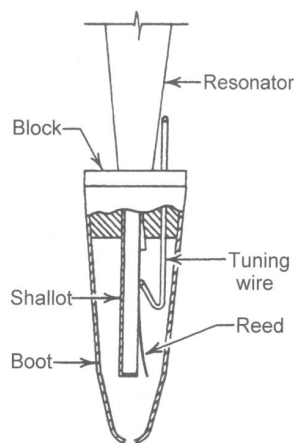
Figure 1: Configuration of the reed pipe. Sound is produced through the vibration of a reed, which can be tuned by adjusting the clamping of the reed between the shallot and tuning wire. [23]
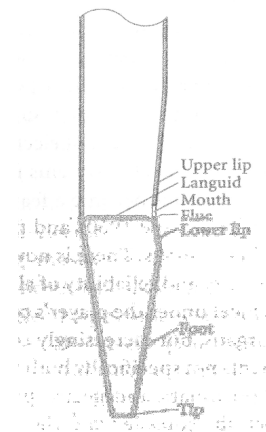
Figure 2: Configuration of the flue pipe. Sound production is achieved by the interaction of an airflow, emerging from the tip of the pipe, with the upper lip. [24]

A particularity of the organ is the ability of playing in different timbres. Timbre, also called tone quality or color, is the characteristic of a tone, which makes it possible to distinguish different types of sound production and thus different musical instruments. The timbre of a sound is a function of the nature and relative strength of the different frequencies composing the sound, and the envelope of the sound. It has been shown that especially the attack is determining in the characteristic perception of the sound. By adjusting the dimensions of the pipes and the mouth configuration, different sound spectra, and thus different tone qualities are reached. Next to the dimensions, also the used materials are important for the tone quality. Since the development of the organ in the middle ages, the most common materials are wood and amalgams of tin and lead. By playing on the exact composition of the amalgam or the exact type of wood, different timbres can be produced. A series of pipes producing the same tone quality for each note is called a rank. The rank is mostly named after the instrument it imitates; flue pipes are often classified as flute, principal or string, while reed pipes include the trumpet, bassoon, fagot and oboe. [24]

2.2   Mechanisms of sound production in flue organ pipes

2.2.1   Air column vibrations

Sound is produced when air or another compressible medium is excited by a mechanical incentive. The sound waves, resulting from this mechanical excitation, are fluctuations in pressure with respect to the atmospheric pressure. In gases, plasma's and liquid, these waves are longitudinal waves, causing local regions of compressions and rarefactions. Like light waves, sound can be reflected, refracted or attenuated by the medium. [25], [26]

Two types of musically interesting pipes exist: the open pipe, having two free boundaries, and the stopped pipe, where the upper end is closed. Now, when a wave, travelling in a stopped pipe, is reflected by the closed end, it interferes constructively with the incident wave, resulting in a standing wave consisting of pressure nodes and antinodes. The reflected wave will not be inverted: a compression will be reflected as a compression. In the case of an open end, the sound wave will also be reflected and create a standing wave. But in this case, the reflected wave is inverted. When a rarefaction, propagating along the tube, reaches the open end at atmospheric pressure, air is sucked into the pipe because of the pressure difference. This process stops when the open end is restored to the ambient pressure. However, the sucked air molecules move into the tube because of their inertia, and squeeze the present molecules. The rarefaction is thus converted to a compression by 'reflection'. [27]

Instead of talking in pressure nodes and antinodes, also the displacements can be considered. At a closed end, the displacement of the air particles is blocked, resulting in displacement node. On the contrary, at an open end, the pressure will take the value of the surrounding pressure, resulting in a pressure node, or equivalently, a displacement antinode. Because of these constraints, it is easily to see that for an open pipe, the simplest standing wave, i.e. the fundamental, first harmonic will be the one with a wavelength $\lambda_s = 2L$, where L is the length of the resonator (Table 1 and Figure 3 (a)). Also other standing waves, called the resonant modes are possible. As shown in the table, both the even and odd harmonics are included in the spectrum.

| First harmonic | Second harmonic | Third harmonic | | First harmonic | Third harmonic | Fifth harmonic |

(a) (b)
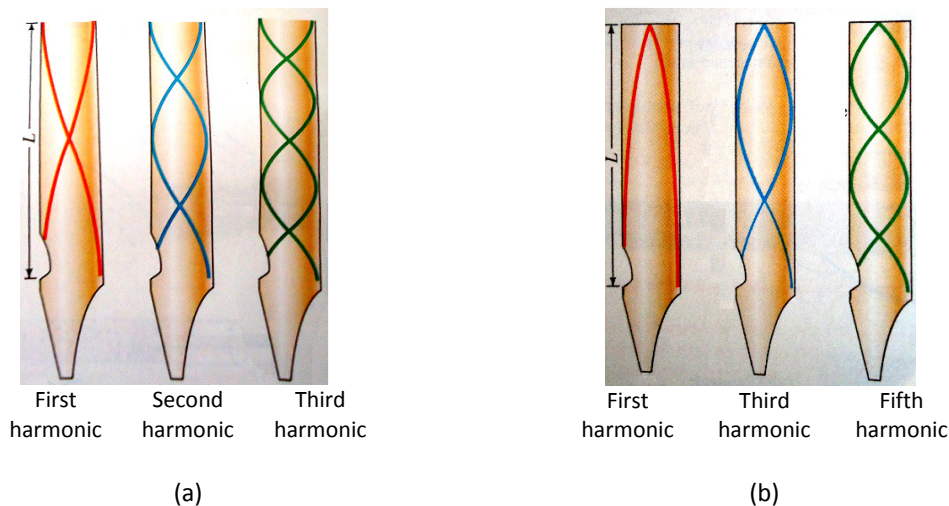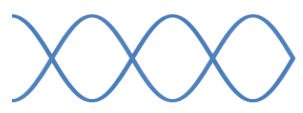
Figure 3: Different modes occurring in (a) open pipes and (b) stopped pipes. [28]

Table 1: Different modes occurring in open organ pipes.

Waveform (displacement)	Number of nodes	Wavelength	Frequency	Name (harmonic)	Name (overtone)
	1 node	$\lambda_s = 2L$	$f_s = 1\dfrac{v}{2L}$	First harmonic	Fundamental tone
	2 nodes	$\lambda_s = L$	$f_s = 2\dfrac{v}{2L}$	Second harmonic	First overtone
	3 nodes	$\lambda_s = \dfrac{2}{3}L$	$f_s = 3\dfrac{v}{2L}$	Third harmonic	Second overtone
	4 nodes	$\lambda_x = \dfrac{1}{2}L$	$f_s = 4\dfrac{v}{2L}$	Fourth harmonic	Third overtone

In the case of a stopped pipe, things are quite different. The fundamental first harmonic will have a wavelength $\lambda_s = 4L$ (Figure 3 (b)). Therefore, the stopped pipe will sound one octave lower than an open pipe with the same resonator length. Furthermore, the spectrum of the stopped pipe consists only of the fundamental and the odd harmonics (Table 2). The timbre of the sound produced will thus be less bright than in the case of the open pipe. [24],[28]

Table 2: Different modes occurring in stopped organ pipes.

Waveform (displacement)	Number of nodes	Wavelength	Frequency	Name (harmonic)	Name (overtone)
	1 node	$\lambda_s = 4L$	$f_s = 1\dfrac{v}{4L}$	First harmonic	Fundamental tone
	2 nodes	$\lambda_s = \dfrac{4}{3}L$	$f_s = 3\dfrac{v}{4L}$	Third harmonic	First overtone
	3 nodes	$\lambda_s = \dfrac{4}{5}L$	$f_s = 5\dfrac{v}{4L}$	Fifth harmonic	Second overtone
	4 nodes	$\lambda_s = \dfrac{4}{7}L$	$f_s = 7\dfrac{v}{4L}$	Seventh harmonic	Third overtone

2.2.2   Edgetones

In order to produce sound, a wind instrument has to be equipped with a mechanism for converting energy of a steady flow of air into energy of air vibrations. Three kinds of instable fluid flows give rise to sound: a simple fluid jet, a jet hitting an edge, and a jet controlled by a resonator. This last one represents the mechanism of the organ pipe and is considered in the next paragraph. However, to get a better understanding of this, first the other two mechanisms are introduced.

A simple jet of fluid, emerging into a region filled with similar fluid, can produce sound if its velocity is high enough. The stream will become turbulent, creating non-periodic disturbances. Such a jet thus creates broadband noise and has no definite pitch. Small amounts of this noise are present in the sound produced by an organ pipe.
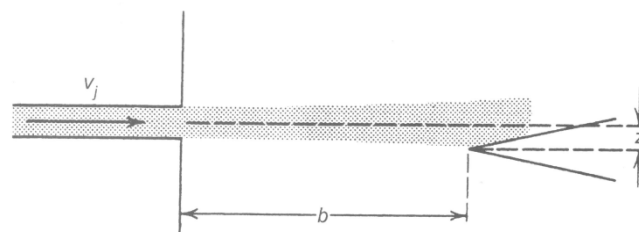
Figure 4: Pressurized air with an average speed v_j emerging from a flue crosses a gap of length b and hits a wedge to produce an edgtone. The wedge can have an offset z from the centerline of the jet, which influences the sound quality. [23]

When a sharp edge is placed in the path of a thin sheet of air emerging from a narrow slit (Figure 4), called a flue, much stronger vibrations are present. The vibrations are concentrated around one certain frequency and thus, a sound with a more or less perception of pitch, called the edgetone, is generated. The placement of the edge with respect to the centerline, the offset z, is critical for the tone quality, whereas the jet velocity v_j and the gap size b determine the pitch. This dependency is shown in Figure 5.

For a given gap size, increasing the jet velocity increases the frequency of the edge tone. However, this is not a continuous function. For some speeds, the edgetone may operate in stages of different frequencies. Sudden jumps between stages occur, and are indicated by arrows on the graph. For a given jet speed, increasing the gap distance b lowers the edgetone frequency. Again, the frequency may jump suddenly to a different value for certain values of the gap size. In musical applications, only the first of these stages are encountered.

(a)

(b)
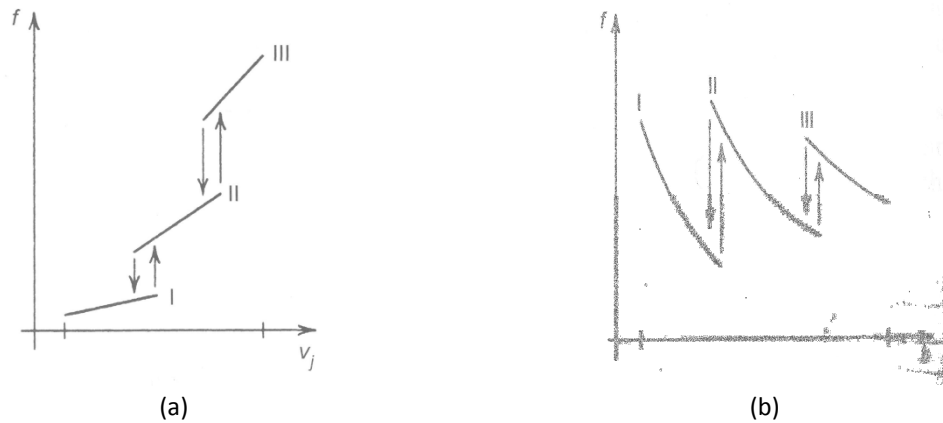
Figure 5: Dependency of the edgetone frequency on the jet speed (a) and gap distance (b).
For some speeds and distances, the edgetone operates in stages of different frequencies. Sudden jumps between the stages are indicated by arrows. [23]

The edgetone jet behavior is a difficult matter in fluid mechanics, on which experts are still not fully agreed. Some sources pose that an alternating series of vortices is formed ahead of the edge (Figure 6 (a)). The interaction of these vortices with the edge ensures the continued formation of new vortices, whereby an edgetone is maintained. Other sources, supported by experiments, point that, in order to produce an edgetone, the instability does not have to be so fully developed. The jet only has to wave back and forth slightly, in order to deliver air alternately above and below the edge (Figure 6 (b)).

(a)

(b)
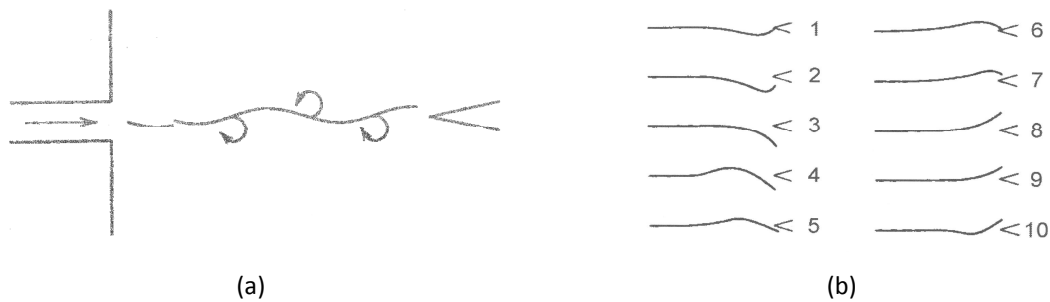
Figure 6: (a) According to some sources, an edgetone is generated by the interaction of a series of vortices with the edge. (b) Other sources pose that it is only necessary for the jet to wave back and forth slightly. [23]

When the jet flows below the edge, a higher fluid pressure is generated than above it. Therefore, other fluid is forced to move out, and a part of it flows through the gap between the flue and the edge. It pushes the fluid emerging from the slit upward, making it flow above the edge instead of below it after a while. The same process is then repeated in the other direction, leading to a periodic oscillation. The generation of an edgetone is thus a positive feedback mechanism. The frequency of the oscillation is determined by the speed at which the disturbance travels across the gap, which is approximately $0.4v_j$. Half the period of oscillation must equal the time it takes to travel a distance b at a velocity $0.4v_j$. Therefore, the frequency of oscillation can be calculated as follows:

$$\frac{T_o}{2} = \frac{b}{0.4v_j} \; or \; f_o = \frac{1}{T_o} = \frac{0.2v_j}{b} \tag{2.1}$$

Equation 2.1 represents the first stage in Figure 5. The other stages arise from the possibility that the jet disturbance could take one and a half (Figure 7 (b)) or two and a half periods (Figure 7 (c)) to cross the gap instead of only one half. Intermediate frequencies are not possible, since then negative feedback will occur instead of positive feedback. In such cases, the disturbance would arrive half a period too late, pushing the jet in the opposite direction, and thus suppressing the oscillations. [23]
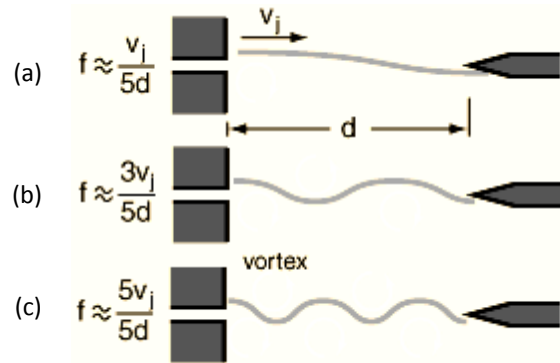
Figure 7: The frequency of oscillation depends on the time it takes for the disturbance to cross the gap. Positive feedback is established for (a) half a period, (b) one and a half period, (c) two and a half period. [29]

2.2.3   Organ pipe behavior

In a flue organ pipe, the edge system is extended with a resonator. This resonator has a strong control over the edgetone, making the whole system sound at a lower frequency than the isolated edgetone would do. This is achieved by the feedback mechanism of the pipe itself; a wave travelling in the pipe will be reflected at the end and disturb the jet upon its return. [23]. The exact nature of this interaction is up to now far from clear. The way the resonator is excited and the interaction mechanism of the acoustic wave emitted from the resonator and the jet both remain a subject for intensive research. [1]
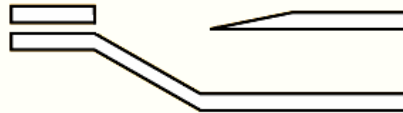
Figure 8: The combined flue-labium-resonator system. [29]

Consider Figure 8, where a resonator is added to the edge system. When the jet is switched from the outside to the inside of the edge, a positive pressure pulse is initiated in the pipe. In the case of a stopped pipe, this compression is reflected at the end, and tries to push the jet upwards when it returns to the mouth. Therefore, a self-sustained oscillation is reached if the pulse travel time is one half of the period of the jet oscillation, thus:

$$\frac{2L}{v} = \frac{T_o}{2} \text{ or } T_o = \frac{4L}{v}$$

(2.2)

As shown in Table 2, this is exactly the period of the fundamental mode of the stopped pipe.

As mentioned in paragraph 2.2.1, in the case of an open pipe, the positive pressure pulse is reflected to a negative pulse. Therefore, when the pulse has reached the mouth again, it will try to pull the jet inside again. A self-sustained oscillation will be reached when the travel time is one full period of jet oscillation:

$$T_o = \frac{2L}{v}$$

(2.3)

Again, this corresponds to the fundamental mode of the pipe (Table 1).

When the jet velocity is too large or the gap distance too small, so that the edgetone would prefer a much higher frequency, the second or third pipe mode may drive the feedback. A sound with higher pitch is then produced. This is called overblowing the pipe.

Even when the jet oscillates at the pipe's fundamental frequency, it may also receive positive feedback from the higher modes. Therefore, the resulting sound waves are not sinusoidal, but contain also higher frequency components. It is observed that, when pipe resonance is strongest and fully controls the jet motion, the jet disturbances travel from across the gap in about a quarter of a period, instead of a half in the case of a free edge:

$$\frac{T_o}{4} = \frac{b}{0.4 v_j} \; or \; f_o = \frac{1}{T_o} = \frac{0.1 v_j}{b} \tag{2.4}$$

Thus, the mouth of the pipe should be designed so that its edgetone sounds an octave higher than the desired note to be played by the pipe as a whole. [23]

The amount at which the different frequency components are present, and thus the sound quality, is strongly dependent of the dimensions of the pipe, as already mentioned in paragraph 2.1. The first important factor is the cross section of the pipe. Small pipes produce more harmonics and therefore a brighter sound than broader pipes. The reason for that can be found in the fact that the natural frequencies of a pipe do not coincidence exactly with the emitted frequencies under forced excitation. While the latter are exact multiples of the fundamental frequency, the natural frequencies will show a successively greater divergence from the multiples. This is due to end corrections that have to be made, which are larger for lower frequencies, and wider pipes. The oscillation of the jet around the labium is highly non-linear, and periodic with the fundamental frequency of the pipe. It will be the natural frequencies of the pipe, which will amplify the corresponding forced harmonics of the oscillating jet; the overtones will be accurately harmonic, and locked in both phase and frequency to the fundamental. This mode locking is only possible if the corresponding frequencies approximate each other quite well. Since the natural harmonics of a wide pipe do not coincide well with the harmonics present under forced excitation, the pipe will not amplify the latter in large amount. Therefore, the sound spectrum of such pipes is mostly restricted to the fundamental and the first few harmonics. [30], [31]. Organ pipes are also very sensitive to small adjustments of their mouth configuration; both the flue height and the gap size (called the mouth width) are determinative for the sound quality. These influences will be experimentally studied in chapter 5.

2.3   Techniques suited for studying sound production in organ pipes

The mechanism of sound production in organ pipes relies on the behavior and interactions of the air driven through the pipe. Because of its colorless, transparent and non-luminous character, this phenomenon cannot be observed by direct visual or photographic methods. In science and engineering, similar problems are often encountered. Just think about the airflow around an aircraft wing, the mixing of gasses, or convection problems. These phenomena can however be revealed by using an appropriate optical technique. Several techniques exist, each based on a specific physical effect. Table 3 shows a number of common optical techniques.

Most of these techniques exist for a long time, but due to recent developments, they have gained more interest during the last years. The improvements in laser, detector, optical fiber and computer technology made optical measurements a suitable technique in the analysis of phenomena in heat- and mass-transfer. The most important advantage of optical measurements is that they are non-intrusive, and therefore do not influence the investigated process. Furthermore, even highly transient phenomena can be analyzed, using a camera with a high temporal resolution. [32], [33]

Table 3: Common optical measurement techniques, suitable for the study of the flow behavior in organ pipes. Techniques indicated by an * are discussed in this thesis. [32]

Measuring technique	Physical effect	Application	Dimension
Schlieren and Shadowgraphy*	Light deflection	Heat, mass-transfer	2D
Holography	Holograpy	Particle size, velocity	3D
Interferometry	Change of light velocity	Heat, mass-transfer	2D
Laser Doppler velocimetry	Mie scattering-Doppler shift	Flow velocity	Point
Phase Doppler velocimetry	Mie scattering-Doppler shift	Particle size, flow velocity	Point
Laser Doppler vibrometry*	Doppler shift	velocity	Point, 2D
Particle image velocimetry*	Light scattering	Flow velocity	2D, 3D

From what has been discussed above, it is clear that optical measurements are ideally suited for the investigation of the phenomena occurring in organ pipes. This thesis focuses on the use of Schlieren techniques for this problem. The theory behind this technique and the practical realization of such a measuring set-up is thoroughly discussed in the following two chapters. Next to Schlieren measurements, also experiments using the Particle Image Velocitmetry and Laser Doppler Vibrometry technique were performed. The results of each of these techniques are given in chapter 5, followed by a discussion of the advantages and disadvantages of each technique.

3   Schlieren and Shadowgraph techniques

3.1   Principles of the Schlieren methods

3.1.1 Light propagation through inhomogeneous media

The word Schliere originates from the German 'Schliere', meaning streak. It is used as collective noun for gradient disturbances of inhomogeneous transparent media. Schlieren are small differences in refractive index, and therefore bend light rays from their original direction.

The refractive index is defined as

$$n = \frac{c_0}{c} \tag{3.1}$$

Were c is the light speed in the studied medium and c_0 the speed of light in vacuum.

For gasses, a relationship between the refractivity $(n-1)$ and the gas density ρ can be written:

$$n - 1 = k\rho \tag{3.2}$$

k is the Gladstone-Dale coefficient. This parameter depends on the gas and increases slightly with increasing wavelength λ. From equation 3.2 one can conclude that the refractivity depends on gas composition, temperature, density and wavelength of illumination. k varies from 0.1 to 1.5, which means that the refractive index is only weakly dependent on the density. So if small density variations have to be observed optically, very sensitive optics are needed. A solution is to use infrared light, rather than invisible light. Because of the increase of k with λ, weak disturbances will be more detectable using illumination with higher wavelengths.

Optical inhomogeneities will refract or bend light rays in proportion to their refractive index gradient. For a right-handed Cartesian coordinate system with z aligned with the optical axis and a Schlieren object in the $x - y$ plane, the equation of the ray curvature is given by:

$$\frac{\partial^2 x}{\partial^2 z} = \frac{1}{n}\frac{\partial n}{\partial x} \tag{3.3}$$

$$\frac{\partial^2 y}{\partial^2 z} = \frac{1}{n}\frac{\partial n}{\partial y} \tag{3.4}$$

The components of the angular ray deflection are obtained after integration:

$$\varepsilon_x = \frac{1}{n}\int \frac{\partial n}{\partial x} dz \tag{3.5}$$

$$\varepsilon_y = \frac{1}{n}\int \frac{\partial n}{\partial y} dz \tag{3.6}$$

For a two-dimensional Schlieren object of extent L along the optical axis, inserted in surrounding medium with refractive index n_0 , these equations become [33], [34]:

$$\varepsilon_x = \frac{L}{n_0}\frac{\partial n}{\partial x} \tag{3.7}$$

$$\varepsilon_y = \frac{L}{n_0}\frac{\partial n}{\partial y} \tag{3.8}$$

3.1.2 Schlieren versus Shadowgraph technique

Schlieren and Shadowgraph methods are closely related. However, some important differences exist. First of all, the Schlieren technique produces a real focused image; it has a conjugate optical relationship to the Schlieren object. On the contrary, a shadowgram is just a shadow. Furthermore, the illuminance level in a Schlieren image responds to the first derivative of the refraction index, and thus the deflection angle ε is displayed. In a shadowgram, the second derivative is measured and the ray displacement resulting from the deflection is imaged.

For both techniques, several configurations exist. The major distinction is that for a Schlieren configuration, a knife-edge is needed in order to cut off a part of the refracted light. Also, in most circumstances, a Shadowgraph configuration requires less optical components and is easier to set up compared to a Schlieren configuration. However, Shadowgraphy gives rise to less sensitive images than Schlieren photography does. Thus, depending on the application, a well considered choice between complexity, sensitivity and costs has to be made. [34]

3.2   Shadowgraph techniques

3.2.1 Direct Shadowgraphy in diverging light

The simplest form of the Shadowgraph techniques is the Direct Shadowgraphy. For this optical technique, only a light source and a screen are needed (Figure 9). Without the Schlieren object S in the field of view, the screen would be illuminated uniformly. But with the presence of the Schlieren, some rays are deflected form their original paths. Therefore, some spots on the screen will be illuminated more or less, casting a shadow.
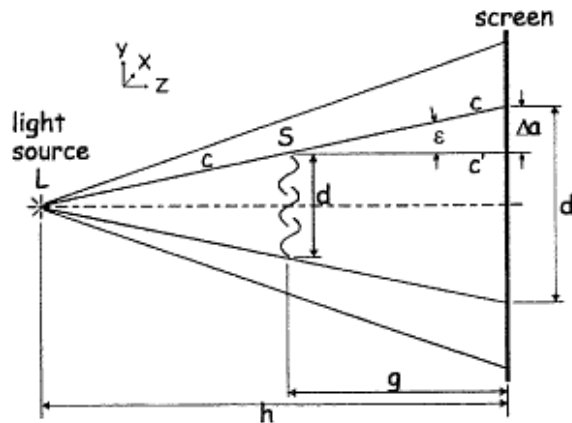
Figure 9: Configuration for the Direct Shadowgraph technique in divergent light.
Because of the presence of the Schlieren object S with height d, a light ray c is bended by an angle ε, causing it to strike the screen at a distance $\triangle\,a$ from its original position and creating a shadowgram with height d'. [34]

This is indicated on Figure 9: the light ray c is bended by an angle $\boldsymbol{\varepsilon}$ from its original path. Therefore, it strikes the screen at a distance $\triangle\,a$ from the original intersection, whereof one can write:

$$\Delta a = \varepsilon \cdot g \tag{3.9}$$

The optical inhomogeneities of the Schlieren object thus redistribute the screen illuminance. However, a Schlieren object is only visible at a shadowgram when it has varying lateral refractive index gradients $\frac{\partial n}{\partial x}$ or $\frac{\partial n}{\partial y}$. A uniform gradient would shift the entire light beam undisturbed and no shadowgram can be observed. Thus, differential illuminance shifts only occur in Shadowgraphy when there is a change in refractive index gradient. Referring to paragraph 3.1.1, it is the gradient of the deflection angle, $\frac{\partial \varepsilon}{\partial x}$ or $\frac{\partial \varepsilon}{\partial x}$ that is observed in a shadowgram in the form of ray displacement.

Using some simple goniometry, the magnification m of the shadowgram can be written as:

$$m = \frac{d'}{d} = \frac{h}{h-g} \tag{3.10}$$

The contrast of the shadowgram, i.e. the increase in illuminance ΔE compared to the background illuminance E, was first defined by:

$$\frac{\Delta E}{E} = \frac{\Delta a}{d'} = \frac{\varepsilon}{d} \cdot \frac{g(h-g)}{h} \tag{3.11}$$

Where the term $\frac{\varepsilon}{d}$ characterizes the Schlieren object, and $\frac{g(h-g)}{h}$ represents the effect of the optical geometry on the sensitivity. However, later researchers found that, instead of $\frac{\varepsilon}{d}$, the strength of refraction in the Schlieren object should be written as $\frac{\partial \varepsilon}{\partial y}$ or $\frac{\partial \varepsilon}{\partial x}$, depending on the direction in which the refractions are observed. This clarifies that it is not the refraction angle ε that is sensed by the Shadowgraph method, but rather its spatial derivative. For refractions in the y-direction, the contrast becomes then:

$$\frac{\Delta E}{E} = \frac{\partial \varepsilon}{\partial y} \cdot \frac{g(h-g)}{h} \tag{3.12}$$

The optimum of this contrast is reached by choosing $h = 2g$. For this value, the equation yields:

$$\frac{\Delta E}{E}\bigg|_{max} = \frac{\partial \varepsilon}{\partial y} \cdot \frac{h}{4} \tag{3.13}$$

From this, one can conclude that a high sensitivity is reached by choosing h as large as possible and locating the Schlieren object in the middle of the source and screen.

Figure 9 demands a point light source. In reality, the source diameter D is always finite, causing a circle of confusion in the shadowgram. This is also known as geometric blur. Referring to Figure 10, the diameter of this circle is:

$$D_{cc} = \frac{gD}{h-g} \tag{3.14}$$

So when the configuration is set according to the maximum sensitivity, the diameter of the circle of confusion equals that of the light source.
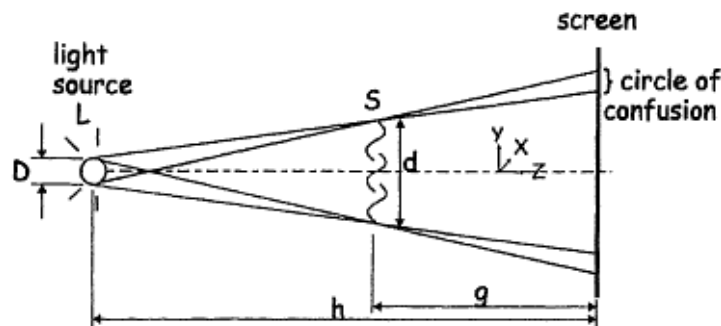
Figure 10: A finite source diameter causes geometric blur. [34]

To avoid this, Contact Shadowgraphy can be used. Here, the screen is placed directly behind the Schlieren object. This leads to a low sensitivity, but sharp shadowgrams can be made, using any light source.

The tolerable level of blur in a shadowgram depends on the size δ of the smallest Schlieren feature that needs to be resolved. By dividing the diameter of the circle of confusion by the magnification, the relative blur size is obtained:

$$\left.\frac{D_{cc}}{m}\right|_{h=2g} = \frac{gD}{h}$$

(3.15)

A Schlieren object of size δ in the test zone can then be visualized only, if it is greater than the relative blur size, i.e. if g is maintained less than $\frac{\delta h}{D}$. The corresponding maximum sensitivity can then be written as:

$$\frac{\Delta E}{E} = \frac{\partial \varepsilon}{\partial y}\frac{\delta h}{2D}$$

(3.16)

From this equation, it follows that when the diameter of the light source is reduced, sensitivity increases. However, beyond a certain limit of light source diameter, a further increase in sensitivity is impossible because diffraction fringes appear. An expression for the minimum light-source diameter, causing no diffraction, was derived by Weinberg for monochromatic light with wavelength λ_l:

$$D_{min} = 1.33\sqrt{\frac{\lambda_l h(h-g)}{g}}$$

(3.17)

The corresponding smallest feature of the Schlieren object that can be visualized in the schadowgraph is given by:

$$\delta_{min} = 1.33\sqrt{\frac{\lambda_l g(h-g)}{h}}$$

(3.18)

The sensitivity and blur functions, introduced above, can be plotted graphically (Figure 11). For the sensitivity function, equation 3.12 is used. The geometric blur function is $\frac{g}{h}$, and the diffraction blur function is based on equation 3.18 and equals $1.33\sqrt{\frac{g}{h}\left(1-\frac{g}{h}\right)}$. From this graph, one can conclude that it is not necessary to put the Schlieren object exactly at $g = \frac{h}{2}$, because the sensitivity does not change significantly for $\frac{g}{h}$ in the rage of 0.3 - 0.7. Because also the diffraction blur is at his maximum for $\frac{g}{h} = 0.5$, it is best to chose $\frac{g}{h}$ somewhat aberrant from 0.5, and preferably smaller than this value, in order to minimize the geometric blur.
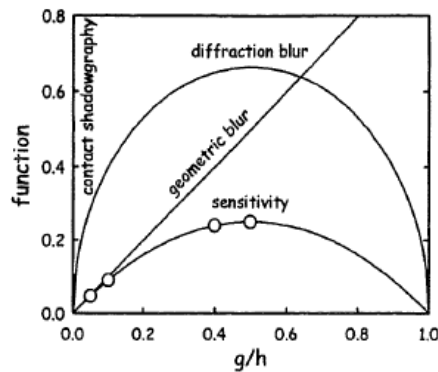
Figure 11: Sensitivity and blur functions for Direct Shadowgraphy in divergent light. [34]

3.2.2   Direct Shadowgraphy in parallel light

By using a convergent light source instead of a divergent one, the results of the shadowgrams can be highly improved. In practice, a lens or mirror is placed between the light source and the test object (Figure 12, Figure 13).
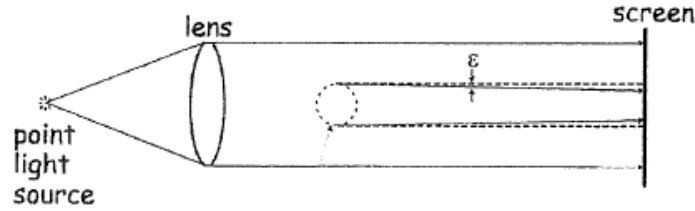
Figure 12: Configuration for the Direct Shadowgraph technique in parallel light, using a lens. [34]
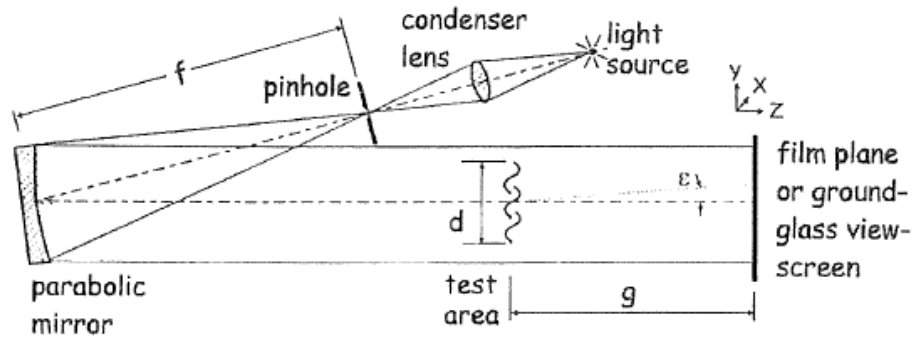
Figure 13: Configuration for the Direct Shadowgraph technique in parallel light, using a mirror. [34]

In this case, the magnification becomes unity, whereby the contrast of the shadowgram becomes:

$$\frac{\Delta E}{E} = \frac{\Delta a}{d} = \frac{\partial \varepsilon}{\partial y} g \tag{3.19}$$

Recalling that the maximum sensitivity for illumination with divergent light occurred at $g = \frac{h}{2}$, and comparing this with equation 3.13, it appears that the sensitivity in the case of parallel illumination is the double of that of divergent illumination for the same distance g.

The circle of confusion in this case equals:

$$D_{cc} = \frac{gD}{f_1} \tag{3.20}$$

With f_1 the focal length of the mirror. From equation 3.20, it can be concluded that, in order to minimize the geometric blur, a mirror or lens with a large optical length is preferred, and, as in the previous case, a small light-source diameter. Again, this diameter cannot be extremely small, because of the diffraction blur. The minimum useful light-source diameter D_{min} in this case becomes:

$$D_{min} = f_1 \sqrt{\frac{\lambda_l}{g}} \tag{3.21}$$

3.2.3   Focused Shadowgraphy

When additional optical elements are placed between the Schlieren object and the screen, one speaks of Focused Shadowgraphy (Figure 14). A second field lens is used in order to focus the beam and a focusing

lens images the shadowgram plane M onto the screen. M and M^* are conjugate optical planes, thus the primary shadowgram at M is projected and eventually sized by the lens to form a shadowgram at M^*.
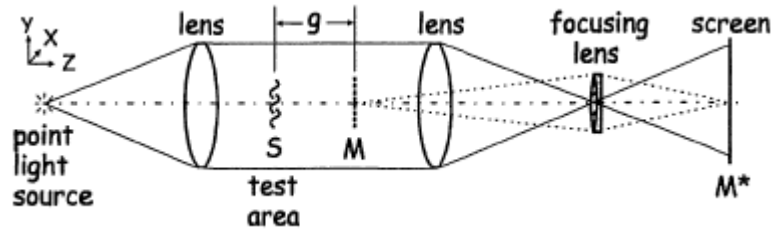
Figure 14: Configuration for the Focused Shadowgraph technique. [34]

The major advantage of this technique is the ability to vary the magnification and thus to adjust the size of the image. Also, while magnification and sensitivity are linked in the Direct Shadowgraph technique (equation 3.10 and 3.11), inserting a lens decouples this two quantities. [34]

3.3   Schlieren techniques

3.3.1   Working principle

3.3.1.1 Point light source

As mentioned before, different kinds of configurations exist for the Schlieren technique. The simplest form is shown in Figure 15. Actually, it is nothing more than the configuration for the Focused Shadowgraphy, discussed above, extended with a knife-edge placed in the focal point of the second lens or mirror. The difference, however, is that in this case a real image of the test area is formed, while in the Focused Shadowgraph technique the shadowgram is focused on the screen.
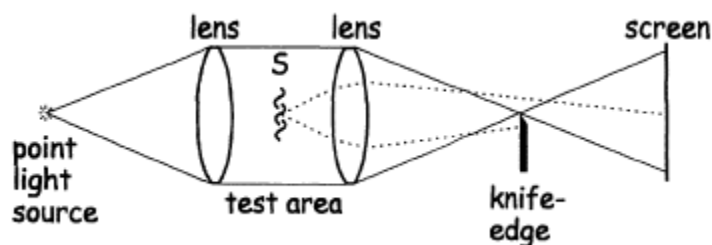
Figure 15: Configuration for the Schlieren technique. [34]

The working principle is similar to that of the Shadowgraph technique: a light beam, coming from a point source is collimated by a lens. A second lens then refocuses the beam to an image of the point source in the knife-edge plane. When a Schlieren object is present, it bends the light rays from their original paths. The second lens then focuses the rays to a corresponding image point on the screen. The source and knife-edge planes, as well as the test area and screen planes are thus sets of conjugate optical planes. An upward deflected ray will brighten a point on the screen. However, some of the downward deflected rays are blocked by the knife-edge. The corresponding image point will therefore be dark compared to an image point corresponding to an undisturbed ray. Thus, the illuminance of a spot of the image will decrease or increase, depending whether the deflection is towards or away from the opaque side of the knife-edge. Therefore, it is clear that the orientation of the knife-edge is very important and depends on the direction in which the density gradients are to be observed. This is illustrated in Figure 16: in (c), the knife-edge is placed horizontally like in Figure 15 and therefore, it only detects vertical index variations $\frac{\partial n}{\partial y}$ in the Schlieren object. Horizontal components $\frac{\partial n}{\partial x}$ move along the knife-edge, but do not cross it, so in order to detect them, a vertical placement as in Figure 16 (b) is necessary. As a result, in order to visualize

the whole Schlieren object, both a vertical and horizontal knife-edge is needed. Practically, this can be realized by choosing a circular hole as in Figure 16 (a).
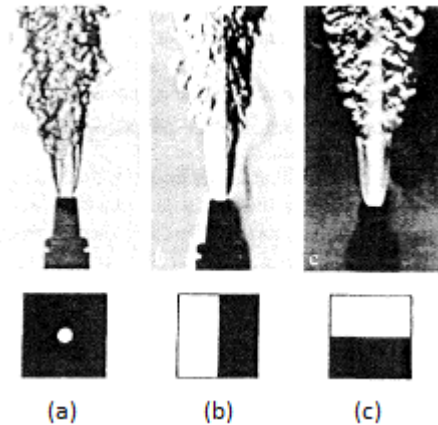
Figure 16: Influence of the orientation of the knife-edge. [34]

Also the position of the knife-edge with respect to the optical axis is important. When no Schlieren object is present, it determines the brightness of the image and thus the contrast between the illuminance of spots corresponding to whether deviated or non-deviated rays. The distance between the Schlieren edge to the optical axis is therefore a measure for the sensitivity of the set-up.

3.3.1.2 Influence of a finite light source

A real light source can be considered as an array of point sources, distributed along the vertical height of the extended source (Figure 17). Each point produces a light beam that focuses to a corresponding point in the light source image at the knife-edge plane. Every point in the test area is thus illuminated by an infinite number of rays; each point in the light source illuminates every test area point. This leads to the generation of a composite light source image at the knife-edge plane: the image is the superposition of many elemental source images originating from all points of the test area. Because every point in the test area contributes an entire elemental source image to the composite image, advancing the knife-edge blocks each elemental source image equally when no Schlieren object is present. Every test area point is then equally reduced in light and the screen will darken uniformly.
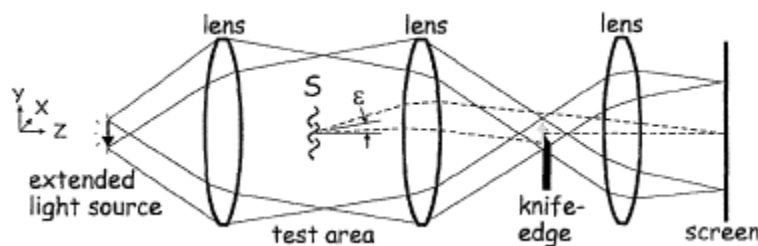
Figure 17: Influence of an extended light source. [34]

When a Schlieren object is placed in the test area, instead of one single ray as in the case for a point source, a ray bundle, coming from all light source points will be refracted and form a displaced elemental source image in the knife-edge plane (Figure 18). If the bundle is bended by an angle ε, having y-component ε_y, the vertical displacement of the corresponding elemental source image in the knife-edge plane is:

$$\Delta a = f_2 \cdot \varepsilon_y \tag{3.22}$$

Where f_2 is the focal length of the second field lens or mirror. Nevertheless, the bundle is returned by the second lens to the same relative position in the conjugate image plane on the screen. Because the refracted bundles will give rise to a displaced source image, the amount of cutoff at the knife-edge will

differ from that of the undisturbed bundles. The Schlieren image will therefore be built up of many points of varying illuminance, corresponding to the shape of the Schlieren object. It is clear that in this case a continuous gray-scale Schlieren image is formed, while in the case of a point source only a binary black and white scale is possible, because a single ray is considered, which is whether blocked as a whole or not at all.
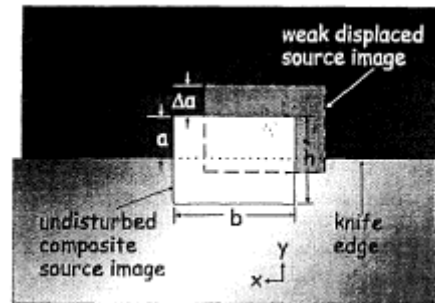
Figure 18: Elemental source images in the knife-edge plane.
An undisturbed source image with height h and width b has an unobstructed height a. By passing a Schlieren object, the source image can be shifted with an amount Δa, causing a variation in illumination on the screen. [34]

3.3.2   Configurations of the Schlieren technique

When a Schlieren set-up is to be designed, one can choose between a configuration using mirrors or lenses. Both have some advantages and disadvantages; a lens-type Schlieren set-up can be put in-line, while mirror-type configurations are inherently folded and therefore more difficult to align. Therefore, off-axis aberrations can occur. On the other hand, using mirrors always entails chromatic aberrations, even for expensive lenses. In general, because lenses demand a higher internal quality than mirrors, they are more expensive and thus often less interesting regarding price/quality.

3.3.2.1 Lens systems

When one opts for using lenses, most of the time the dual-field-lens system is used (Figure 19). Compared to Figure 17, the bare bulb is supplemented by a condenser lens and a slit in order to have an approximately-uniform effective light source with sharp boundaries.
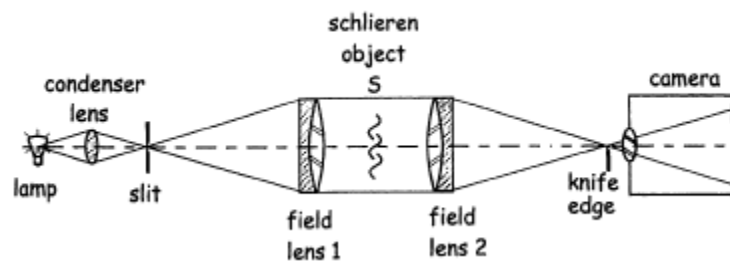
Figure 19: Configuration for the dual-field-lens system. [34]

Because the Schlieren objects are often weak themselves, lens distortions can easily mask them. Therefore, high quality lenses, like telescope objectives or projector lenses are needed.

3.3.2.2 Mirror systems

Since parallel light in the test area is desired, parabolic mirrors can be used instead of lenses. The most common mirror-type configuration is the Z-Type 2-Mirror Schlieren system (Figure 20).

Two symmetrical, on-axis parabolic mirrors are oppositely-tilted and replace the lenses of the dual-field-lens configuration. Because of this tilting, two particular aberrations occur: coma and astigmatism. The cause and characteristics of coma are discussed in Appendix A, paragraph A.4.1.2. The amount of coma is proportional with the offset angle θ and the inverse square of the mirror's f-number. In order to minimize coma, the offset angle mist be kept small and the f-number must be chosen as high as possible. But, since coma is generated at both mirrors, it is possible to cancel out the overall effect by tilting the mirrors at

equal but opposite angles. That exactly, is the reason why the Z-type system is so commonly used; if the mirrors are perfectly arranged, no coma occurs. Unfortunately, astigmatism cannot be eliminated likewise. In paragraph A.4.1.3, it is described how astigmatism creates 2 focal points; the tangential focus and the sagittal focus. In these points, the cross section of the beam is transformed into, respectively, a horizontal and vertical line. Therefore, in order to cut off all elemental source images equally, the knife-edge must be positioned in the focal point, where it is parallel to this line. This means that if a horizontal knife edge is used, it should be placed in the tangential focus, while in the case of a vertical knife-edge, it should be placed in the sagittal focus. [32], [33], [34]
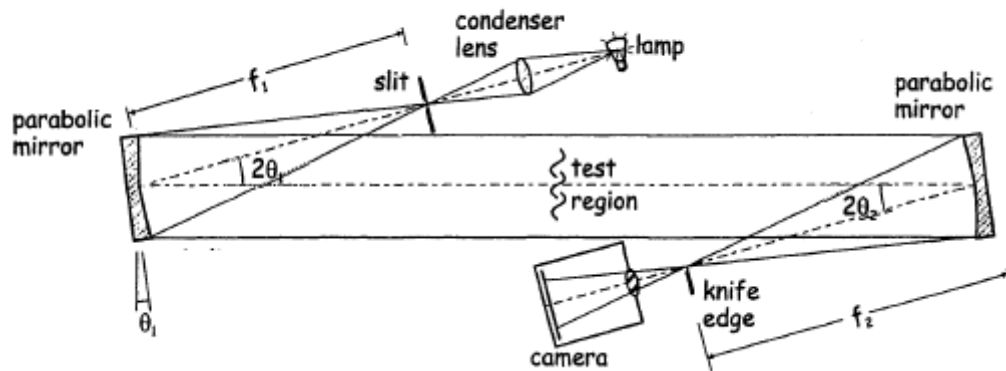
Figure 20: Configuration for the Z-Type 2-Mirror Schlieren system. [34]

4   Set-up

4.1   Towards the z-type mirror system

In the previous chapter, different forms of Shadowgraph and Schlieren techniques were introduced in an order of increasing complexity. Because of the advantages of the z-type 2 mirror system, discussed in the previous chapter and its relative compactness compared to that of a lens-system, this configuration was used for the measurements. But in order to get acquainted with this technique, the whole list of introduced techniques was run through, starting with the simplest form and consecutive introducing extra optical components to finally reach the complex z-type 2 mirror system. As illuminator section, a tungsten-halogen lamp is used, extended with a condenser lens and source slit in order to produce a regular, approximately-uniform effective light source. The flow above a candle served as Schlieren object.

4.1.1   Direct Shadowgraphy in divergent light

The measurements in divergent light were made by placing the candle between the illuminator and a screen. According to equations 3.12 and 3.13, a maximum sensitivity is obtained by choosing the distance between the source slit and the screen, h, as large as possible, and placing the Schlieren object in the middle of it. Because then also the diffraction blur would be maximum, the source dimensions have to be chosen correct, in order not to have this effect. Because of practical considerations, h was chosen to be 1500 mm, whence an optimal value of 750 mm for g follows (Figure 21). The wavelength of the light emitted by the halogen lamp goes from 380 nm to 780 nm. Therefore, the minimum usable light source diameter can be calculated using equation 3.17:

$$D_{min} = 1.33 \sqrt{\frac{780 \cdot 10^{-9}m \cdot 1.5m(1.5m - 0.75m)}{0.75m}} = 0.00144m \tag{4.1}$$

Therefore, the slit height was chosen to be 1.5 mm. In order to check the behavior of the sensitivity and blur functions, given in Figure 11, the distance g was varied from 200 mm up to 1200 mm. The results are shown in Figure 22.
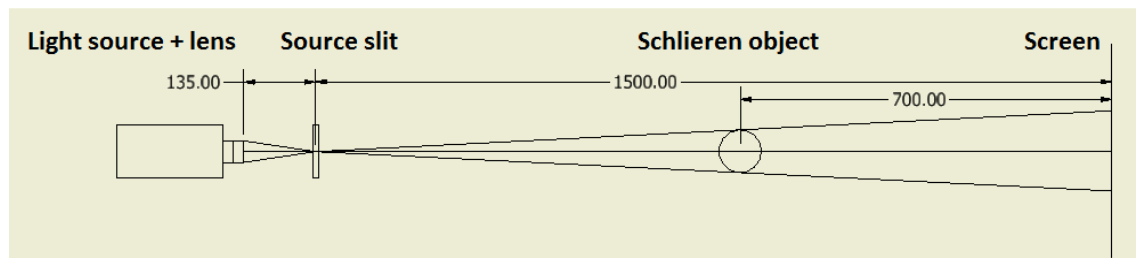
Figure 21: Schematic representation of the set-up for Direct Shadowgraphy in divergent light.

As predicted by Figure 11, the sensitivity is reasonable and does not change a lot for the pictures (c), (d) and (e). However, it is remarkable diminished for values strongly deviating from $h = 2g$ as in picture (a), (b) and (f). The circle of confusion is clearly distinguishable on all images.

(a) g = 200 mm   (b) g = 400 mm   (c) g = 600 mm

(d) g= 800 mm   (e) g = 1000 mm   (f) g = 1200 mm
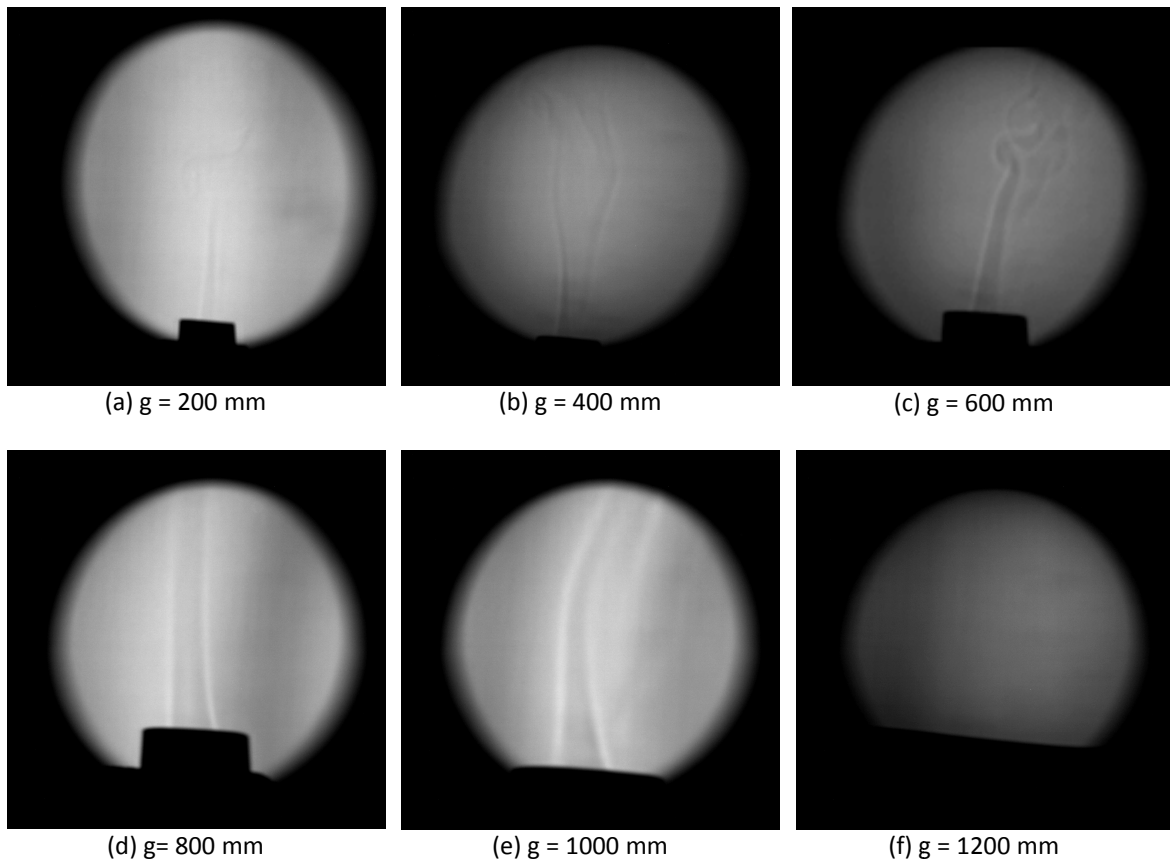
Figure 22: Influence of the parameter g on the shadowgram in divergent light.

4.1.2 Direct Shadowgraphy in parallel light

For the Direct Shadowgraphy in convergent light, a parabolic mirror was added to render the light beam parallel. This mirror has a diameter of 108 mm and a focal length of 647.7 mm. It is therefore positioned on a distance of 647.7 mm from the source slit. Figure 23 shows a schematic representation of the configuration. As predicted in paragraph 3.2.2, the sensitivity of images obtained with this configuration should be twice that of the configuration in the previous paragraph. Figure 24 shows the flow above a candle for different values of g.
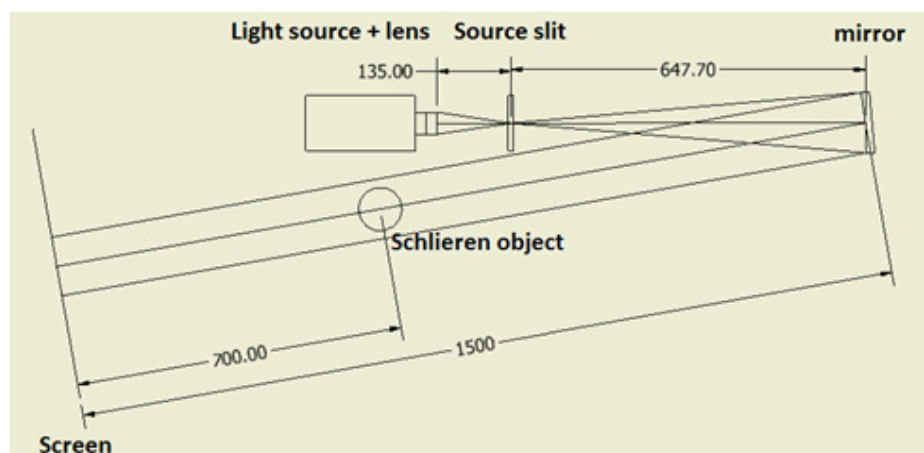
Figure 23: Schematic representation of the configuration for Direct Shadowgraphy in convergent light.

| (a) g = 200 mm | (b) g = 400 mm | (c) g = 600 mm |
| (d) g = 800 mm | (e) g = 1000 mm | (f) g = 1200 mm |
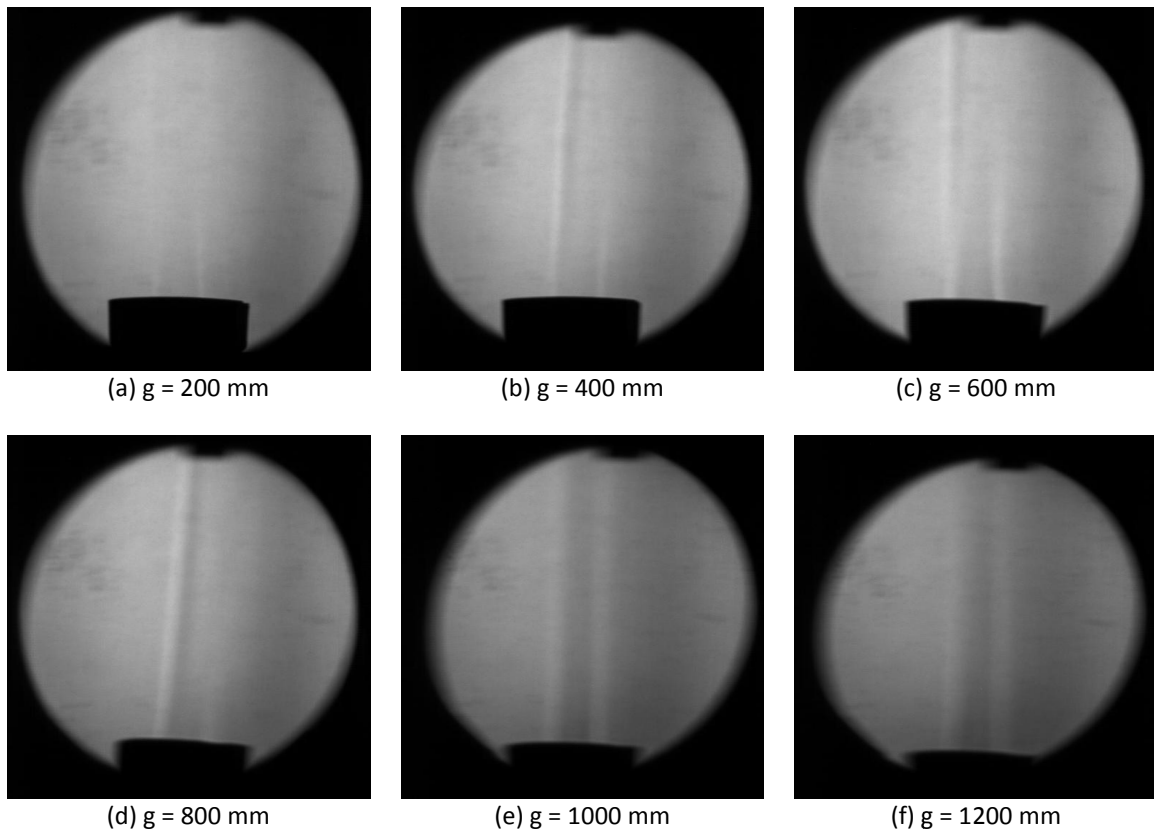
Figure 24: Influence of the parameter g on the shadowgram in parallel light.

The images on the screen indeed showed a higher sensitivity than for the previous case. But because of the global darkness of the images of Figure 22, the image characteristics were artificially adapted to obtain a better view on a printed version. Therefore, comparing these images with those of Figure 24 would result in wrong conclusions. The images clearly show the circle of confusion, as well as its increase in diameter for higher values of g.

4.1.3   Focussed Shadowgraphy

The addition of a focusing lens and a second field mirror turns the previous configuration in one for the Focused Shadowgraphy (Figure 25). The second mirror is identical to the first one, while the focusing lens has a diameter of 50 mm and a focal length of 200 mm. The result is shown in Figure 26.
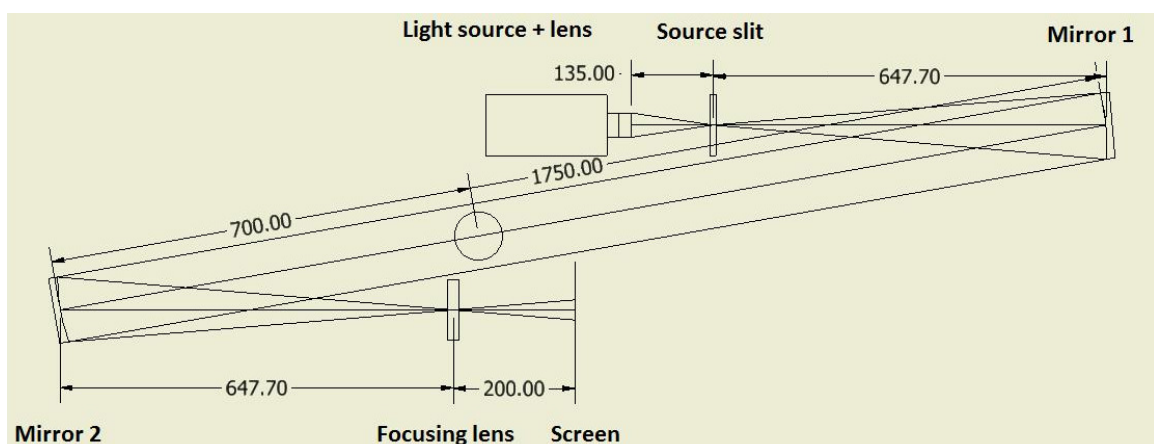
Figure 25: Schematic representation of the configuration for Focused Shadowgraphy.
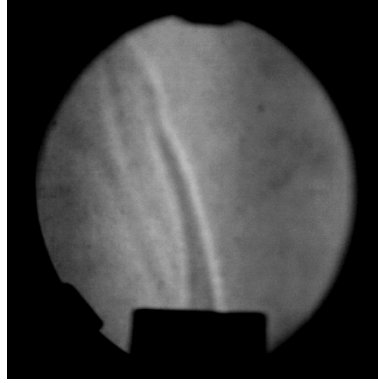
Figure 26: Image of the flow above a candle, using Focussed Shadowgraphy.

4.2 The Z-type 2 mirror system using a halogen lamp

4.2.1 The components of the configuration

By replacing the focusing lens by a knife edge, the configuration is transformed in a Z-type 2 mirror Schlieren system. A schematic representation of the set-up is shown in Figure 27. The tungsten-halogen lamp is suitable for visualizing the flow above a candle, but for the visualization of the airflow in an organ pipe, a higher light intensity is necessary. Therefore, a Nd:YLF laser is used for this experiments. The use of a laser for Schlieren measurements is somewhat impractical because the light damages the eyes, and therefore direct exposure is not recommended. Aligning the Schlieren system in that way is thus far from easy, and therefore the halogen lamp was used for the first experiments to gain the skills required for the set-up and alignment of the system. To obtain an approximately-uniform light source, the condenser lens and source slit were again added to the illuminator section. The shape of the source aperture is unimportant; the only requirement is that it has one straight edge corresponding to the knife-edge cutoff. Therefore, it is chosen to be a rectangle with a width of 3 mm and a variable height ranging from 0 to 1 mm. The used parabolic mirrors have a focal length of 647.7 mm. In what follows, it will be made clear that this is a good compromise between sensitivity and practical considerations. As knife-edge, a simple razor blade was used, attached to a height regulator which has a resolution of 1 micrometer.
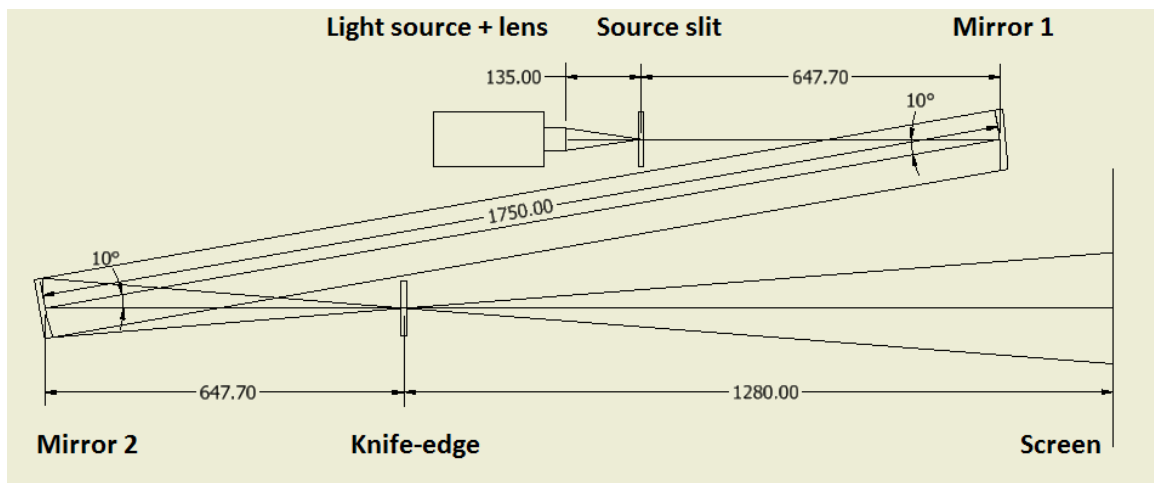
Figure 27: Schematic representation of the halogen lamp Schlieren set-up.

4.2.2 The importance of the knife-edge

The knife-edge is the component that makes the configuration a Schlieren system and distinguishes it from a Shadowgraph set-up. The importance of its emplacement was already mentioned in paragraph 3.3.1.2. The orientation of the edge, as well as its distance with respect to the second field mirror and the

optical axis has an influence on the obtained image. The latter will be described in the following paragraphs. The influence of the shape and orientation of the knife-edge on an image of the flow above a candle is shown in Figure 28. The horizontal cutoff used in figure (a) only blocks downwards deflected light. Therefore, a system using this cutoff, can only detect vertical variations in refractive index as already explained above. Since figure (b) uses a vertical cutoff, horizontal variations in refractive index are to be visualized with this configuration. Figure (c) uses a circular cutoff, and thus variations in all directions can be visualized.

| (a) Horizontal cutoff | (b) Vertical cutoff | (c) Circular cutoff |
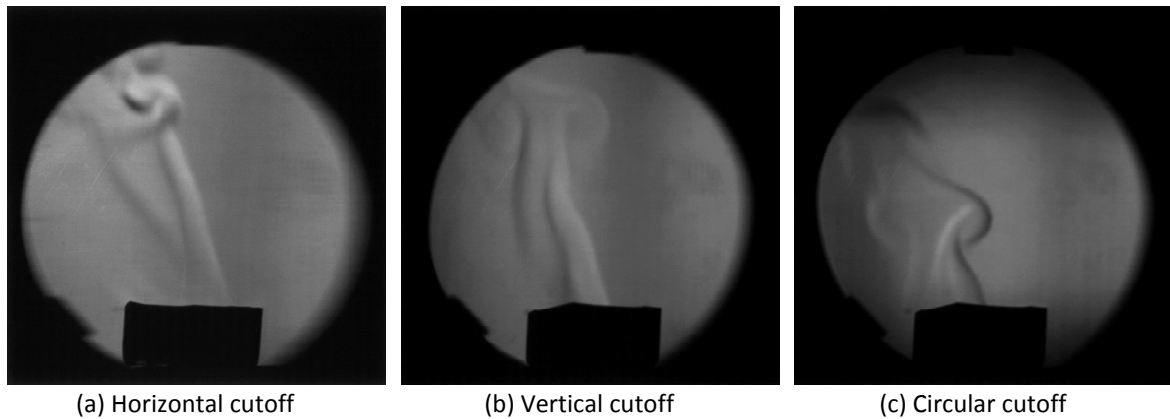
Figure 28: Influence of the shape and orientation of the cutoff.

Because all three options gave reasonable results and considering practical issues, a horizontal cutoff was used for the following measurements.

The position of the knife-edge with respect to the second field mirror determines the homogeneity of the brightness of the image. When the component is not placed exactly in the focal point of the mirror, part of the image will be darkened more or less (Figure 29). By observing the image on the screen, en replacing the knife-edge somewhat for- or backward, the exact position can be found. In this matter, attention must be made into which focal point the component is located; in the sagittal or tangential focal point, depending on the orientation of the edge.

| (a) Too close to mirror | (b) Correct position | (c) Too far from mirror |
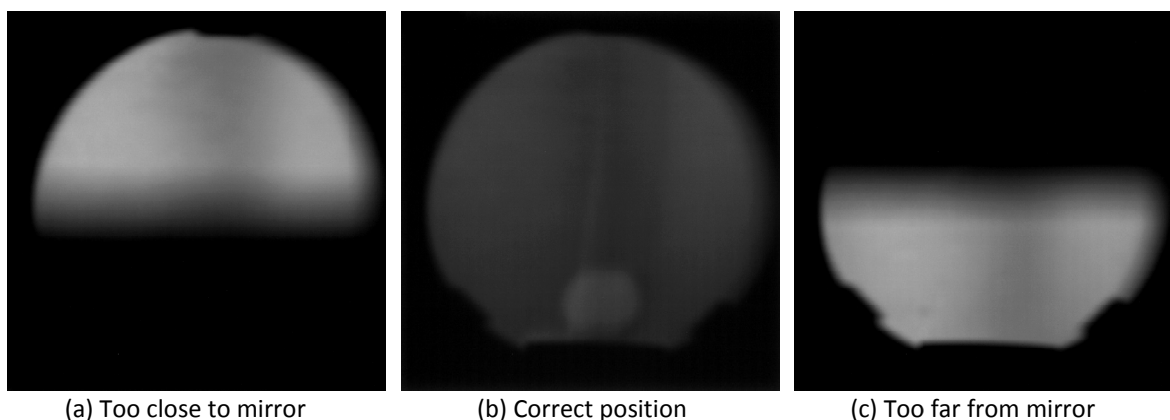
Figure 29: Influence of the position of the knife edge with respect to the second field mirror.
If not correctly positioned, the screen will not be darkened homogeneously.

4.2.3 Sensitivity

Before measurements can be performed, it is important to determine, and if possible maximize the sensitivity of the set-up. Therefore, first the illuminance E_0 upon the first mirror has to be calculated. If the luminance emitted by the light source is B, it can be found by applying the inverse square law:

$$E_0 = \frac{B \cdot b_s \cdot h_s}{f_1{}^2} \tag{4.2}$$

where b_s and h_s are respectively the width and height of the source slit and f_1 the focal length of the first field mirror. If losses are neglected, this illuminance also falls on the test area and the second mirror. In absence of knife-edge cutoff, the image illumince can be calculated by accounting for the magnification m:

$$E_0 = \frac{B \cdot b_s \cdot h_s}{m^2 f_1{}^2} \tag{4.3}$$

However, if there is some cutoff and only the part of light having height a is unimpeded (as is Figure 18), the actual unobstructed height of the light source image becomes $\frac{f_1}{f_2}a$. After replacing h_s by this factor, equation 4.3 becomes:

$$E = \frac{B \cdot b_s \cdot a}{m^2 f_1 f_2} \tag{4.4}$$

Equation 4.4 gives the background illuminance or amplitude level E in the Schlieren image. Depending on the orientation in which a ray bundle is bent, the illuminance of the corresponding point will be above or below this level. Suppose a light ray is bent trough an angle ε having y-component ε_y. Then the vertical displacement of the elemental source image is given by equation 3.22:

$$\Delta a = f_2 \cdot \varepsilon_y$$

Substituting this in equation 4.4 gives the increment in illuminance of the corresponding image point due to the refraction ε_y in the test area:

$$\Delta E = \frac{B \cdot b_s \cdot \varepsilon_y}{m^2 f_1} \tag{4.5}$$

The contrast in the Schlieren image can then be defined by the ratio of differential illuminance ΔE at an image point to the general background illuminance E:

$$C = \frac{\Delta E}{E} = \frac{f_2 \cdot \varepsilon_y}{a} \tag{4.6}$$

Since sensitivity relates the instrument's output to the received input, it can be written as the ratio of the image contrast to the ray deflection ε :

$$S = \frac{dC}{d\varepsilon} = \frac{f_2}{a} \tag{4.7}$$

Thus, the sensitivity is proportional to the focal length of the second mirror; a reason for choosing it as high as possible. However, increasing the focal length increases the overall dimensions of the set-up, and thus a compromise has to be made between sensitivity and practical considerations. Further, equation 4.7 shows that the sensitivity is influenced by the unobstructed height a. In order to have a large sensitivity, it must be made small. This clears the requirement that the source slit must have a straight edge corresponding to the knife edge: if the source edge should be ill-defined, small values of a are impossible to reach.

An interesting feature of the set-up is the minimum discernable contrast $\frac{\Delta E}{E}$ in the image, and the corresponding minimum detectable refraction ε. The minimum contrast, detectable with the human eye

depends on the amount of luminance. This relationship is plotted in Figure 30. The graph shows, that for a luminance above 10 candela/m², a threshold of 2% is possible.
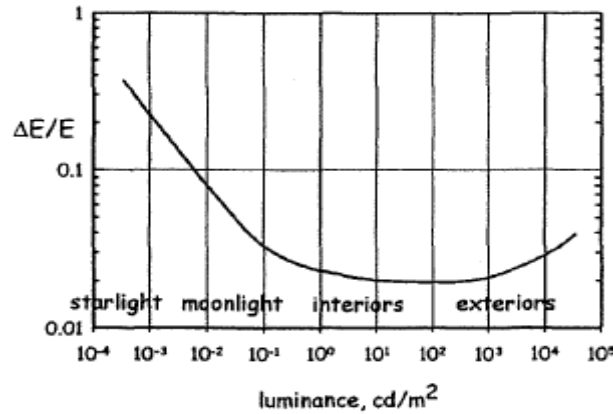
Figure 30: The contrast sensitivity of the human eye as a function of field luminance. [34]

For a given set-up, i.e. when f_2 and the amount of cutoff is known, the minimum detectable refraction angle can be found using equation 4.6. The corresponding minimum detectable index of refraction gradient can then be derived by substituting this minimum refraction angle in equation 3.7 or 3.8. For a horizontal knife-edge, this yields:

$$\left.\frac{\partial n}{\partial y}\right|_{min} = C_{min}\frac{n_0}{L}\frac{a}{f_2} \tag{4.8}$$

Thus, next to a high focal length and a large cutoff, a high sensitivity also demands a Schlieren object with an extensive length along the optical axis.

The luminance of a typical tungsten-halogen lamp after passing a slit of the order of 1x3 mm can be rated at $1.5\cdot 10^7 cd/m^2$. [34] For practical reasons, the screen on which the image is projected was placed at 1280 mm behind the knife edge. This led to a magnification of 1.85. For a slit height of 1 mm and considering no cut off, the background illuminance can be calculated:

$$E = \frac{1.5\cdot 10^7 cd/m^2 \cdot 0.003m \cdot 0.001m}{1.85^2(0.6477m)^2} = 31.3\,\frac{cd}{m^2} \tag{4.9}$$

A typical value for ray deflection occurring in the plume above a candle is 10 arcseconds, or $4.85\cdot 10^{-5}\,rad$. The corresponding increment of illuminance on the image is then:

$$\Delta E = \frac{1.5\cdot 10^7 cd/m^2 \cdot 0.003m \cdot 4.85\cdot 10^{-5}\,rad}{1.85^2 0.6477m} = 0.98 \tag{4.10}$$

From equations 3.4 and 3.5 the contrast of the image point can be easily calculated:

$$C = \frac{\Delta E}{E} = 0.031 = 3.1\% \tag{4.11}$$

And finally, also the sensitivity of the set-up can be calculated:

$$S = \frac{0.6477m}{0.001\,m} = 647.7 \tag{4.12}$$

A contrast of 3% is small; for a background illuminance of 31.3 cd/m² just nearly detectable for the human eye, as can be verified on Figure 30. In order to increase the contrast, the unobstructed height a has to be reduced by increasing the amount of cutoff. The behavior of the contrast as a function of the amount of

cutoff is shown in Figure 31. The contrast stays small for cutoffs up to 60%, but then starts increasing significantly.
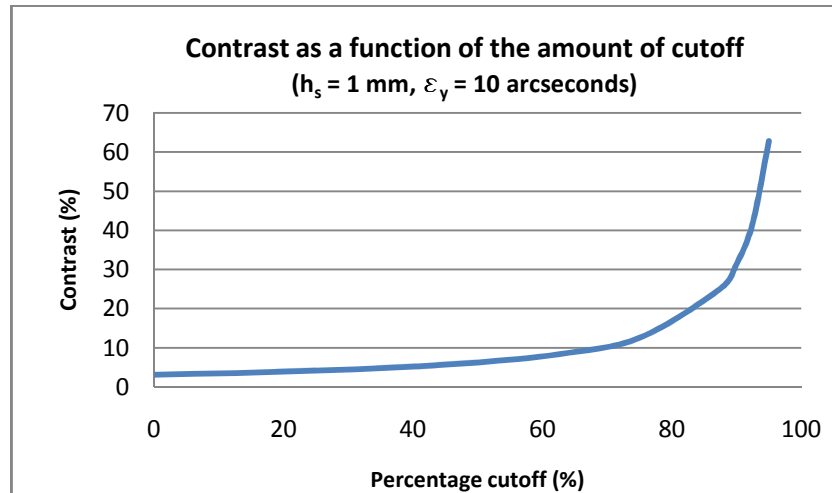
Figure 31: Dependency of the contrast on the amount of cutoff ($h_s = 1\ mm$).

This can also be seen on Figure 32, where the flow above a candle was imaged for different amounts of cutoff. For 0 % cutoff, the contrast is really low; almost nothing can be seen from the image. Increasing the percentage of cutoff clearly increases the contrast; for 50 % cutoff, the flow is already clearly visible. For a cutoff higher than 50%, the contrast increases rapidly with the amount of cutoff. Image (f) is however misleading; in reality, orange-colored flow strips could be distinguished on a totally black background. But because of the global darkness of the image, it was not recorded correctly by the camera.

| (a) 0 % cutoff | (b) 25% cutoff | (c) 50 % cutoff |
| (d) 75 % cutoff | (e) 85 % cutoff | (f) 95 % cutoff |
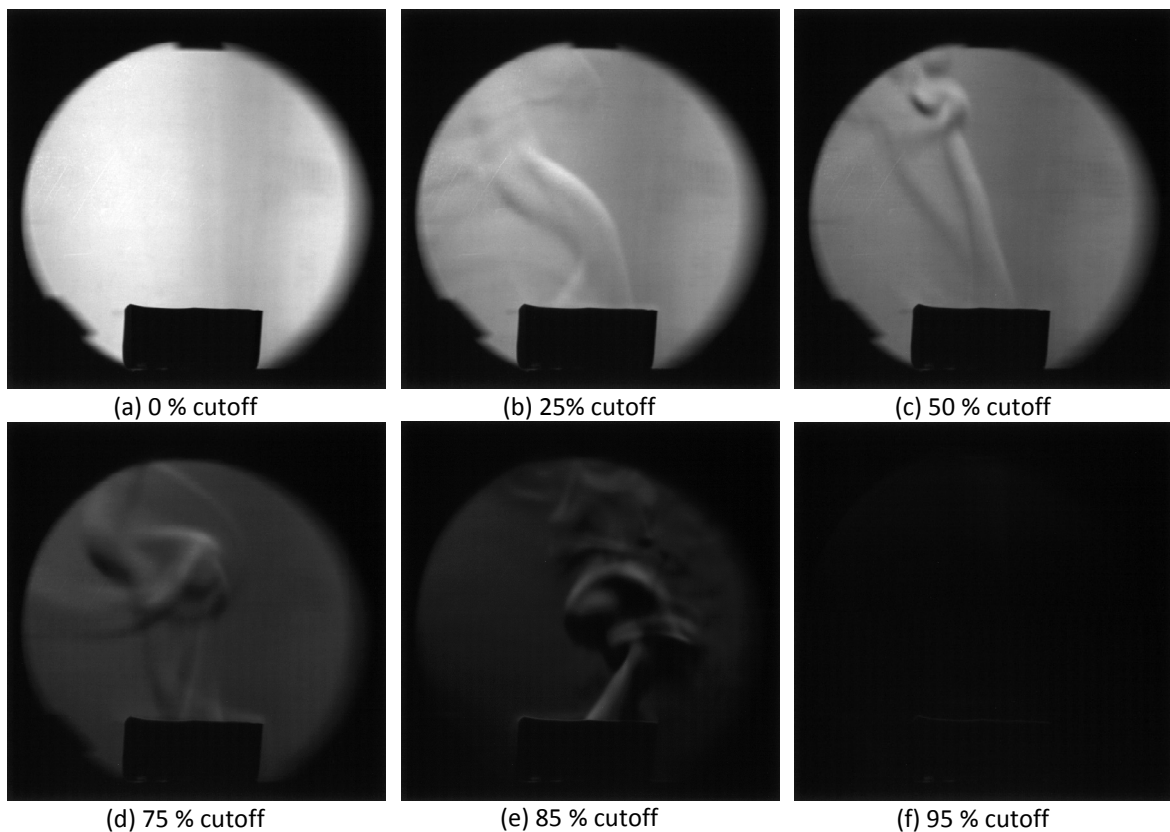
Figure 32: Influence of the amount of cut-off on the contrast ($h_s = 1\ mm$).

Because the unobstructed height a is directly connected to the slit height, the contrast can also be improved by trimming the height. The dependency of the contrast on the slit height is shown in Figure 33; for small values of the slit height, the contrast increases significantly with decreasing slit height. This trend can also be seen in Figure 34, which contains recordings of the flow above a candle for different values of slit height.
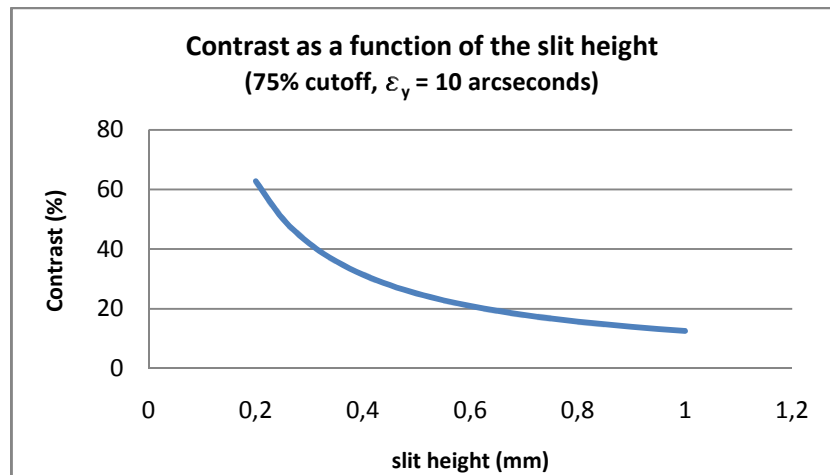
Figure 33: Dependency of the contrast on the slit height (75% cutoff).
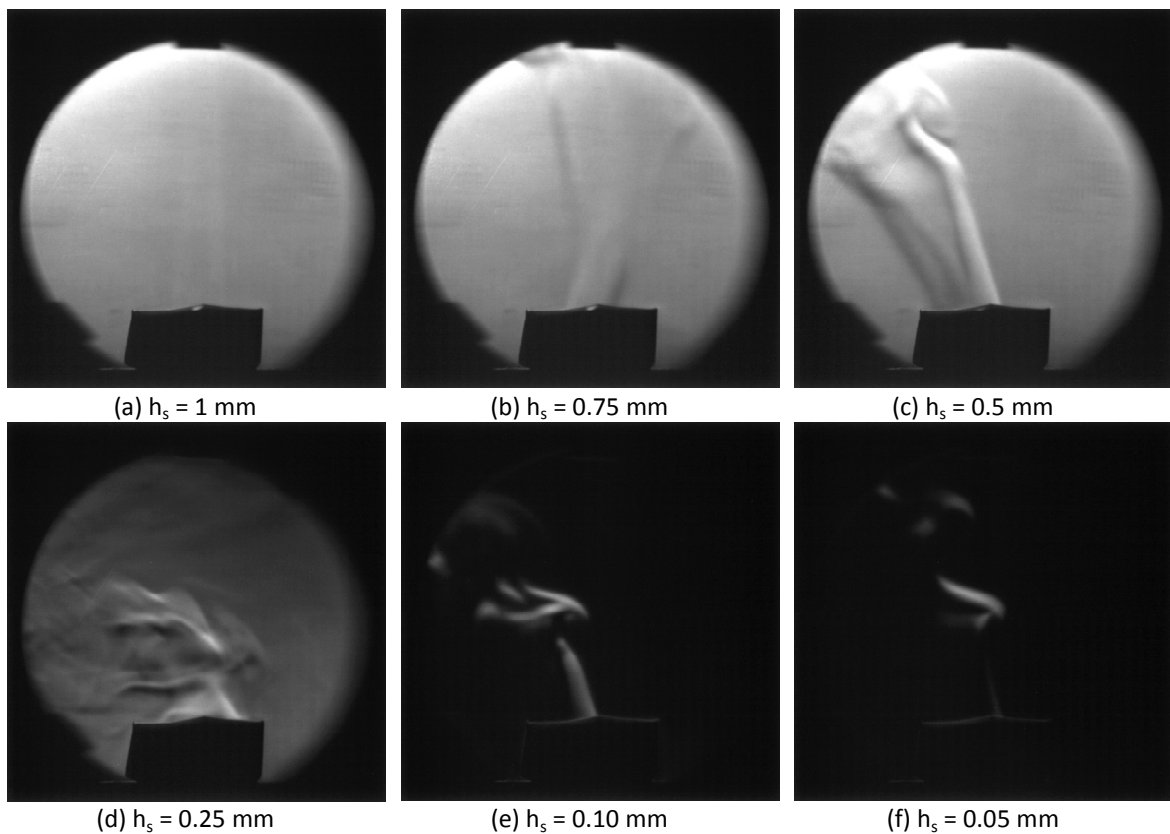
Figure 34: Influence of the slit height on the contrast (75 % cutoff).

4.2.4 Measuring range

The measuring range R of the Schlieren technique contains all refraction angles ε over which a detectable change in image illuminance occurs. In other words, the range over which elemental light source images from various points in the test area remain partially cut off by the knife-edge. Once a source image has shifted entirely off or onto the knife-edge, the corresponding image point has respectively reached the brightest or darkest value possible. Larger deflection angles do not longer cause an incremental illuminance; the conditions are then called out of range.

The maximum range of displacement of the source image, still causing a change in illuminance is equal to the height of the image in the cutoff plane:

$$h_s|_{cutoff\ plane} = \frac{f_2}{f_1} h_s \tag{4.13}$$

The corresponding range of angular deflections δ_{ε_y} is then given by:

$$\delta_{\varepsilon_y} = \frac{h_s}{f_1} \tag{4.14}$$

For an amount of x % cutoff, the corresponding maximal and minimal deflection can then be calculated as follows:

$$\varepsilon_{y,max} = \frac{x}{100} \delta_{\varepsilon_y} \tag{4.15}$$

$$\varepsilon_{y,min} = -(1 - \frac{x}{100}) \delta_{\varepsilon_y} \tag{4.16}$$

Referring to Figure 18, the unobstructed height a can then be calculated using following formula:

$$a = \left(1 - \frac{x}{100}\right) h_s|_{cutoff\ plane} \tag{4.17}$$

By substituting equation 4.13, 4.14 and 4.17 in equation 4.7, the sensitivity can be written as:

$$S = \frac{1}{\left(1 - \frac{x}{100}\right) \delta_{\varepsilon_y}} \tag{4.18}$$

The maximum sensitivity is thus inversely proportional to the range; a high sensitivity entails a narrow measuring range. Mostly, it is desirable to have an equal range for deflections toward the opaque side of the knife edge, as away from it, in order to obtain an equal range for brightening and darkening. This is achieved by choosing a cutoff of 50%. Although this is a good choice form a range point of view it is not for the sensitivity as mentioned above. In practice, mostly a broad source slit is used in order to increase the range, while the cutoff is raised to high values to obtain a higher contrast. This leads to an uneven measuring range, but because most of the time, sensitivity is the most important variable, this is accepted. [33], [34]

The maximum detectable refraction angle can be calculated for the used setup (Figure 35, Figure 36). For a cutoff of 50% and slit height of 1 mm, it is found that $\varepsilon_{y,max} = 0.001544\ rad$ and $\varepsilon_{y,min} = -0.001544\ rad$. As mentioned before, the typical value for ray deflection occurring in the plume above a candle is $10\ arcseconds$ or $4.85 \cdot 10^{-5}\ rad$. Both a downward as upward refraction of this magnitude can thus be visualized using this set-up. This remains true when the slit height is decreased until a value of 0.1 mm.

Range as a function of the slit height (50% cutoff)
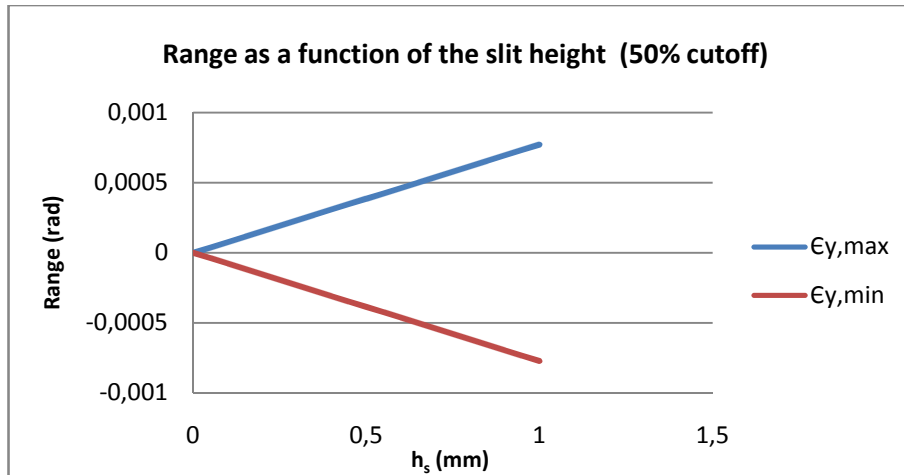
Figure 35: Dependency of the range on the slit height (50% cutoff).

For a cutoff of 95%, things are quite different. For this case, $\epsilon_{y,max} = 0.001467\,rad$ and $\epsilon_{y,min} = -7.7 \cdot 10^{-5}\,rad$, if a slit height of 1 mm is considered. A 10 arcseconds refraction is again visible in both directions. The downward deflection, however, only stays visible if the slit height remains higher than 0.6 mm. For smaller slit heights, a deflection of this magnitude will be shifted entirely on the knife-edge, and will thus be out of range. This is the case in Figure 32 (f) and in Figure 34 (e) and (f); the range is simply too low for the encountered refraction angles, causing large regions to appear binarized black and white.

Range as a function of the slit height (95% cutoff)
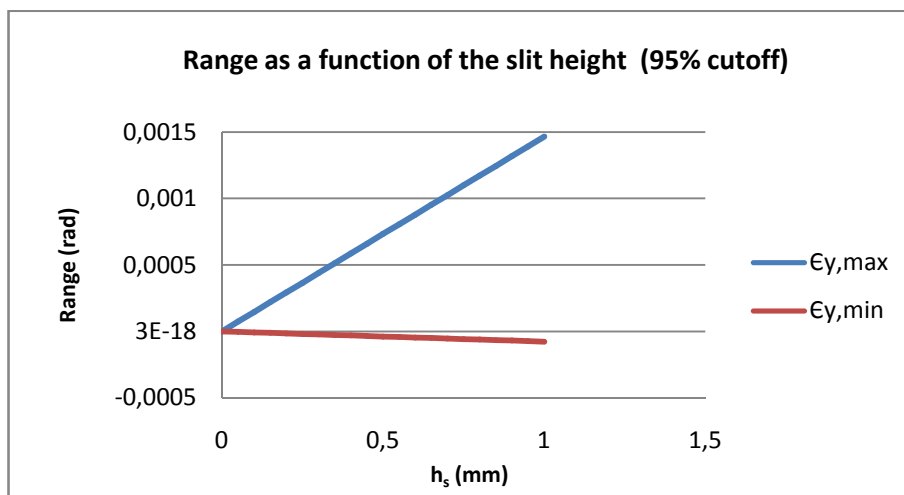
Figure 36: Dependency of the range on the slit height (95% cutoff).

4.2.5 Diffraction effects

The discussion of sensitivity in paragraph 4.2.3 was based on geometrical optics (Appendix A). Equation 4.7 suggests an infinite sensitivity when the unobstructed source image height a tends to zero. However, also the effects of the wave-character of the light have to be considered. When visualizing phenomena using Schlieren techniques, diffraction can influence the image. Two important effects exist: the creation of halos in the images due to diffraction of light in the test area, and the diffraction of the light source image at the knife edge, limiting sensitivity and resolution.

4.2.5.1 Diffraction in the test area

Every opaque edge in the test area diffracts light in the direction perpendicular to that edge. Because this diffracted light lies outside the light-source images in the cutoff plane, it partially escapes from be cut off by the knife-edge. Since the image plane is optically conjugated to the Schlieren object plane, the diffracted light hits the screen at the position of the edge in the test area. Advancing the knife-edge cutoff

decreases the illumination of the image, but not in an equal amount the diffracted light. A bright diffraction band or halo thus appears around all opaque edges in the test area having components parallel to the knife edge. This is shown in Figure 37, where a spanner was inserted in the test zone.
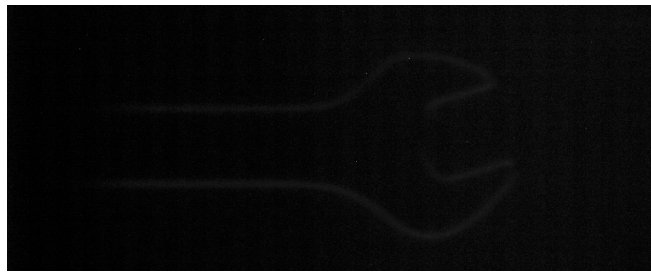
Figure 37: Diffraction in the test area creates a halo around opaque edges.

4.2.5.2 Diffraction at the knife-edge

When the knife-edge cutoff is advanced, the unobstructed source image height becomes smaller. Eventually, a begins to behave like a narrow slit, making light diffracted by edges in the test area to diffract a second time in the cutoff plane. Near 100% cutoff, this creates a sort of diffraction shadow emanating perpendicular to the edges of the objects in the test area. Diffraction at the knife edge thus counteracts any sensitivity gain beyond a certain amount of cutoff and puts a limit on the sensitivity.

Since these halos and shadows only outline opaque object with white lines and do not influence the Schlieren image otherwise, they are mostly not of great concern. One must, however, take care interpreting these phenomena, in order not to be confused with other bright bands that can appear in the image. [33], [34]

5   Organ pipe measurements

5.1 Organ pipe setup

In order to study the flow in organ pipes with means of optical measuring techniques, a transparent copy of a representative organ pipe was necessary. A wooden organ pipe was provided by organ builder Mr. J.P. De Greef. The pipe has a length of 538 mm and a rectangular cross section of 48 mm to 61 mm, while the resonator itself has a length of 495 mm. Because of a mistake during the assembly of the pipe, the transparent pipe was given a cross section of 48 mm to 51 mm, instead of the original one. The mouth geometry was made variable by the realization of several flue top-blocks and labia with different dimensions. The dimension of the flue height could be varied between 1 mm and 10 mm, while the mouth width, the distance between the flue exit and labium, could be chosen between 13 mm and 28 mm. For the angle of the labium, three values were provided: 10°, 20° and 30°. The technical drawing of the organ pipe is given in Figure 38 , while Figure 39 shows an enlargement of the mouth geometry.
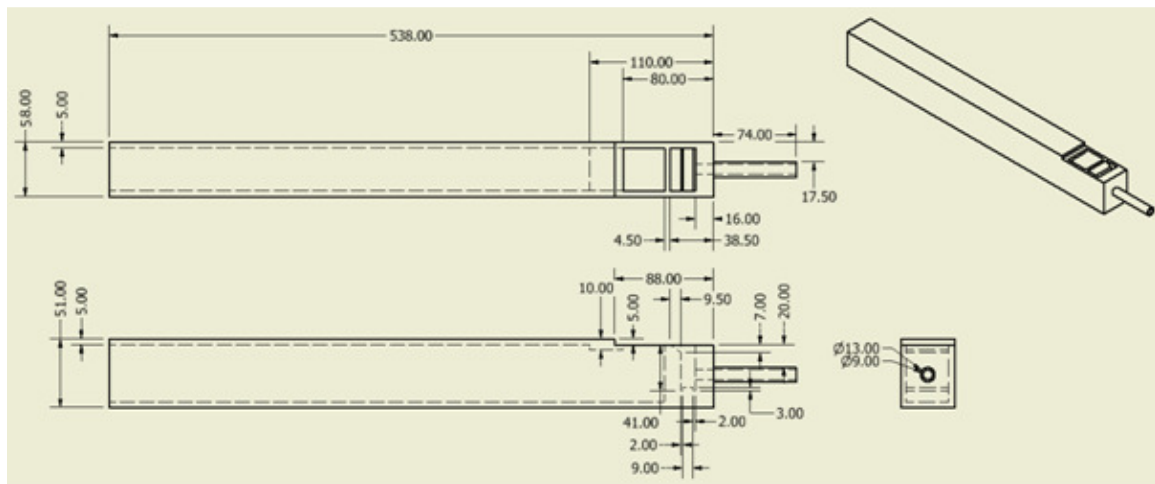
Figure 38: Geometry and dimensions of the tested organ pipe (without labium and flue top-block).
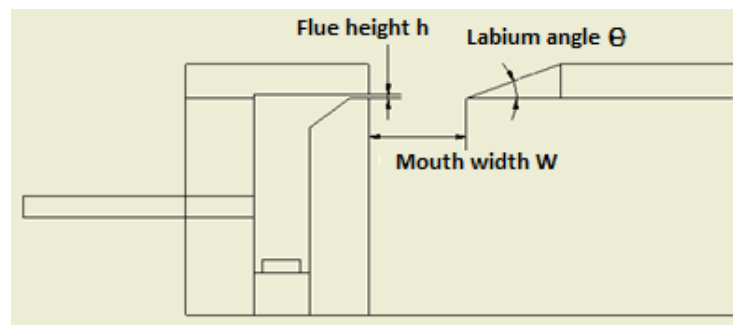
Figure 39: Mouth geometry of the tested organ pipe.

In order to provide the necessary refractive index differences for the visualization of the flow with the Schlieren technique, the pipe was operated using CO_2. This makes the pipe sound flat, but it does not influence the conclusions on the flow [1]. For the other experiments, namely the acoustic, PIV and LDV measurements, this refractive index difference is not necessary, and thus the pipe was driven by air. A schematic representation of the organ pipe set-up is shown in Figure 40. The pipe *(5)* was connected to a bottle of CO_2 or compressor *(1)* by means of a pneumatic servo valve *(4)*, controlled by a signal generator *(2)* and powered by a DC power supply of 24 V *(3)*. The amplitude of the applied control signal is determining for the pressure at which the fluid leaves the valve. Attention must be made when comparing results of the different techniques; the CO_2 was supplied to the servo valve with a pressure of 2 bar, while pressurized air was available under a pressure of 5 à 6 bar. Therefore, the velocity of the jet leaving the flue will be higher for the experiments involving air, compared to those involving CO_2, for a same amplitude of control signal.
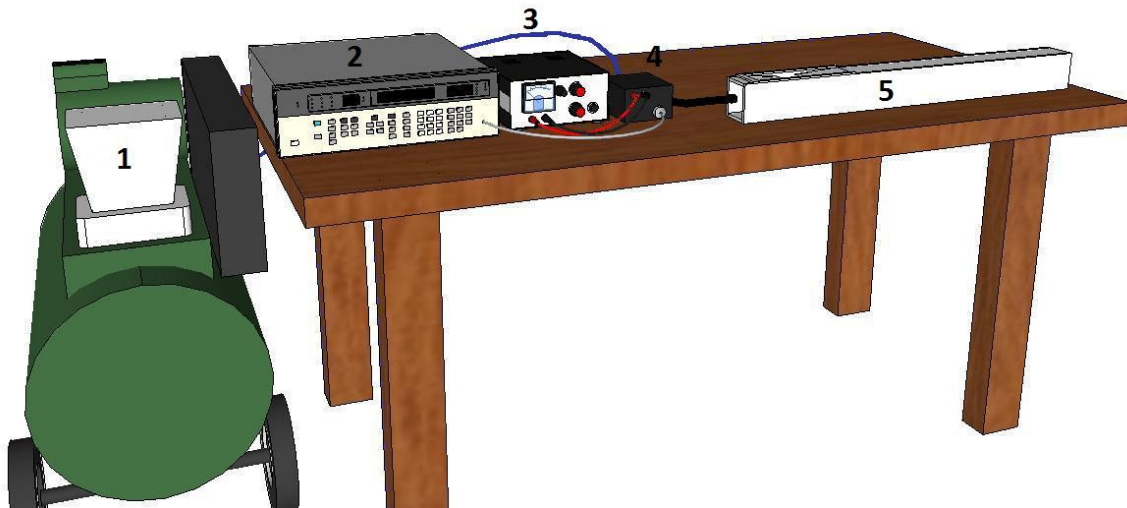
1. compressor/CO_2 bottle   3. DC power supply   5. Organ pipe
2. Signal generator   4. Servo valve

Figure 40: Schematic representation of the organ pipe set-up.

5.2   Study of the frequency spectrum generated by the organ pipe

Before studying the mechanism of sound production in the pipe, it is important to analyze the produced sound. Therefore, the frequency content of the steady sound was studied both theoretical and experimental. The latter was done by two different techniques: fist by using a microphone, and second by using the Laser Doppler Vibrometry technique.

5.2.1   Theoretical calculation of the resonant modes

Using the formula's given in paragraph 2.2.1, the resonant modes of the pipe can be calculated theoretically. This was done for both the open and stopped configuration, by considering a resonator length of 495 mm and a value of 343 m/s for the speed of sound in air. The results are shown in Table 4 for the open pipe and Table 5 for the stopped pipe.

Because an organ pipe is not completely open at the mouth, the real frequencies will deviate a little from the calculated ones. For the open pipe, the measured frequencies will be somewhat lower that the calculated ones, while those for the stopped pipe will be a little bit higher.

Table 4: Calculation of the frequency components occurring in the tested open pipe.

Name (overtone)	Wavelength	Frequency
Fundamental tone	$\lambda_s = 2L = 990 \ mm$	$f_s = \mathbf{1}\dfrac{v}{2L} = 346 \ Hz$
First overtone	$\lambda_s = L = 495 \ mm$	$f_s = \mathbf{2}\dfrac{v}{2L} = 693 \ Hz$
Second overtone	$\lambda_s = \dfrac{2}{3}L = 330 \ mm$	$f_s = \mathbf{3}\dfrac{v}{2L} = 1039 \ Hz$
Third overtone	$\lambda_s = \dfrac{1}{2}L = 247.5 \ mm$	$f_s = \mathbf{4}\dfrac{v}{2L} = 1386 \ Hz$

Table 5: Calculation of the frequency components occurring in the tested stopped pipe.

Name (overtone)	Wavelength	Frequency
Fundamental tone	$\lambda_s = 4L = 1980\ mm$	$f_s = \mathbf{1}\dfrac{v}{4L} = 173\ Hz$
First overtone	$\lambda_s = \dfrac{4}{3}L = 660\ mm$	$f_s = \mathbf{3}\dfrac{v}{4L} = 520\ Hz$
Second overtone	$\lambda_s = \dfrac{4}{5}L = 396\ mm$	$f_s = \mathbf{5}\dfrac{v}{4L} = 866\ Hz$
Third overtone	$\lambda_s = \dfrac{4}{7}L = 283\ mm$	$f_s = \mathbf{7}\dfrac{v}{4L} = 1213\ Hz$

5.2.2   Acoustic measurements

For the acoustic measurements, the organ pipe set-up was placed in an anechoic room and the produced sound signal was measured by a microphone. A Fast Fourier Transform was applied on it to obtain the frequency spectrum. The measurements were done for different values of blowing pressure and different mouth configuration, to analyze the effect of these parameters on the spectrum.

5.2.2.1 Open pipe

First, the influence of the blowing pressure on the frequency spectrum was analyzed. The blowing pressure is determined by the amplitude of the signal controlling the servo valve. Therefore, in what follows, the blowing pressure is expressed in millivolts. The correlation between the amplitude and the resulting pressure in the pipe foot was measured by means of a pressure sensor and is shown in Figure 41. This correlation is valid for a supply pressure of 2 bar, i.e. for the configuration used for the Schlieren measurements. Since air was supplied on a higher pressure, the corresponding pressure in the pipe foot will be higher than suggested by Figure 41.
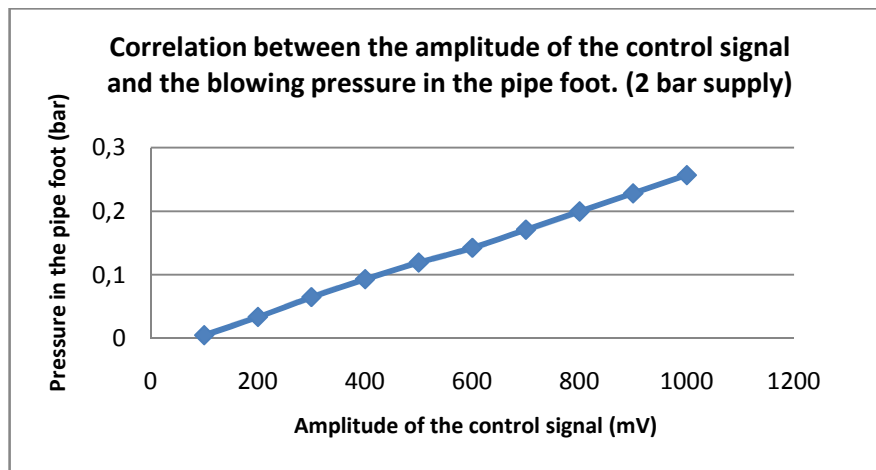
Figure 41: Correlation between the amplitude of the control signal and the pressure in the pipe foot.

Table 6 contains the measured frequencies for different blowing pressures, while Figure 42 shows the variation in amplitude of the harmonics. At 200 mV, only the first and second harmonics are measured. As expected, the amplitude of the fundamental tone is the highest and determines the pitch of the sound, while the second harmonic only contributes to the tone quality. Because of the small amount of higher harmonics and its low amplitudes, no bright sound is produced. For higher blowing pressures, higher harmonics are activated and the brightness of the sound increases. It can be observed that the higher the harmonic, the less it is represented in the spectrum. This could be expected from what was explained at

the end of paragraph 2.2.3; since for higher harmonics, the natural frequencies of the pipe will successively diverge more from the corresponding forced harmonics of the oscillating jet, they will not be amplified in large amount. Up to a pressure corresponding to 500 mV, both the frequency of the harmonics and its amplitudes increase for increasing pressure. This increase of the frequency can be explained by recalling equation 2.4:

$$\frac{T_o}{4} = \frac{b}{0.4v_j} \ or \ f_o = \frac{1}{T_o} = \frac{0.1v_j}{b}$$

Since a higher pressure gives rise to a higher jet velocity, according to equation 2.4, a higher frequency is generated. The increase in frequency explains why for higher pressures, more harmonics are activated; because the frequency of the forced harmonic is raised somewhat, it better agrees with the natural harmonic of the pipe, and therefore, the harmonic is locked in. From a voltage of 600 mV, the frequency and amplitude pattern changes. At this point, overblowing occurs; the jet velocity is made too high, so that the feedback is driven by the first overtone. The frequencies of all harmonics are diminished suddenly, but continue to increase for higher pressures. Remarkable is that the amplitudes of all the odd harmonics are minimal at that point, while the amplitudes of the even harmonics continue to increase. When the pressure is further increased, higher harmonics are generated, which were not observed in normal working.

Table 6: Variation of the frequency of the harmonics in function of the blowing pressure (h = 1 mm, W = 16 mm, labium angle = 10°).

Blowing pressure (mV)	First harmonic (Hz)	Second harmonic (Hz)	Third harmonic (Hz)	Fourth harmonic (Hz)	Fifth harmonic (Hz)	Sixth harmonic (Hz)	Seventh harmonic (Hz)	Eight harmonic (Hz)
200	287	574						
300	304	606	909	1211				
400	309	617	925	1232	1541			
500	313	625	937	1249	1561			
600	303	595	890	1190		1784		
700	303	604	906	1207	1508	1810	2112	2413
800	305	608	912	1216	1519	1823	2126	
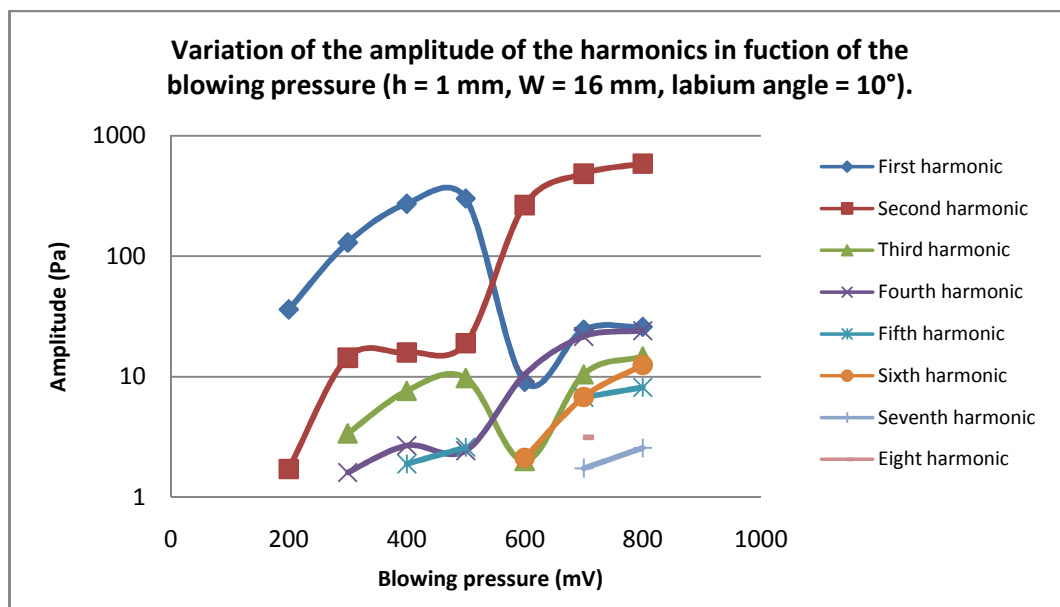
Figure 42: Variation of the amplitude of the harmonics in function of the blowing pressure (h = 1 mm, W = 16 mm, labium angle = 10°).

In paragraph 2.2.3, it was already stated that the frequency spectrum is very dependent on the mouth configuration. Therefore, the influence of variations in mouth width, flue height and labium angle on the sound spectrum was studied. Table 7 and Figure 43 respectively show the variation of the frequency and amplitude of the harmonics in function of the mouth width. Similar conclusions as for the dependency of the blowing pressure can be made. For high mouth widths, the fundamental tone is the one expected from the geometric properties of the resonator. Higher harmonics are present in the spectrum, though in more restricted amount. Lowering the mouth width increases the frequency of the harmonics. Again this can be explained by considering equation 2.4; next to its dependency on the blowing pressure, the frequency is inversely proportional to the mouth width. This trend is valid for mouth widths higher than 14 mm; lower values cause the pipe to overblow. This transition can be clearly observed on Figure 43. Again, the amplitudes of the odd harmonics diminish, while those of the even harmonics significantly increase.

Table 7: Variation of the frequency of the harmonics in function of the mouth width
(Blowing pressure = 500 mV, h = 1 mm, labium angle = 10°).

Mouth width (mm)	First harmonic (Hz)	Second harmonic (Hz)	Third harmonic (Hz)	Fourth harmonic (Hz)	Fifth harmonic (Hz)	Sixth harmonic (Hz)
23	304	608	911	1214		
22	306	611	917	1222		
21	307	614	920	1227	1533	
20	309	617	925	1234	1543	
19	309	617	925	1233	1541	
18	310	618	927	1236	1545	
17	311	6221	931	1241	1551	
16	313	625	937	1249	1561	
15	312	622	933	1244	1555	
14	303	595	889	1189		1783
13	304	605		1209		1813
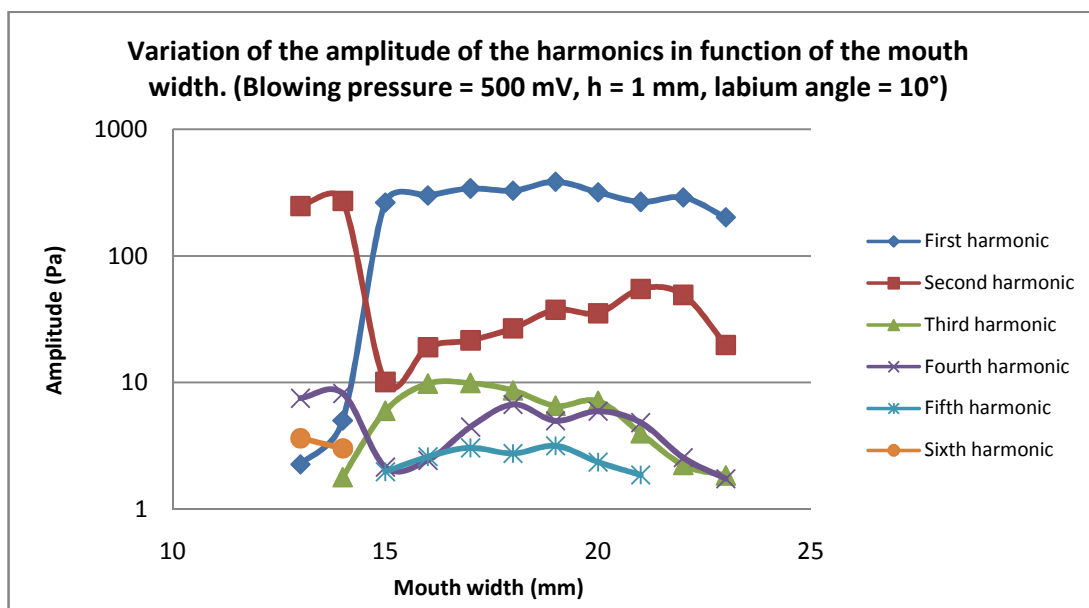
Figure 43: Variation of the amplitude of the harmonics in function of the mouth width
(Blowing pressure = 500 mV, h = 1 mm, labium angle = 10°).

The same measurements were performed for labia with angles of 20° and 30°. The patterns of the frequencies and amplitudes closely agree with the ones showed in the previous table and figure and were therefore not fully reproduced here. Table 8 shows the frequencies present in the spectrum for different labium angles for a mouth width of 16 mm, while Figure 44 shows their amplitudes. The table shows that, increasing the labium angle increases the frequency of the harmonics. This trend was also observed for other mouth widths. The amplitudes do not change significantly, and certainly no trend was observed.

Table 8: Variation of the frequency of the harmonics in function of the labium angle
(Blowing pressure = 500 mV, h = 1 mm, W = 16 mm).

Labium angle (°)	First harmonic (Hz)	Second harmonic (Hz)	Third harmonic (Hz)	Fourth harmonic (Hz)	Fifth harmonic (Hz)
10	310	618	927	1236	1545
20	311	620	931	1241	1551
30	313	624	936	1248	1559
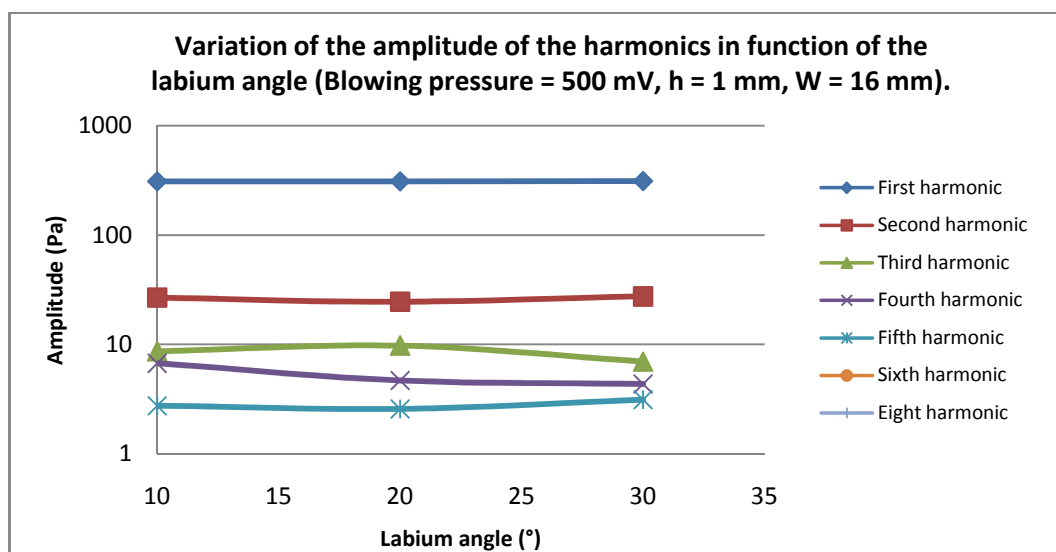
Figure 44: Variation of the amplitude of the harmonics in function of the labium angle
(Blowing pressure = 500 mV, h = 1 mm, W = 16 mm).

The last parameter of the mouth configuration that can be varied is the flue height. This parameter could only be varied from 1 mm to 2 mm; no sound was generated for higher values. Table 9 shows that for a broader flue height, less higher harmonics are present in the spectrum, and that the frequency of the harmonics is lower than for a narrow flue height. This could be expected from the above measurements; narrowing the flue height at a constant blowing pressure has the same effect as increasing the blowing pressure for at a constant flue height; it both increases the jet velocity, which is determinative for the frequency as discussed before. Furthermore, Figure 45 shows that the amplitude of the harmonics increases significantly for smaller flue heights, a similar trend as was observed for increasing blowing pressure.

Table 9: Variation of the frequency of the harmonics in function of the flue height
(Blowing pressure = 500 mV, W = 16 mm, labium angle = 10°).

Flue height (mm)	First harmonic (Hz)	Second harmonic (Hz)	Third harmonic (Hz)	Fourth harmonic (Hz)	Fifth harmonic (Hz)
1	313	625	937	1249	1561
2	297	593			

Figure 45: Variation of the amplitude of the harmonics in function of the flue height
(Blowing pressure = 500mV, W = 16 mm, labium angle = 10°).

5.2.2.2 Stopped pipe

The same measurements were performed for a stopped pipe. In general, the stopped pipe produces a less bright sound as the open pipe does; this is expected, as a stopped resonator only generates odd harmonics. Table 10 and Figure 46 show the results of the acoustic measurements for different blowing pressures. In general, the sound produced by the stopped pipe sounded noisier than that produced by the open pipe. Because of the high noise level, harmonics higher than the fifth harmonic could not be clearly distinguished. They are therefore not listed in the table. For a blowing pressure corresponding to a signal amplitude of 200 mV, a pure tone of 139 Hz is generated. Increasing the pressure locks in more harmonics. As seen for the open pipe, for higher pressures the frequency of the harmonics increases, corresponding to equation 2.4. An important difference with the previous measurements, is that in the case of a stopped pipe, the transition to overblowing occurs very smooth, while for the open pipe, the increase in amplitude of the second harmonic and the corresponding decrease in amplitude of the fundamental frequency occurred very abrupt. The actual overblowing only starts from a pressure of 1200 mV; then the produced pitch sounds one octave higher, but already from a pressure of 1000 mV, the amplitude of the fundamental tone starts decreasing slowly.

Table 10: Variation of the frequency of the harmonics in function of the blowing pressure
(h = 1 mm, W = 25 mm, labium angle = 10°).

| Blowing pressure (mV)	First harmonic (Hz)	Third harmonic (Hz)	Fifth harmonic (Hz)
200	139		
300	170	507	
400	174	521	
500	176	527	877
600	178	533	887
700	180	537	888
800	181	540	877
900	181	542	882
1000	182	543	891
1100	181	478	897
1200	180	490	848
1300	181	500	997
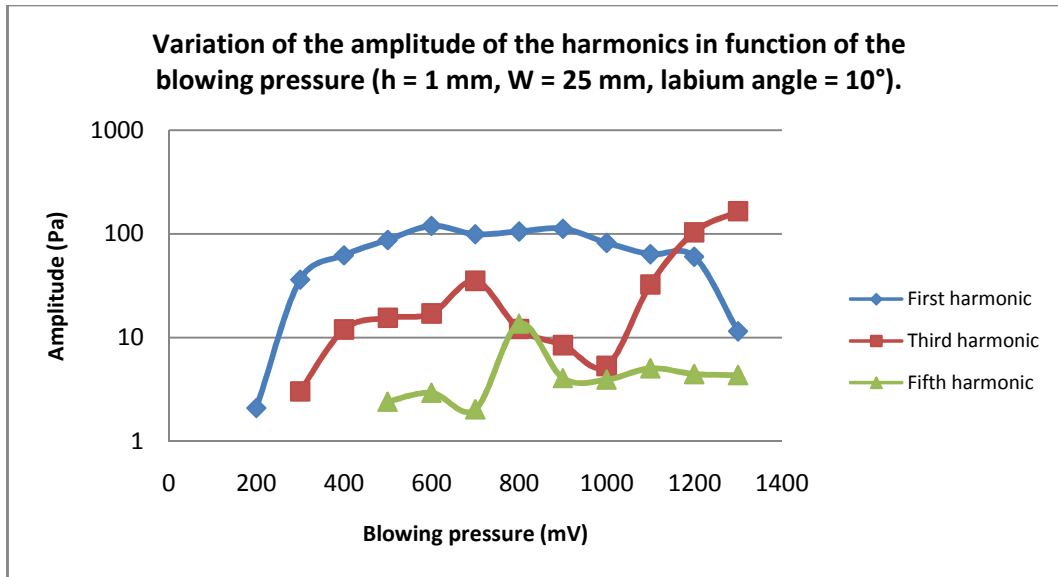
Figure 46: Variation of the amplitude of the harmonics in function of the blowing pressure
(h = 1 mm, W = 25 mm, labium angle = 10°).

The conclusions for the variation of the frequency spectrum as a function of the mouth width are similar. Table 11 shows that for broad mouth widths, only the fundamental tone and the first overtone are present. Lowering the mouth width introduces a third harmonic, and causes the frequency of the harmonics to increase. As soon as the mouth width is decreased to a value of 19 mm, the importance of the fundamental frequency starts to diminish. Simultaneously, the amplitude of the first overtone starts to increase, but only when the mouth width is further decreased to a value of 16 mm, it takes over from the fundamental frequency and a sound with higher pitch is produced.

Table 11: Variation of the frequency of the harmonics in function of the mouth width
(Blowing pressure = 500 mV, h = 1 mm, labium angle = 10°).

| Mouth width (mm)	First harmonic (Hz)	Third harmonic (Hz)	Fifth harmonic (Hz)
28	175	524	
27	176	526	
26	176	527	877
25	176	527	877
24	177	528	879
23	178	531	884
22	178	531	884
21	178	531	
20	178	533	860
19	179	534	868
18	177	430	865
17	176	455	909
16		480	
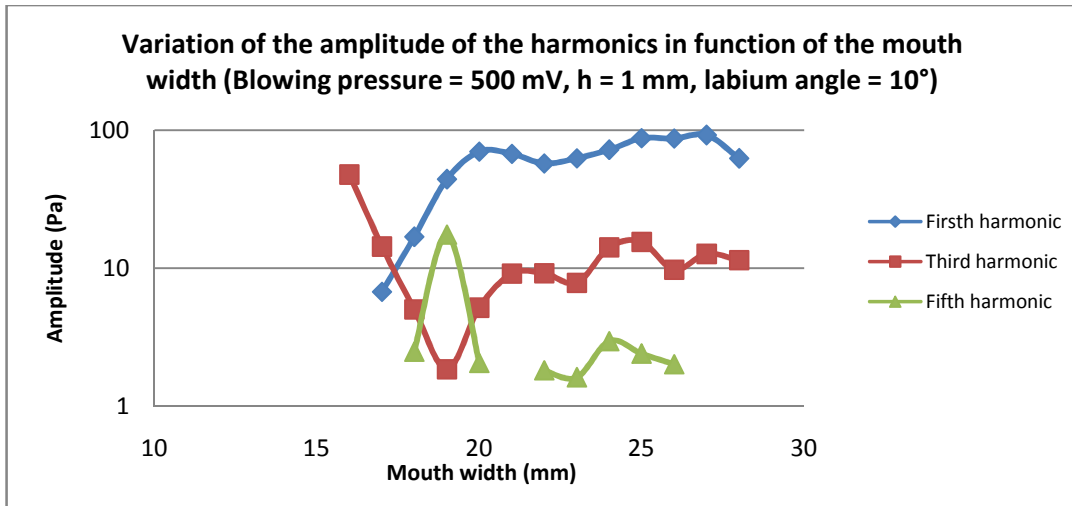
Figure 47: Variation of the amplitude of the harmonics in function of the mouth width (Blowing pressure = 500 mV, h = 1 mm, labium angle = 10°).

The measurements for different labia gave similar results. In contrast to the open pipe, the frequency of the harmonics did not increase for increasing labium angle. No trend for the variation of the spectrum in function of this mouth parameter was observed.

The influence of the slit height is similar as for the open pipe; narrow flues produce a bright sound, rich in overtones, while for broader slits a spectrum is measured with a scarce amount of harmonics. In this case, even only the fundamental frequency is present for a flue height of 2 mm. Therefore, the behavior of the frequencies and amplitudes could not be thoroughly studied. Only a formulation of the trend of the fundamental frequency is possible; an increases in both frequency and amplitude if the flue height is narrowed. This behavior however agrees with that observed in the case of the open pipe, and is theoretically supported by equation 2.4.

Table 12: Variation of the frequency of the harmonics in function of the flue height
(Blowing pressure = 500 mV, W = 25 mm, Labium angle = 10°).

Flue height (mm)	First harmonic (Hz)	Third harmonic (Hz)	Fifth harmonic (Hz)
1	176	527	877
2	169		

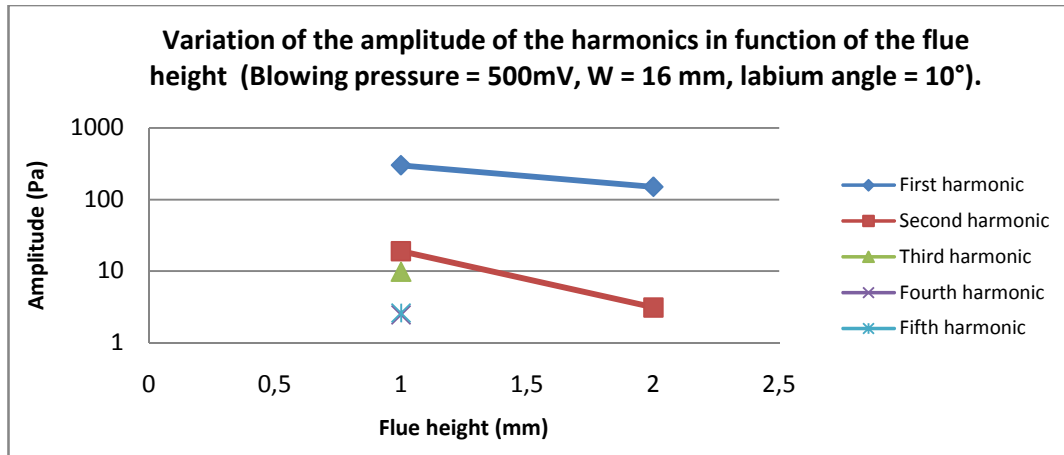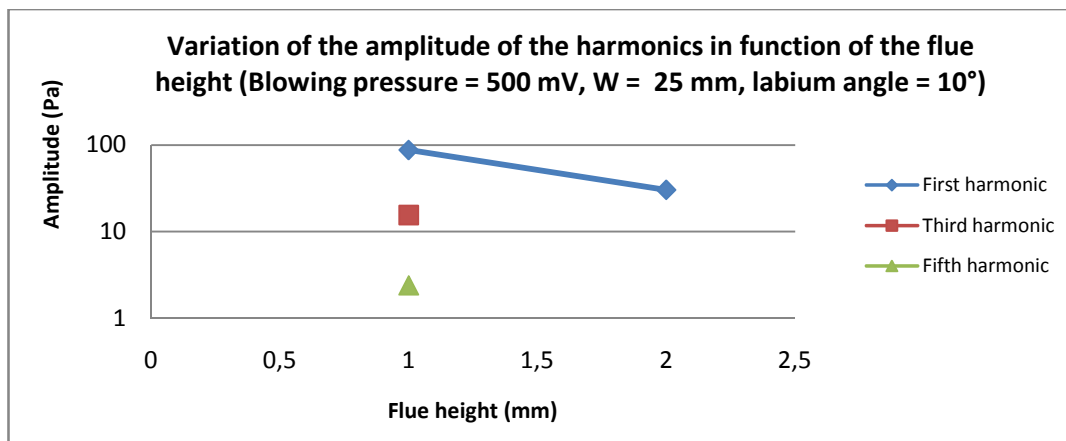**Figure 48:** Variation of the amplitude of the harmonics in function of the flue height
(Blowing pressure = 500 mV, W = 25 mm, labium angle = 10°).

5.2.3 Laser Doppler Vibrometry

5.2.3.1 Technique

Laser Doppler Vibrometry is an optical measurement technique, based on the Doppler Effect. In classical applications, it is used for the measuring of the velocity of vibrating objects. Therefore, a light beam is pointed at the target. The relative displacement of the object with respect to the light source ΔL_g caused by the vibration leads to a Doppler shift. If the object is moving with a velocity v, and the angle between the light beam and the normal to the object is β, the shift between the transmitted frequency f_0 and the measured frequency of the reflected beam f_m is:

$$\Delta f_{Dg} = f_d = f_m - f_0 = \frac{2v}{\lambda} cos\beta \tag{5.1}$$

Both the transmitted and measured frequencies are too high to be followed by a photo-detector. The superposition of the two signals however, results in a beat with frequency f, which can be detected. Therefore, in a practical set-up (Figure 49), a laser beam is divided in two coherent light beams by means of a beam splitter. The frequency of the so called reference beam stays unchanged, whereas the test beam is pointed to the object, and will undergo the frequency shift. The superposition of the signals is a beat with frequency $f_m - f_0$. But, in this way, a velocity with opposite direction gives rise to the same beat frequency. Therefore, the frequency of the test beam is shifted by a constant frequency f_b by means of a Bragg cell. Now, if the plate moves away from the light source, f_d will be negative, and the frequency of the beat will have the value $f_m - f_0 = f_b - |f_d|$. In the case the plate moves in the opposite direction, f_d will be positive, thus the beats frequency will be $f_m - f_0 = f_b + |f_d|$. From this signal, the value of the velocity of the plate can be calculated.
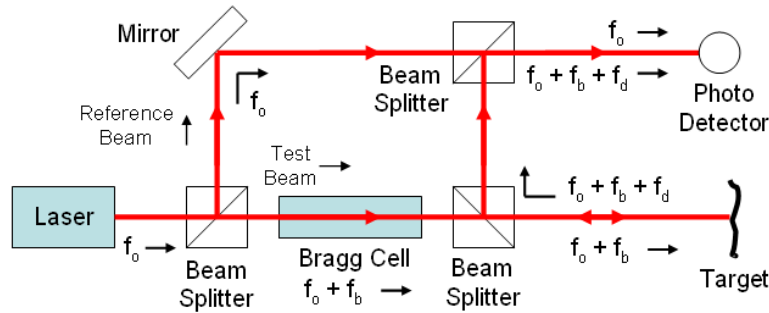
Figure 49: Set-up for the Laser Doppler Vibrometry technique. [35]

But, a vibrating object causes pressure fluctuations $\Delta p(t, x, y, z)$ in the surrounding medium, leading to fluctuations in the refractive index n:

$$\Delta n(t, x, y, z) = \frac{\partial n}{\partial p} \Delta p(t, x, y, z) \tag{5.2}$$

These variations in refractive index result in fluctuations in the optical path length:

$$\Delta L_n(t) = 2 \int_{vibrometer}^{object} \Delta n(t,x,y,z) dl \tag{5.3}$$

Just like the geometrical displacements ΔL_g, also the fluctuations in optical path length ΔL_n cause Doppler shifts. The total Doppler shift is thus the superposition of the two contributions:

$$\Delta f_{tot} = \Delta f_{Dg} + \Delta f_{Dn} = \frac{2}{\lambda} \left(vcos\beta + \frac{\partial n}{\partial p} \int_{vibrometer}^{object} \frac{d}{dt} \left(\Delta p(t, x, y, z) \right) dl \right) \tag{5.4}$$

When, as in general, the LDV technique is used to measure the velocity of a vibrating object, the contribution of the second term is negligible.

But, when instead of a vibrating object, the laser beam is pointed to an absolutely rigid reflector, the first contributor falls out, and the influence of the fluctuations in refractive index, however small, can be detected. This technique, developed by Zipser and Franke in 2007, is called Refracto-Vibrometry and can be used for the measuring and visualizing of acoustic waves in gases and liquids. A set-up for this application is show in Figure 50. The beam of a Scanning Laser Doppler Vibrometer is pointed to a rigid reflector and scans points located in an area $S = HxW$ with a preliminary defined point density. Then the area between an optionally glass plate and the reflector defines the measuring zone. [36]
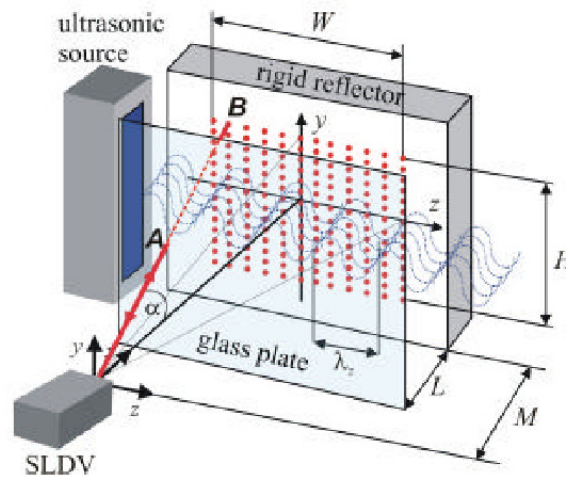
Figure 50: Refracto-Vibrometry set-up.
A laser pointed to a rigid reflector scans all point located in the surface WxH.
The test zone with width L is located between the (optionally) glass plate and the reflector. [36]

By replacing the ultrasonic source in Figure 50 by the organ pipe, the frequency spectrum of the produced sound can be determined. Figure 51 shows the schematic representation of the set-up used for the LDV measurements. The organ pipe *(6)* was placed between a rigid reflector *(5)* and a Laser Doppler Vibrometer *(7)*. It was driven by compressed air *(1)*, which was supplied to the pipe by means of a servo valve *(4)*, as was described in paragraph 5.1.
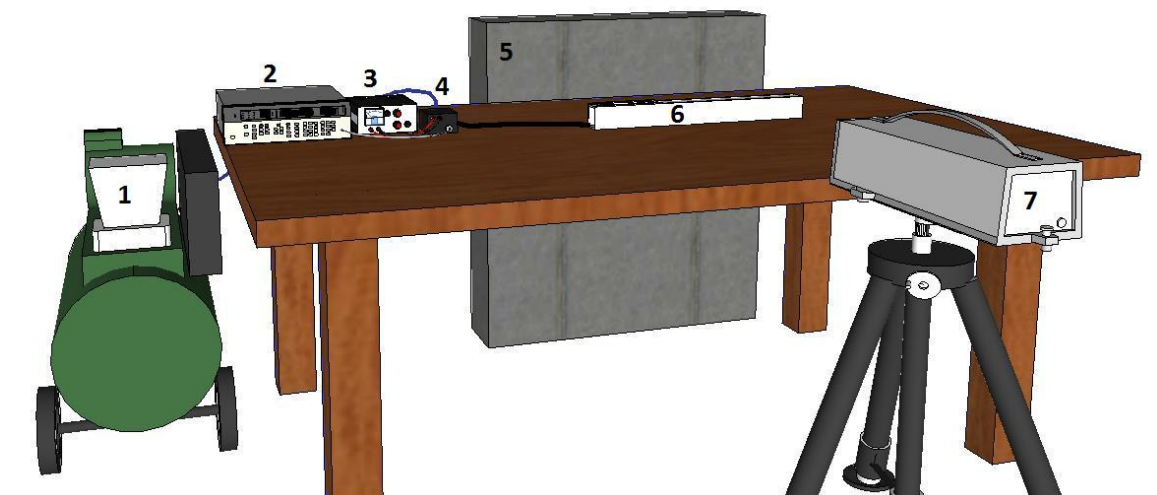
1. Compressor   *4. Servo valve*   *7. Laser Doppler Vibrometer*
2. Signal generator   *5. Rigid reflector*
3. DC power supply   *6. Organ pipe*

Figure 51: Schematic representation of the LDV set-up.

5.2.3.2 Results

The characteristics of the sound spectrum emitted by an open pipe, driven by a control signal with an amplitude of 300 mV are shown in Table 13 and Figure 52. When the frequencies are compared with those listed in Table 6 for the same blowing pressure, a good agreement is observed. The amplitude of the harmonics is expressed in µm/s, but can be converted to Pascal by using equation 5.4. Some qualitative conclusions can however be made without performing this complex conversion. The first harmonic is present in a high amount, as expected, and the relative strength of the overtones is similar as observed for the acoustic measurements. In this case however, the amplitude of the third harmonic is somewhat higher than the second; an unexpected characteristic which was not observed for the previous measurements.

Table 13: Sound spectrum emitted by an open pipe, measured with the LDV technique
(Blowing pressure = 300 mV, W = 24 mm, labium angle = 10°).

	First harmonic	Second harmonic	Third harmonic	Fourth harmonic	Fifth harmonic
Frequency (Hz)	306	612	918	1224	1530
Amplitude (µm/s)	100	14.29	17.86	0.95	0.595
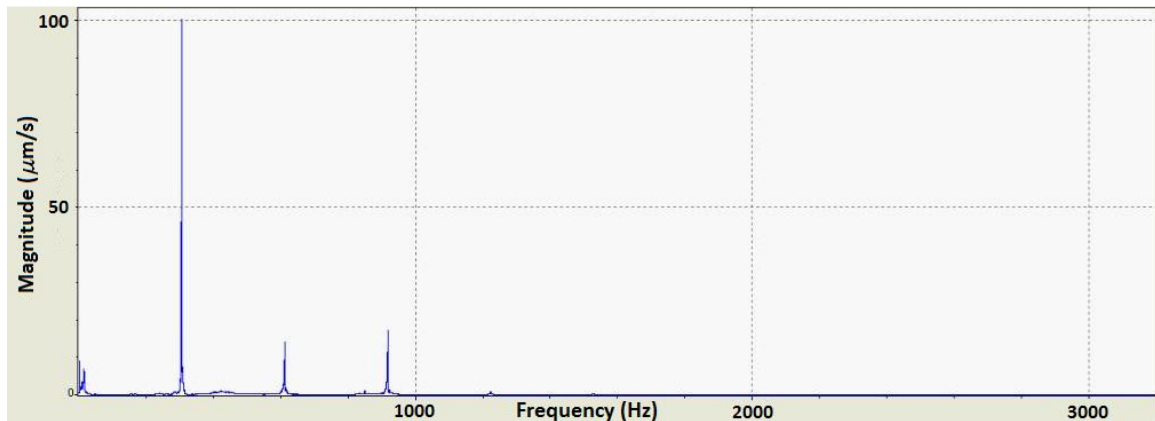
Figure 52: Sound spectrum emitted by an open pipe, measured with the LDV technique
(Blowing pressure = 300 mV, W = 24 mm, labium angle = 10°).

5.3   Flow visualization

5.3.1   Schlieren visualization

While setting op the Schlieren configuration for the organ pipe measurements, all the characteristics of the set-up observed and described in the previous chapter were taken into account. In order to make the flow more visible, and thus to minimize the minimum discernable contrast in the image, the halogen illuminator was replaced by a Diode-Pumped, Q-Switched Nd:YLF laser. Figure 30 indeed shows that the minimum noticeable contrast is lowered because of that action; the background illuminance corresponding to the tungsten-halogen lamp was in equation 4.9 calculated to be 31.3 cd/m². When observing this value on Figure 30, it seems that for this region, the minimum contrast discernable by the human eye is a decreasing function of the background illuminance. Since the use of the Nd:YLF laser will increase the illuminance significantly, the characteristics of the flow will be more visible on the produced image. All other components and its positions remained unchanged. Figure 53 shows a schematic representation of the Schlieren set-up used for the organ pipe measurements. The pipe *(7)* is driven by CO_2 *(1)*, which is supplied by means of the servo valve *(4)*. As required, the laser *(5)* is placed at a distance of 647.7 mm in front of the first field mirror *(6)*, i.e. at its focal distance. The second field mirror *(8)* is placed at a distance of 1500 mm from the first mirror, and the pipe is placed in between. The knife edge

(9) was placed at a distance of 647.7 mm from the second field mirror. The obtained image was captured on the screen *(10)* and recorded by a high speed camera *(11)*.

1. CO_2 bottle
2. Signal generator
3. DC Power supply
4. Servo valve
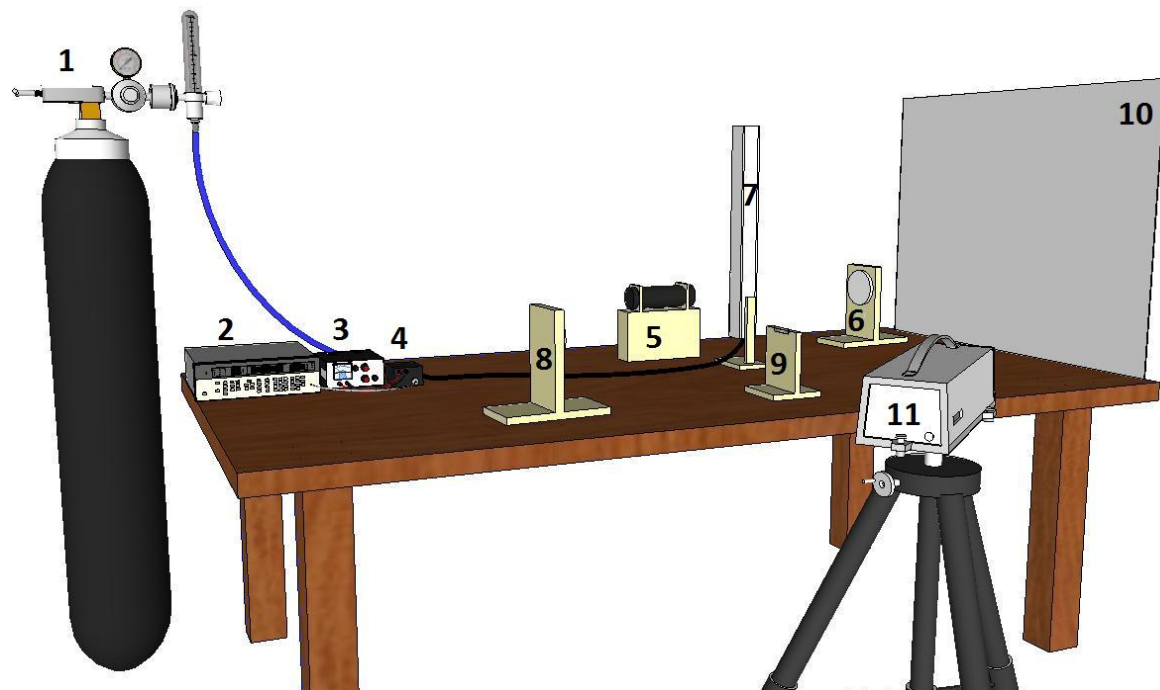
5. Laser
6. First parabolic mirror
7. Organ pipe
8. Second parabolic mirror
9. Knife edge

10. Screen
11. Camera

Figure 53: Schematic representation of the Schlieren set-up.

Because the flow visualization is better observable on a moving image, all the Schlieren recordings, discussed below, are added as AVI file on the accompanying CD, whereof the exact contents can be found in Appendix B

5.3.1.1 Transient State

The initialization of the sound, called the attack transient, has a major importance in the subjective perception of the tone. It contributes to the ability for a listener to discriminate between tones having the same pitch, loudness and duration, played by different instruments. Experiments have made clear that, if the attack is removed from the sound signal, identification accuracy is greatly decreased, while removing the steady state or decay has little influence. [37], [38]. During the attack, a sound with a higher amount of higher frequency components compared to the steady state is generated; often, the transient is dominated by the first overtone, i.e. the second harmonic for open pipes and the third for stopped pipes. The speed of the attack is determined by the rate of pressure rise in the pipe foot, and thus by the valve opening speed. A steep pressure rise results in an earlier contact with the labium; lowering the rate of pressure rise delays the jet hitting the labium. [18], [39]. To investigate this effect, three different signals were applied on the servo valve controlling the CO_2 supply: a square wave, a sine wave and finally a saw wave. Also the differences in flow pattern for an open and closed pipe were studied. Figure 55 shows the flow visualization for the first milliseconds of the attack transient for an open organ pipe, resulting from the three different control signals. Figure 56 shows the case of a stopped pipe. The images from each series are equally spaced in time, but the time step varies for the different series; all images were ranked so that the jet reaches the labium at about the fifth image. Figure 54 clarifies the part of the organ pipe shown in the pictures; the flow is emanating from the flue at the left side of the picture, and travels to the right, towards the labium.
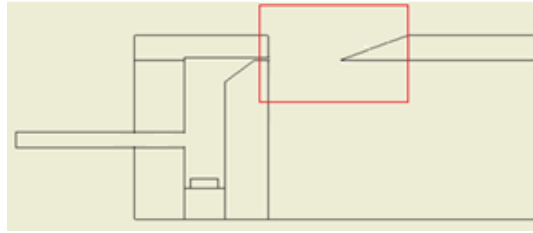
Figure 54: Illustration of the part visualized on the following images.

Square wave	Sine wave	Saw wave

$t = 0.0005\,s = \frac{1}{7}T$

$t = 0.0070 = 2T$

$t = 0.0140s = 4T$

$t = 0.0015\,s = \frac{3}{7}T$

$t = 0.0140\,s = 4T$

$t = 0.0280\,s = 8T$

$t = 0.0025\,s = \frac{5}{7}T$

$t = 0.0210\,s = 6T$

$t = 0.0420\,s = 12T$

$t = 0.0035\,s = \frac{7}{7}T$

$t = 0.0280\,s = 8T$

$t = 0.0560\,s = 16T$

$$t = 0.0045\ s = \frac{9}{7}T$$

$$t = 0.0350\ s = 10T$$

$$t = 0.0700\ s = 20T$$

$$t = 0.0055\ s = \frac{11}{7}T$$

$$t = 0.0420\ s = 12T$$

$$t = 0.0840\ s = 24T$$

$$t = 0.0065s = \frac{13}{7}T$$

$$t = 0.0490\ s = 14T$$

$$t = 0.0980s = 28T$$
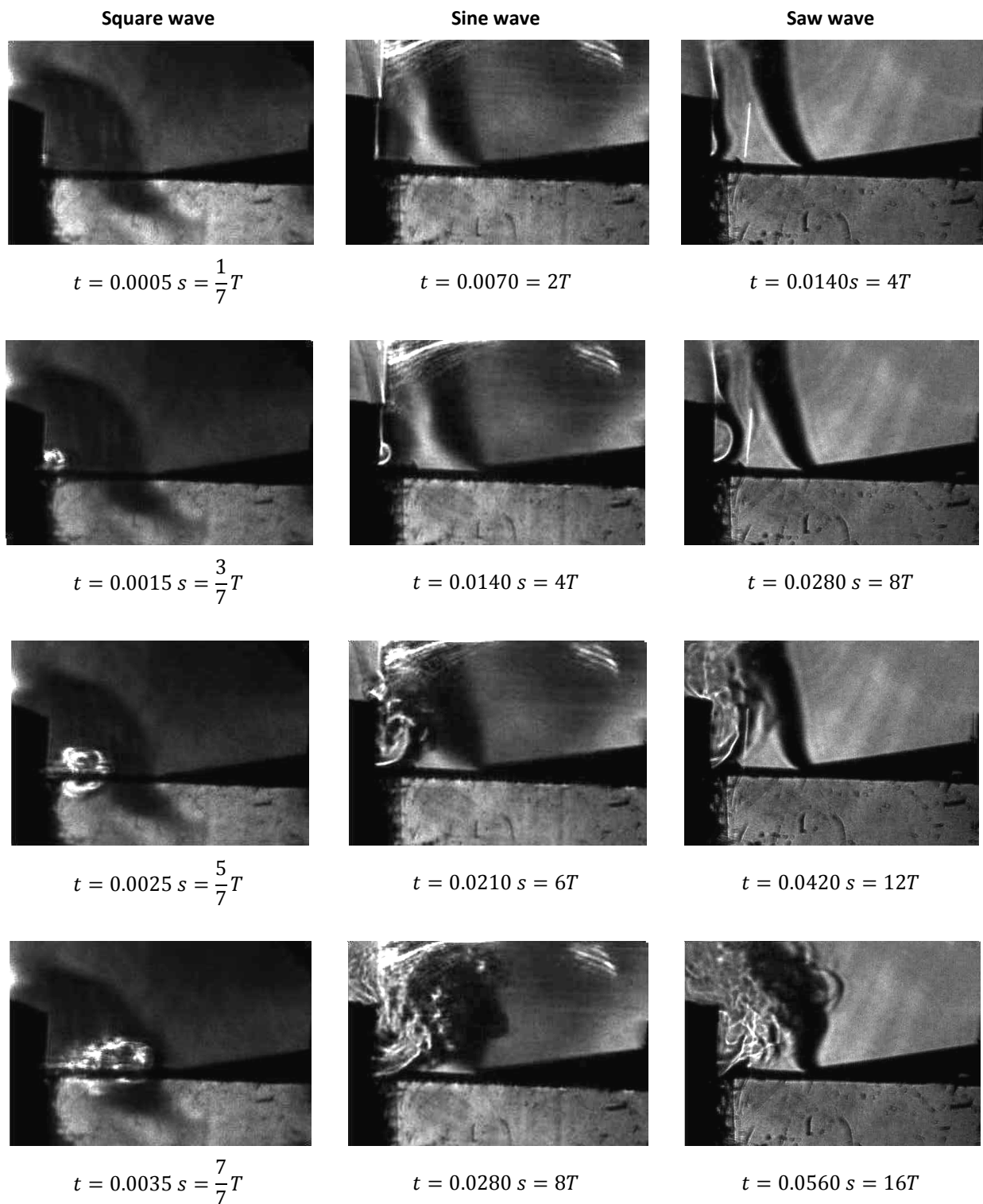
Figure 55: Flow visualization of the transient state of the air jet in an open organ pipe for three different blowing pressure signals (h = 1 mm, W = 16 mm, labium angle = 10°).

When observing Figure 55, it is clear that the above statement is true; the faster the pressure rise in the pipe foot, the faster the evolution of the flow in the pipe mouth. It takes the sine wave about 7 times longer than the square wave to travel a same longitudinal distance. The saw wave demands a time double of that of the sine wave. The first set of pictures shows the start of the jet emanating from the flue. The dark spot emerging from the top of the labium is CO_2 that is left in the pipe during the previous cycle. The flow patterns induced by the different signals show large differences; while the jet is pointed straight to the labium for the square wave, it is curved to the exterior of the pipe for the other two signals. The deviation is largest when a saw wave is applied; one can conclude that the slower the pressure in the foot pipe is raised, the larger the curvature of the jet will be. This result was also experimentally observed and qualitatively proven by means of a simplified acoustic model by Verge et al [18]. Because of its straight path, the flow induced by the square wave immediately hits the labium, at about 4 milliseconds after opening the valve. But for a slower opening of the valve, the flow at first misses the labium because of the strong outward deflection. The contact with the labium results in a vortex shedding, which has a strong influence on the relative magnitudes of the second and higher harmonics [16]. After a while, oscillations with the fundamental frequency imposed by the resonator are developed, and the quasi steady state is set in. The time need to reach these steady oscillations depends on the imposed control signal: for the square wave it takes circa 4 – 5 periods of the fundamental mode, for the other signals, a longer period is needed. Another characteristic, dependent of the control signal, is the laminar/turbulent behavior of the

flow. The second image for the sine and saw wave show a clear laminar flow path, while for the square wave, the flow is already almost turbulent when leaving the flue. The observed laminar patterns however disappear relatively fast when turbulence gradually appears and washes out the coherent two-dimensional structures. On the third set of images, the tail of the flow has already become turbulent, while the part of the jet close to the flue is still ordered. But some periods later, turbulence has fully replaced the laminar pattern.

For a stopped organ pipe, the flow pattern is somewhat different (Figure 56). For the square wave, no important differences are observed. The flow is also directed straight to the labium, and again reaches it at about 4 milliseconds after the valve opening. Like for the open pipe, the flow is already quite turbulent when leaving the flue exit. On the contrary, the sine wave gives rise to a flow pattern that differs significantly from that observed for an open pipe. As for the square wave, the flow follows a straight path when leaving the pipe flue, and is not deflected to the exterior of the pipe. Therefore, the flow is pointed directly to the labium, and the contact is achieved much earlier than in the case of the open pipe. The flow stays laminar, even after the hitting of the labium. But regarded in absolute time, the turbulence effects start at exact the same point of time. When a saw wave is used to drive the servo valve, the flow is deflected to the outwards of the pipe, as observed in the case of the open pipe. In this case however, the deflection is less strong, and the flow is straightened much earlier. Between 56 and 70 ms after the zero crossing of the signal, an abrupt change of direction happens; the flow is seemed to be pulled to the center, and continues a path parallel to the flue axis. Because of the slow longitudinal progress, the flow is already turned turbulent before reaching the labium. This however happens at the same point of time as for the open pipe.

Square wave	**Sine wave**	**Saw wave**
$t = 0.0005\ s = \dfrac{1}{14}T$	$t = 0.0025\ s = \dfrac{5}{14}T$	$t = 0.0140 = 2T$
$t = 0.0015\ s = \dfrac{3}{14}T$	$t = 0.0050\ s = \dfrac{10}{14}T$	$t = 0.0280\ s = 4T$

$$t = 0.0025\,s = \frac{5}{14}T \qquad t = 0.0075\,s = \frac{15}{14}T \qquad t = 0.0420\,s = 6T$$

$$t = 0.0035\,s = \frac{7}{14}T \qquad t = 0.0100\,s = \frac{20}{14}T \qquad t = 0.0560\,s = 8T$$

$$t = 0.0045\,s = \frac{9}{14}T \qquad t = 0.0125\,s = \frac{25}{14}T \qquad t = 0.0700\,s = 10T$$

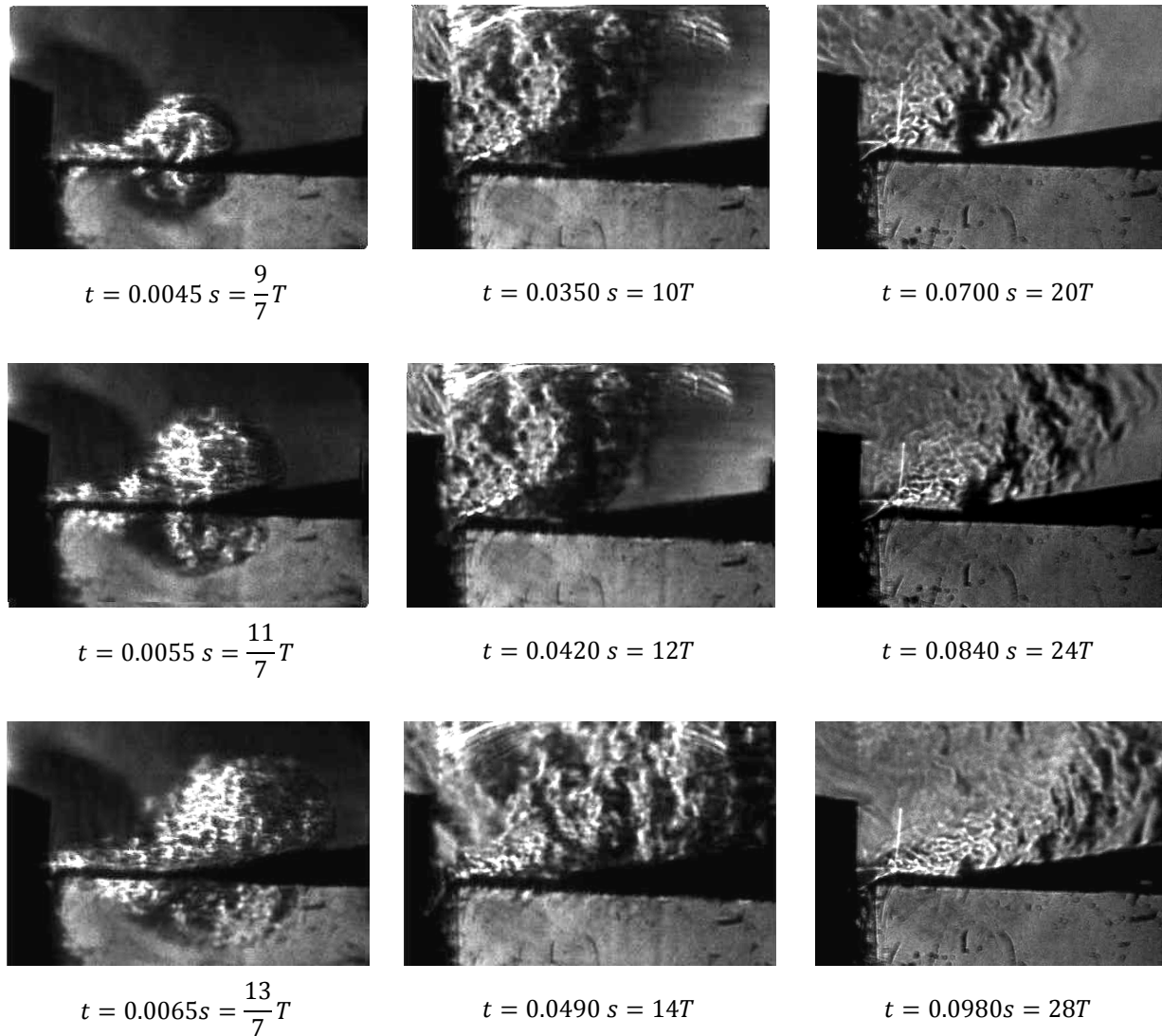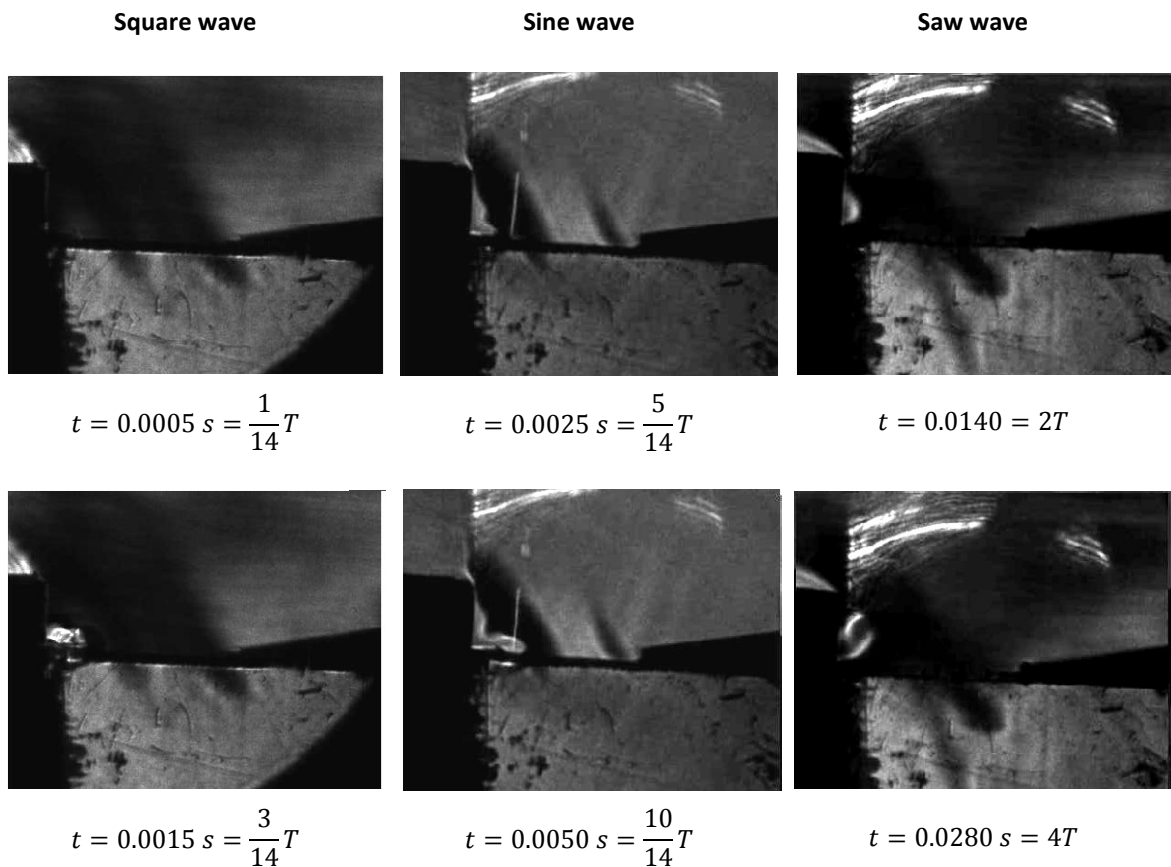$$t = 0.0055\,s = \frac{11}{14}T \qquad t = 0.0150\,s = \frac{30}{14}T \qquad t = 0.0840\,s = 12T$$
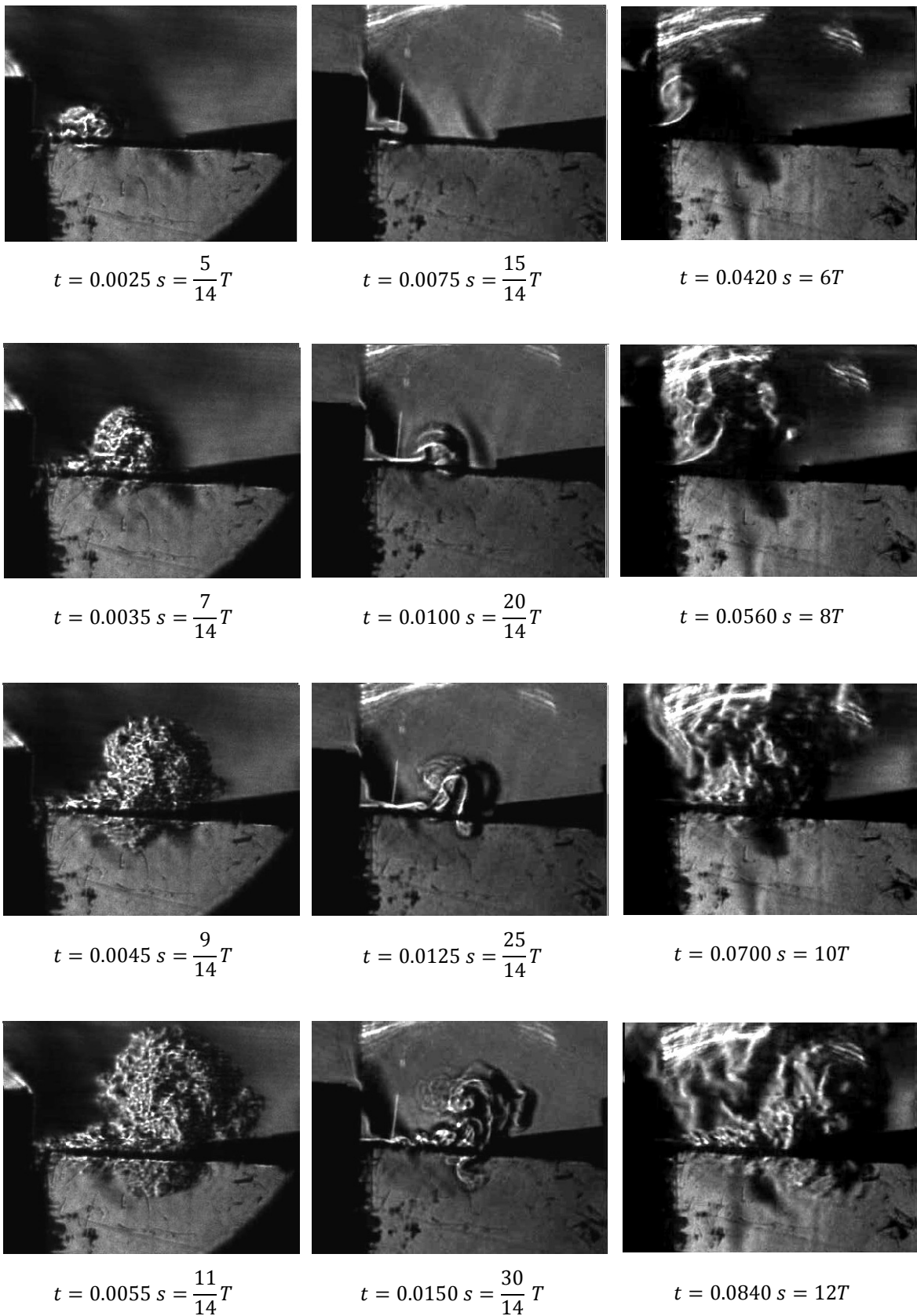
Figure 56: Flow visualization of the transient state of the air jet in a stopped organ pipe for three different blowing pressure signals (h = 1 mm, W = 25 mm, labium angle = 10°).

The difference in flow path for an open and stopped pipe was also observed by Paál et al. [1]. They assumed the difference in flue geometry, used for the open and stopped pipe to be the cause of that behavior. However, for the measurements shown above, a complete equal flue geometry was used, and therefore this cannot be the cause.

It can thus be concluded that for a stopped pipe, a phenomenon is present, that holds the emanating air jet close to the flue axis and prevents it from deflecting to the exterior. This phenomenon is sensitive to the rate of pressure rise in the pipe foot and is not present in the case of an open pipe. This conclusion is very important for the understanding of the choice of mouth widths. By experience, it is know by organ builders that there is a major difference in optimal mouth widths for open and closed pipes. Organ builder De Greef [40] observed that the mouth width for an open pipe has to lie in the range of 24-27% of the labium width, while a stopped pipe can only produce a strong and pure tone if a higher mouth width is used; about 35-40% of the labium width.

The velocity distribution of a jet emerging from a flue was analyzed by Förtmann [41]. He studied the velocity profile of a jet emerging from a rectangular nozzle of 0.03 high and 0.65 m wide at different distances from the flue, i.e. different x-positions. Förtmann's quantitative results, plotted in Figure 57, were used by De Greef [40] to obtain a sketch of the velocity distribution, expressed in terms of percentage of the jet velocity (Figure 58). The jet leaves the flue with a uniform velocity $v_j = 35 \, m/s$. Because of the friction caused by the surrounding air molecules, the velocity is gradually diminished. The region of fluid close to the flue exit, which maintains the jet velocity is called the core of the jet. The length of this core is dependent of the shape of the nozzle and the amount of turbulence, and varies between 3 - 7 times the flue height. The boundary layer, which consists of fluid whereof the velocity is influenced by the stationary air molecules, grows for increasing x-coordinates because of the increscent mixing, while off course the maximum velocity correspondingly decreases.
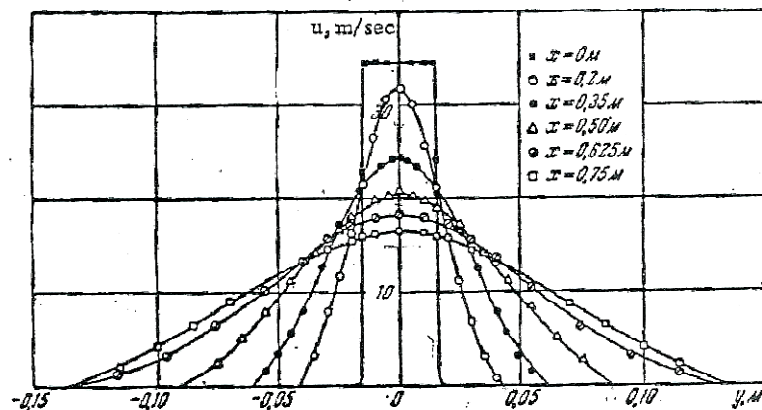
Figure 57: Velocity profiles at different sections of a plane jet. [41]
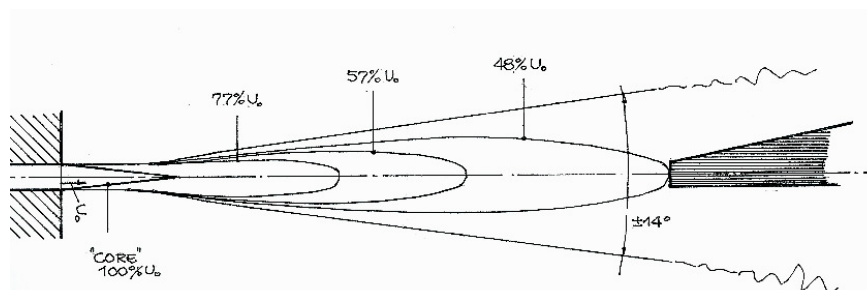
Figure 58: Velocity distribution of an emanating jet. [40]

The velocity at which the jet hits the labium is important for the sound production. A too high velocity causes the pipe to overblow, while a too low velocity gives rise to a weak tone with the possibility of a high amount of noise. Therefore, following conclusion can then be proposed: because the jet is deflected outwards the pipe for an open configuration, the labium has to be located close enough to the flue exit in

order to give the jet the possibility to reach the labium with the desired velocity. The contact happens in the outer part of the jet, where the velocity is already diminished, despite the short travelled longitudinal distance. Moving the labium more downstream will cause the jet to hit the labium with a lower speed and introduces a weak, noisy sound, or will even prevent the jet to hit the labium, and generates no sound at all. For a closed pipe, the jet travels straight to the labium, and thus contact will be achieved with the top of the jet. Therefore, the labium has to be positioned far enough from the flue exit, so that the flow is already decelerated enough before it hits the labium. [40]

5.3.1.2 Quasi Steady state

The attack transient is followed by a steady state, which is characterized by an oscillation whereof the frequency is imposed by the geometric characteristics of the resonator. Because the behavior is not perfectly periodic, this state is called the quasi steady state. As already stated and investigated by the acoustic measurements (paragraph 5.2.2), the produced sound is sensitive to adaptations of the mouth configuration. For both the open and stopped pipe, Schlieren measurements were performed for different values of mouth width and labium angle.

5.3.1.2.1 Open pipe

First, measurements were performed using a labium with an angle of 10°. For flue heights larger than 18 mm, no sound was generated, and accordingly, no clear oscillations were observed at the mouth of the pipe. The air flow leaving the flue travels in the direction of the labium, but follows a more or less straight path. An example of such a flow is shown in Figure 59. The figures were approximately labeled in time, using the oscillation frequency expected from the geometrical properties of the resonator. The time between two pictures is 0.5 milliseconds.

$$t = \frac{1}{7}T \qquad t = \frac{2}{7}T \qquad t = \frac{3}{7}T$$

$$t = \frac{4}{7}T \qquad t = \frac{5}{7}T \qquad t = \frac{6}{7}T$$

$$t = \frac{7}{7}T$$
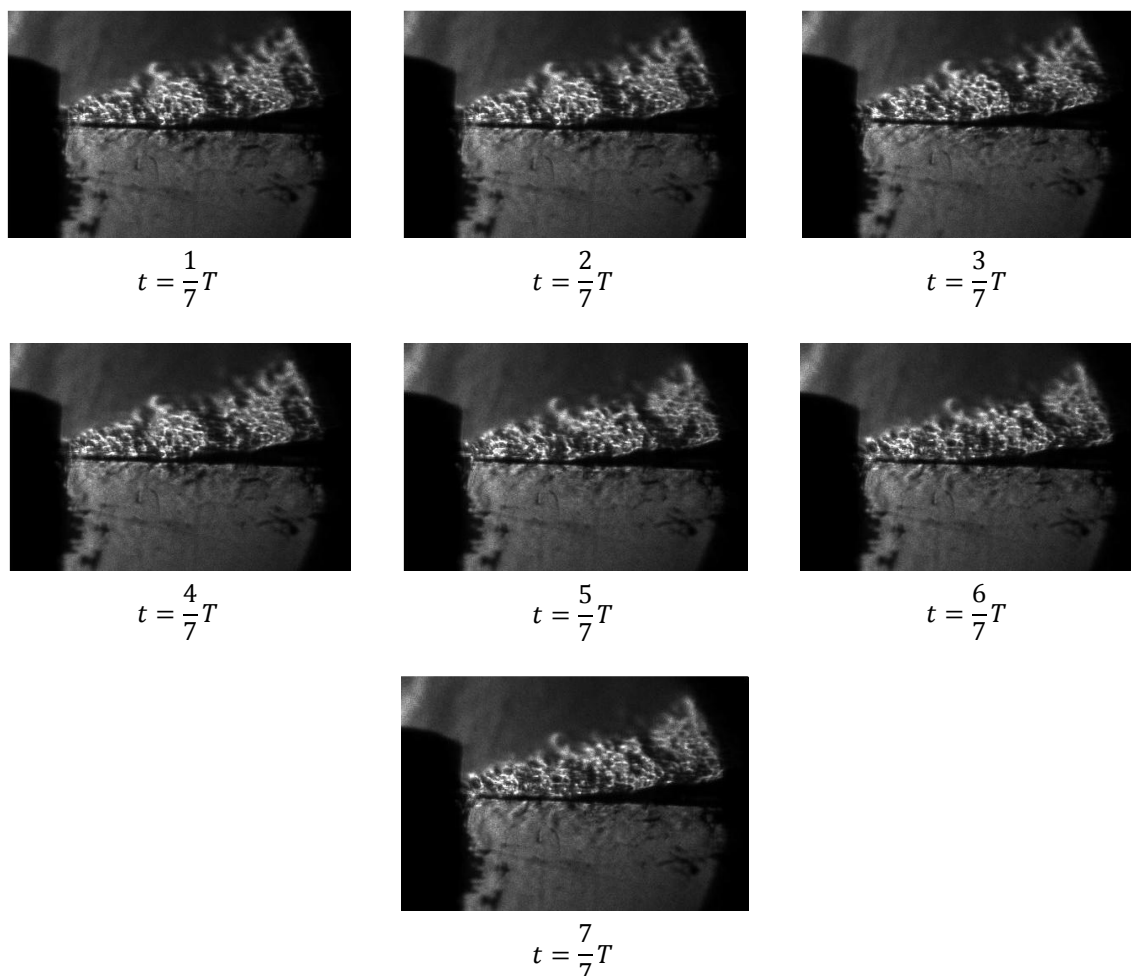
Figure 59: Visualization of the air jet in an open organ pipe, producing no sound
(h = 1 mm, W = 23 mm, labium angle = 10°).

$$t = \frac{1}{7}T$$

$$t = \frac{2}{7}T$$

$$t = \frac{3}{7}Ts$$

$$t = \frac{4}{7}T$$

$$t = \frac{5}{7}T$$

$$t = \frac{6}{7}T$$

$$t = \frac{7}{7}Ts$$
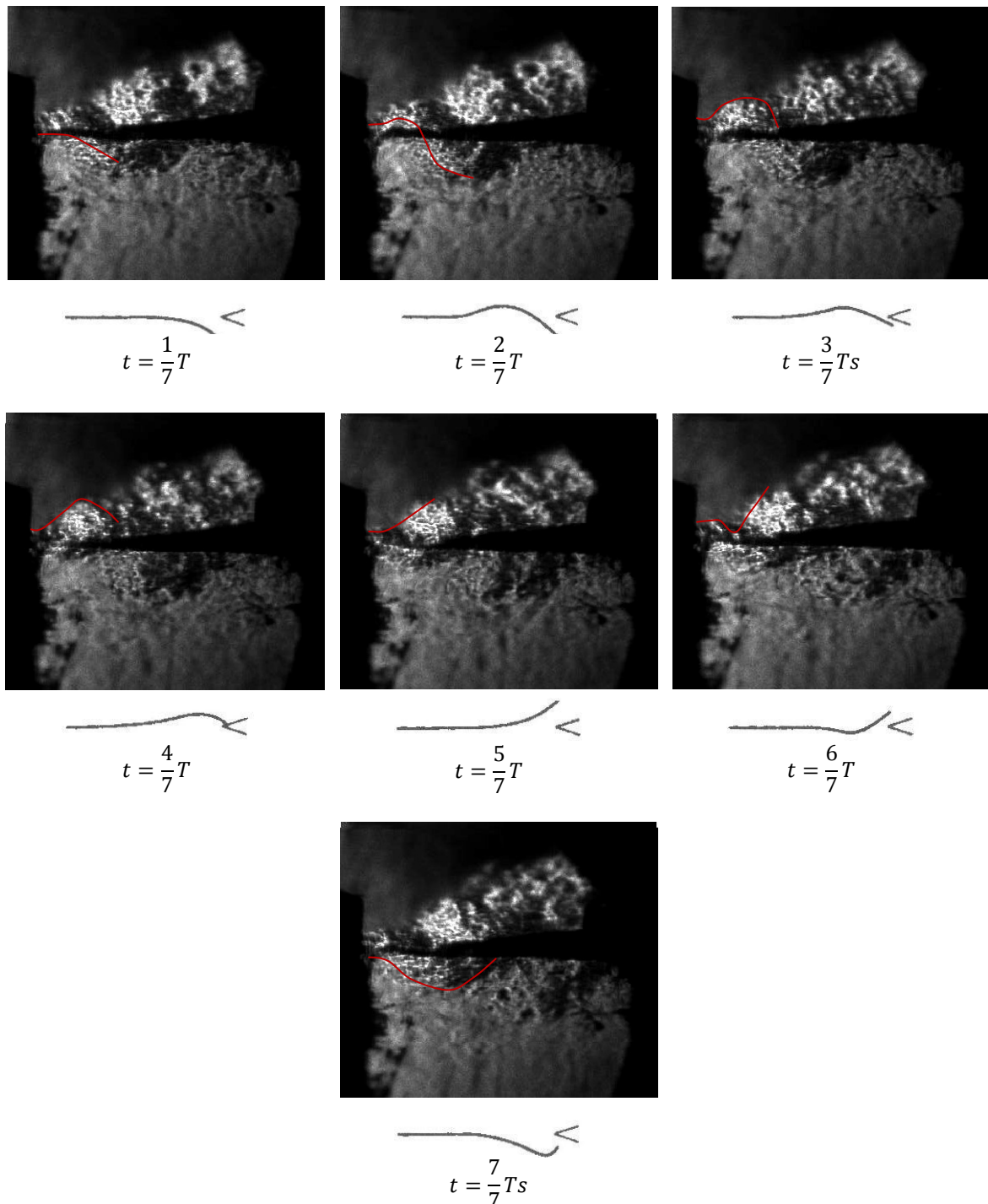
Figure 60: Visualization of one oscillation period of the air jet in an open organ pipe
(h = 1 mm, W = 16 mm, labium angle = 10°).

For mouth widths ranging from 17 mm to 10 mm, a normal sound was produced. The Schlieren measurements corresponding to these configurations clearly show the oscillations around the labium. But since the Schlieren technique is a qualitative measurement technique, no quantitative data can be extracted from the images. However the periodic behavior can be clearly seen on the recordings, the period can thus only be estimated with an accuracy equal to the time between two pictures, in this case 0.5 ms. Figure 60 shows by approximation one period of the flow oscillation measured for an open organ pipe with a mouth width of 16 mm. For clearance, the movement of the jet was denoted by a help line. In paragraph 2.2.2, the edgetone behavior was discussed, whereby the movement of a jet creating such an

edgetone was suggested by Figure 6 (b). The recordings shown below seemed to follow this behavior quite well, and therefore the corresponding phase of the movement as shown by Figure 6 (b) was added below each picture.

At $\frac{1}{7}T$, the flow leaving the flue is approximately pointed straight to the labium. The next images show how the flow is bended outwards the pipe; the maximum deflection occurs at $\frac{4}{7}T$. After that, the flow changes direction; at $\frac{5}{7}T$, the curvature of the jet is inverted and the following period, the flow is pulled inwards the pipe.

When the mouth width was further diminished below 10 mm, the pipe was overblown. As explained in paragraph 1.2.3, this phenomenon occurs when the jet velocity is too high or the mouth width to low, so that the edgetone prefers a higher frequency. Figure 61 shows the flow visualization of approximately one period of an overblown pipe. The frequency of oscillation is here twice the fundamental frequency; the feedback is thus driven by the second harmonic. The oscillation of the jet is not very clearly on the separate pictures as shown below, but could despite the very small amplitude, be well observed when the images were played after each other, as they were recorded with the high speed camera. Verge [16] observed that the oscillation amplitude decreases for too high blowing pressures, which has similar consequences as lowering the mouth width for a constant pressure. The first picture of Figure 61 shows how the jet is oriented more or less straight to the labium, with a small deflection to the outwards of the pipe. On the following picture, the jet is more deflected to the exterior, and at $\frac{3}{4}T$, the bending of the flow is inverted. The following picture should show how the flow is bended inward, but in this case, the jet does not penetrate into the inside of the pipe at all.

$$t = \frac{1}{4}T_2 \qquad t = \frac{2}{4}T_2 \qquad t = \frac{3}{4}T_2 \qquad t = \frac{4}{4}T_2$$
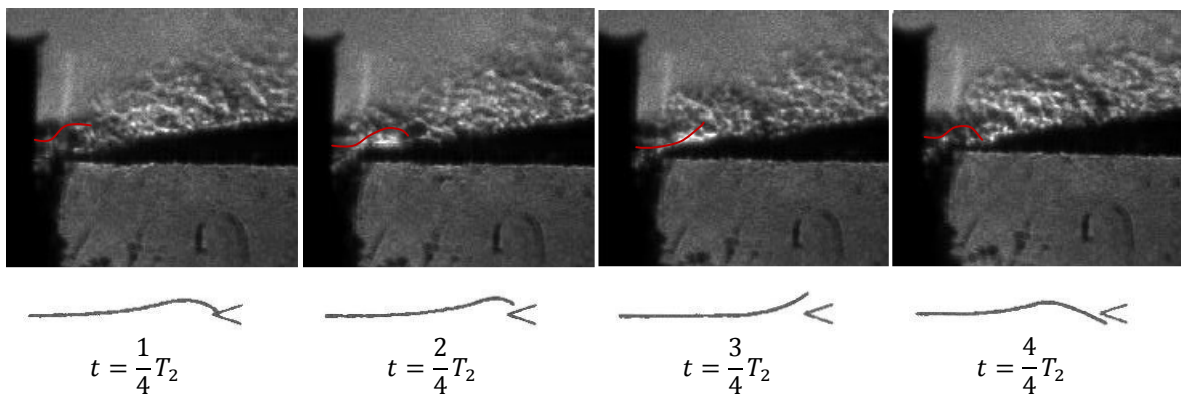
Figure 61: A too narrow mouth width causes the pipe to be overblown: the frequency of oscillation is twice the fundamental frequency (h = 1 mm, W = 9 mm, labium angle = 10°).

When comparing the influence of the mouth width on the produced tone observed during the Schlieren experiments, to the findings of the acoustic measurements, a major difference is noticed. While for the latter, a sound is already produced at a mouth width of 23 mm, the mouth width should be smaller than 18 mm for the Schlieren measurements. Also the mouth width at which overblowing occurs observed during the Schlieren measurements is a lot smaller than that noted during the acoustic measurements. The reason for that has already been addressed; the fact that for the Schlieren measurements, the CO_2 is supplied to the valve with a pressure of 2 bar, while for the acoustic measurements, the valve is fed by air with a pressure of 5 bar, gives rise to a different blowing pressure. For a higher pressure, the jet velocity, and corresponding, the velocity at which the jet hits the labium will be higher. Therefore, a sound can be produced for higher mouth widths, than possible with the lower pressure. The same conclusion can be made for the overblowing.

Similar results for the flow development were obtained for the other labia. When using the labium with the 20° angle, the pipe remained silent until the mouth width was lowered to 19 mm. Oscillations were clearly observed for heights up to 15 mm. Further lowering the space between the flue exit and the

labium again resulted in overblowing. Figure 62 shows the normal oscillation of the air jet for a mouth width of 18 mm. It can be seen how the air jet, starting from a straight position, first deflects outwards the pipe and then at $\frac{5}{7}T$ changes direction to the inwards of the pipe. The figures show clearly that the jet spends more time outwards the pipe than inwards: only for $\frac{2}{7}$ th of the period, compared to the remaining $\frac{5}{7}T$ it spends outside.

$$t = \frac{1}{7}T$$

$$t = \frac{2}{7}T$$

$$t = \frac{3}{7}T$$

$$t = \frac{4}{7}T$$

$$t = \frac{5}{7}T$$

$$t = \frac{6}{7}T$$

$$t = \frac{7}{7}T$$

Figure 62: Visualization of oscillation period of the air jet in an open organ pipe
(h = 1 mm, W = 18 mm, labium angle = 20°).

Similar results were observed by Paál et al. [1]. For comparison, one of their recordings for a similar configuration is shown in Figure 63. In this case, a cylindrical, metal organ pipe was used with a length of 458 mm. The mouth width has a value of 19.7 mm, close to the value of 18 mm which was used for Figure 62. A major difference however, is that Paal et al. choose for a labium which is straight with the flue axis at the outside of the pipe, and oblique at the interior, while in this thesis, the inverse is used. The flow pattern of the jet leaving the flue is quite similar to the recordings of Figure 62.

| $t = 0.1\,T$ | $t = 0.3\,T$ | $t = 0.5\,T$ |

| $t = 0.7\,T$ | $t = 0.9\,T$ |
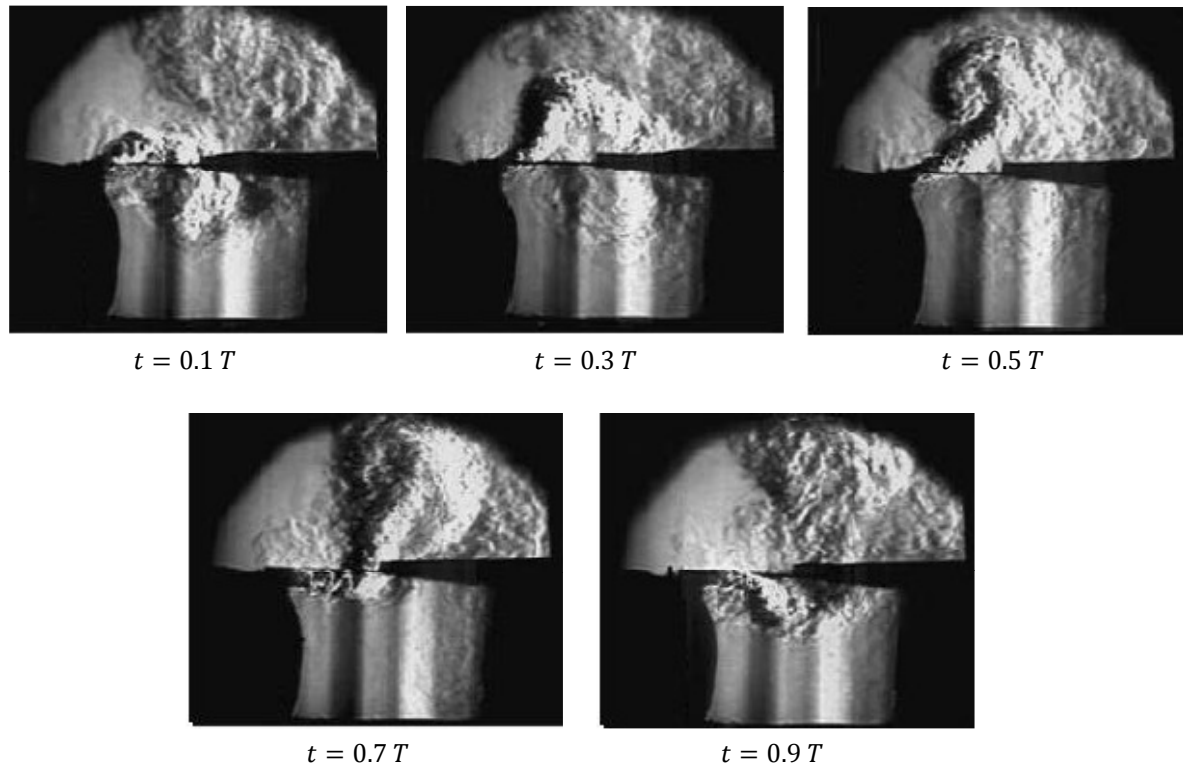
Figure 63: Visualization of one oscillation period of the air jet in an open organ pipe, recorded by Paal et al. [1]

For the labium with an angle of 30°, oscillations were observed for mouth widths between 18 mm and 13 mm. Above 18 mm, no oscillations were observed while for values lower than 13 mm, again oscillations with twice the fundamental frequency were recorded. Figure 65 shows approximately one period of the jet oscillation during normal operation of the organ pipe. Again, it can be seen how the jet deflects, starting from a more or less straight path at $\frac{1}{7}T$ to a maximal outwards deflection $\frac{2}{7}T$ later. In contrast to the previous cases, here, no inward deflection is observed. This however, is not a characteristic related to the labium angle, but is due to the small mouth width that is used; it is the same effect as observed for the images illustrating the overblowing (Figure 61).

All measurements were performed using the same blowing pressure, and using a square wave as control signal for the servo valve. However, Figure 62 and Figure 64 look somewhat different than Figure 60. The latter seems to be much more turbulent than the others. This conclusion may however not be taken; recordings similar to Figure 62 and Figure 64 were also found for a labium with a 10° angle. The explanation lies in the configuration of the Schlieren set-up itself: the characteristics of the obtained image are very sensitive to the settings of the components. Moving the knife edge somewhat more up or down, or increasing or lowering the intensity of the laser just a little bit influences the result significantly. Since the different measurements were not performed on the same day, the settings of the configuration slightly differ, and therefore the global view of the images is somewhat different.
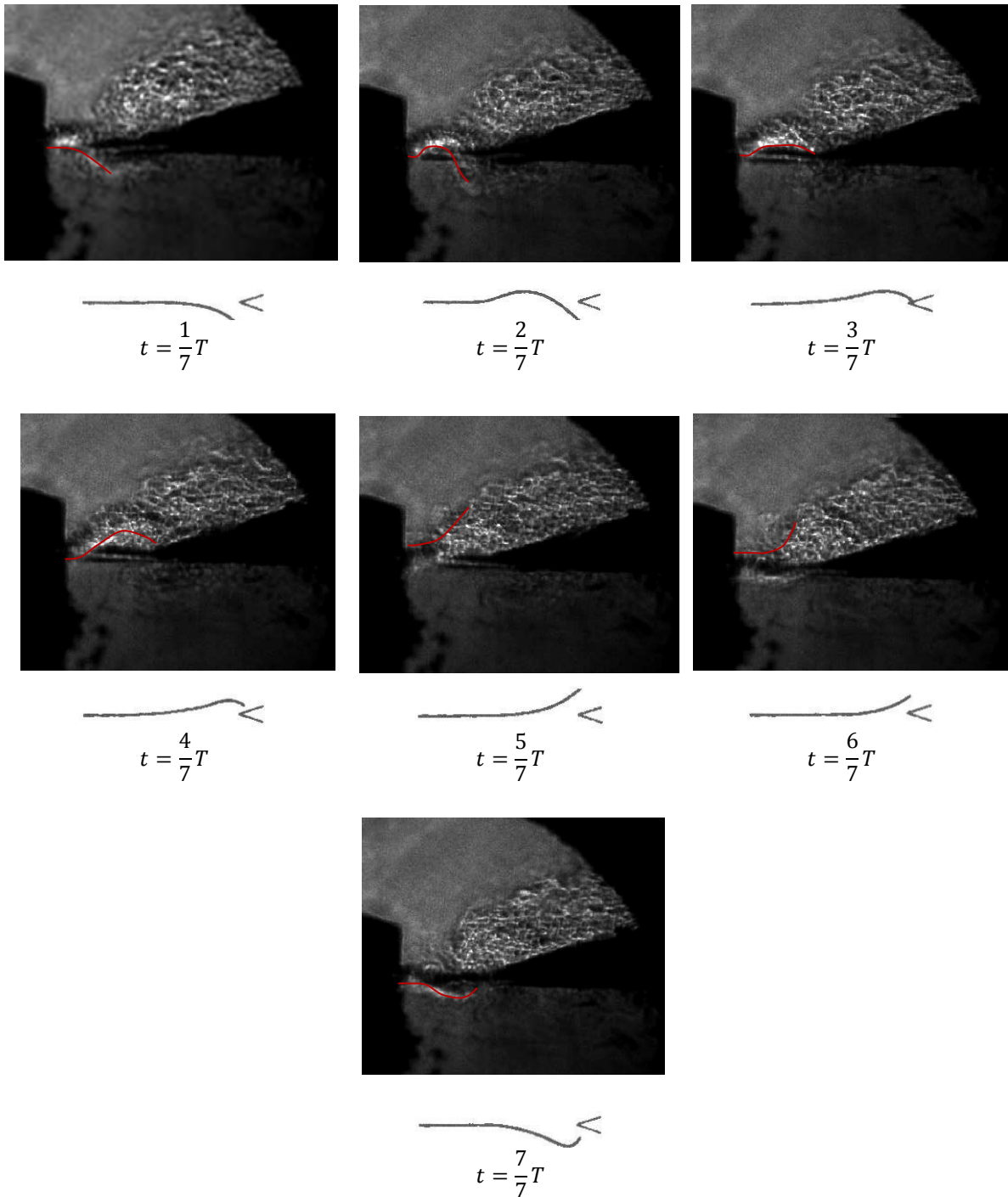
Figure 64: Visualization of one oscillation period of the air jet in an open organ pipe
(h = 1 mm, W = 13 mm, labium angle = 30).

Dequand et al. [21] investigated the behavior of the pulsation amplitude when the mouth configuration was varied. Therefore, a simplified model to predict the amplitudes was proposed. A formula as a function of h, W, the acoustical pressure p at the top of the resonator, the frequency of the acoustical oscillations, the length of the resonator, and the jet flow velocity was derived. The performed experiments show that, first, if the mouth width is kept constant, the amplitude of oscillation increases for increasing labium angle, and second, if the angle is kept constant, the amplitude decreases for increasing values of mouth width. These characteristics were tried to be observed using the Schlieren technique, but no conclusions could be made. As already stated, the Schlieren technique does not aim to provide quantitative data. Conclusions can only be made on qualitative trends. Therefore, the changes in the flow have to be significant in order to be able to detect them in the recorded image by the bare eye. In this case the differences in amplitude caused by adapting the configuration are so small that they could not be observed using this technique.

5.3.1.2.2 Stopped pipe

Besides the fact that the period of oscillation is twice that of the open pipe, no significant differences were observed in the flow pattern for the stopped pipe. In agreement with the discussion in paragraph 5.3.1.1, the mouth widths for which a good tone is produced, were found to be higher than for the open pipe. However in general, it appeared to be more difficult to get a strong tone out of the pipe for the stopped configuration. A visualization of approximately one period is shown in Figure 65. The period starts when the jet is pointed to the labium. It deflects to the exterior of the pipe and reaches a maximum deflection at $t = \frac{4}{7}T$. Then, beam is redirected to the interior of the pipe. The deflection is however much less than that to the outside; the beam stays close to the flue axis.

The other labia gave similar results, and are therefore not reproduced here. Though, the AVI files are added on the included CD.

$$t = \frac{1}{7}T \qquad t = \frac{2}{7}T \qquad t = \frac{3}{7}T$$

$$t = \frac{4}{7}T \qquad t = \frac{5}{7}T \qquad t = \frac{6}{7}T$$

$$t = \frac{7}{7}T$$

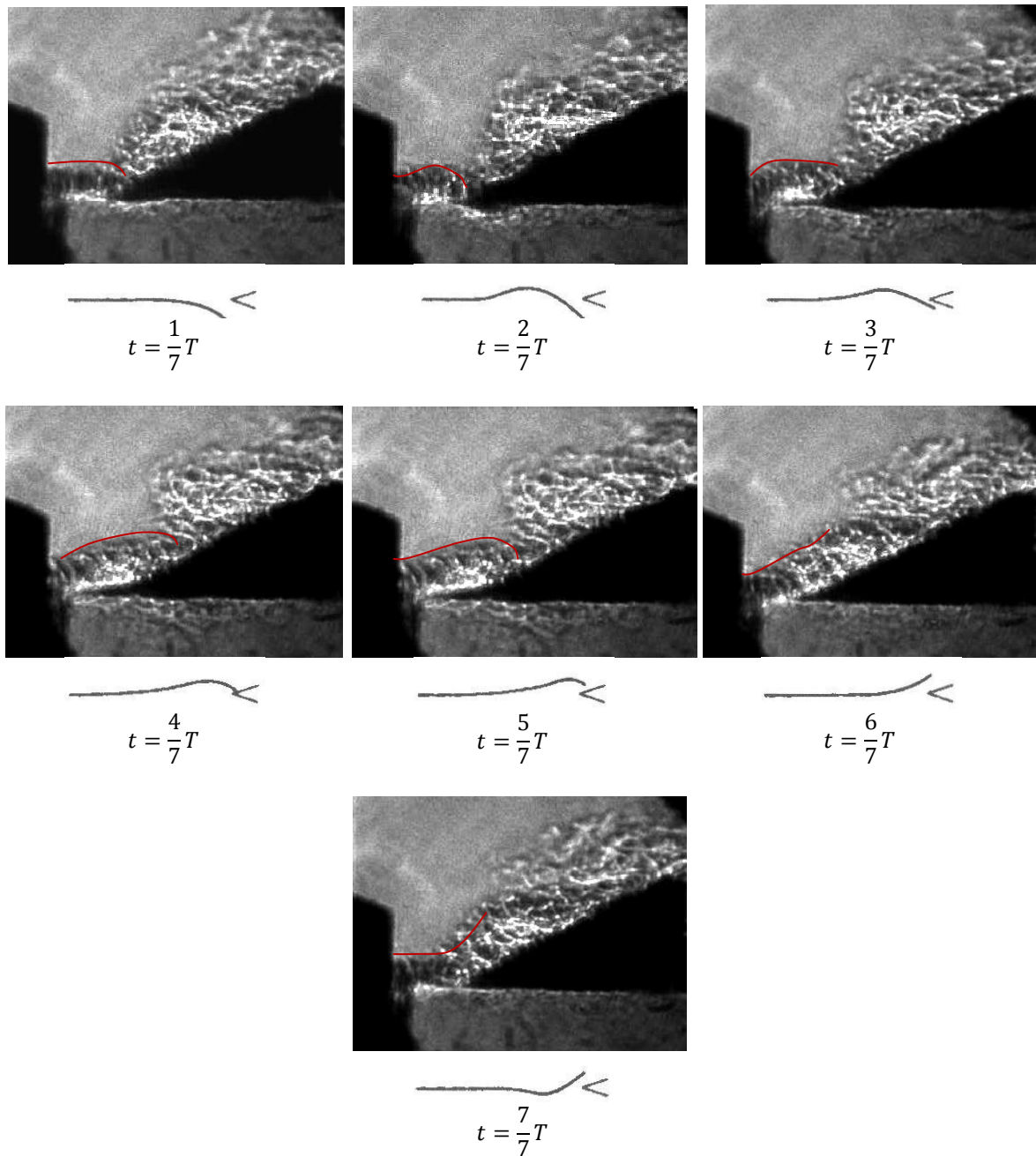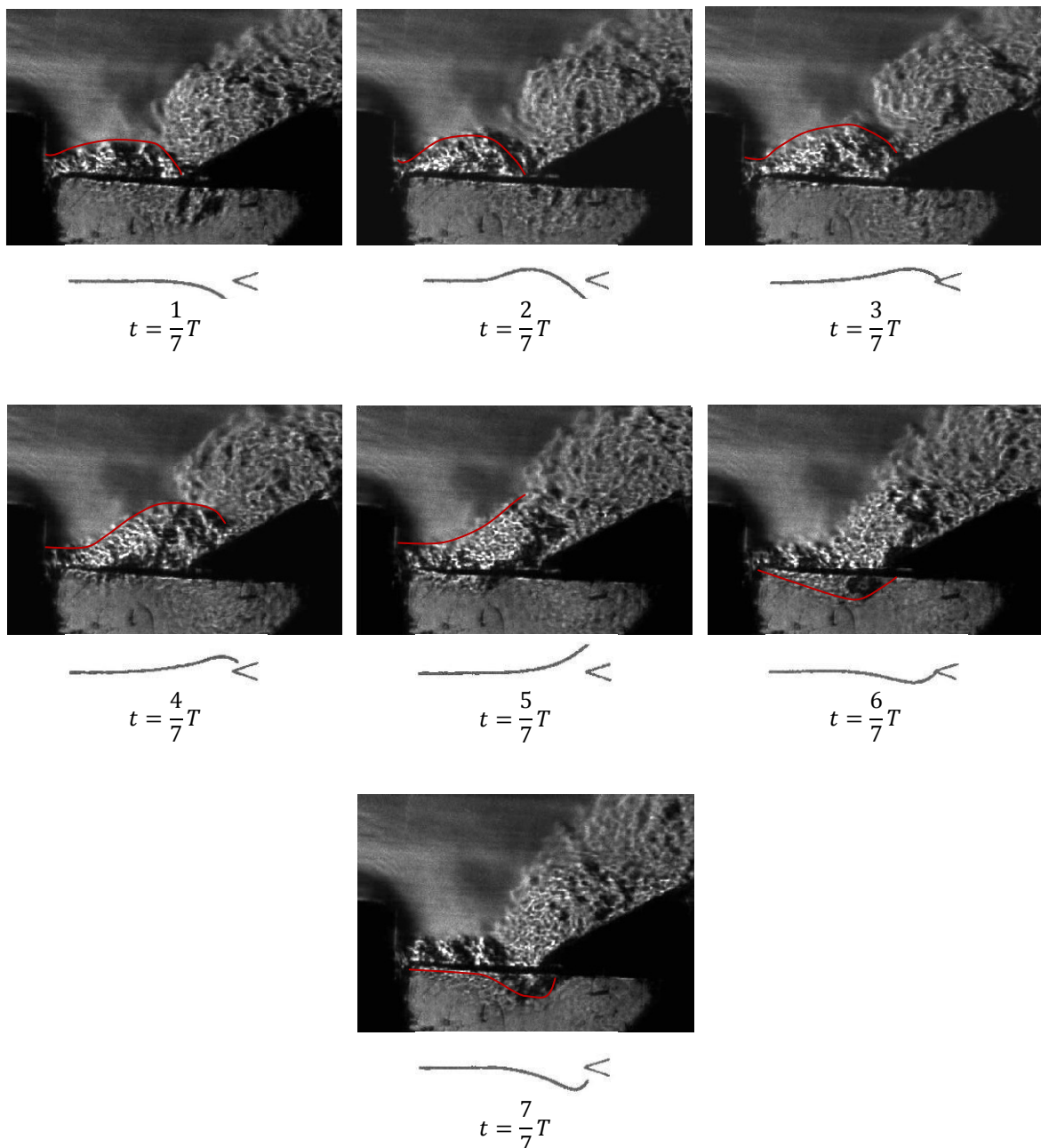**Figure 65:** Visualization of one oscillation period of the air jet in a stopped organ pipe
(h = 1 mm, W = 26 mm, labium angle = 30).

5.3.2   PIV measurements

Particle Image velocitmetry is another optical measurement technique that can be used for the visualization of the flow in an organ pipe mouth. As the name suggests, this technique determines the velocity distribution of a flow field, and can thus be used for the calculation of related fluid properties. The fluid to be investigated is seeded with tracer particles, and it is the displacement Δs of these particles that is measured during a time interval Δt, in order to calculate the velocity.
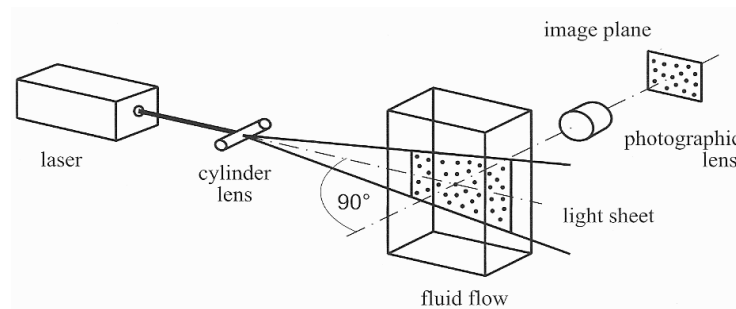
Figure 66: Configuration for the PIV measurement technique. [32]

A laser beam, converted to a sheet by means of a cylinder lens is pointed to the flow field and illuminates the seeding particles. The motion of the particles in the plane of the light sheet is recorded by a camera that is pointed normal to the laser sheet; the classic PIV technique is thus a 2 dimensional field technique. For the determination of the velocity, two or more recordings at a time interval of Δt are necessary. In order to produce the desired pairs of images, the test zone is best illuminated with pulsed light. The pulse length δt and separation time Δt depend on the velocity to be measured. Furthermore, the intensity of the pulse has to be high enough to allow the particles to be recorded. The best option is to choose a laser that can produce double pulses. The camera is then to be synchronized with the laser pulses, so that the two pulses illuminate two successive frames. These recordings can then be subjected to a software, in order to calculate the velocity field. [32]
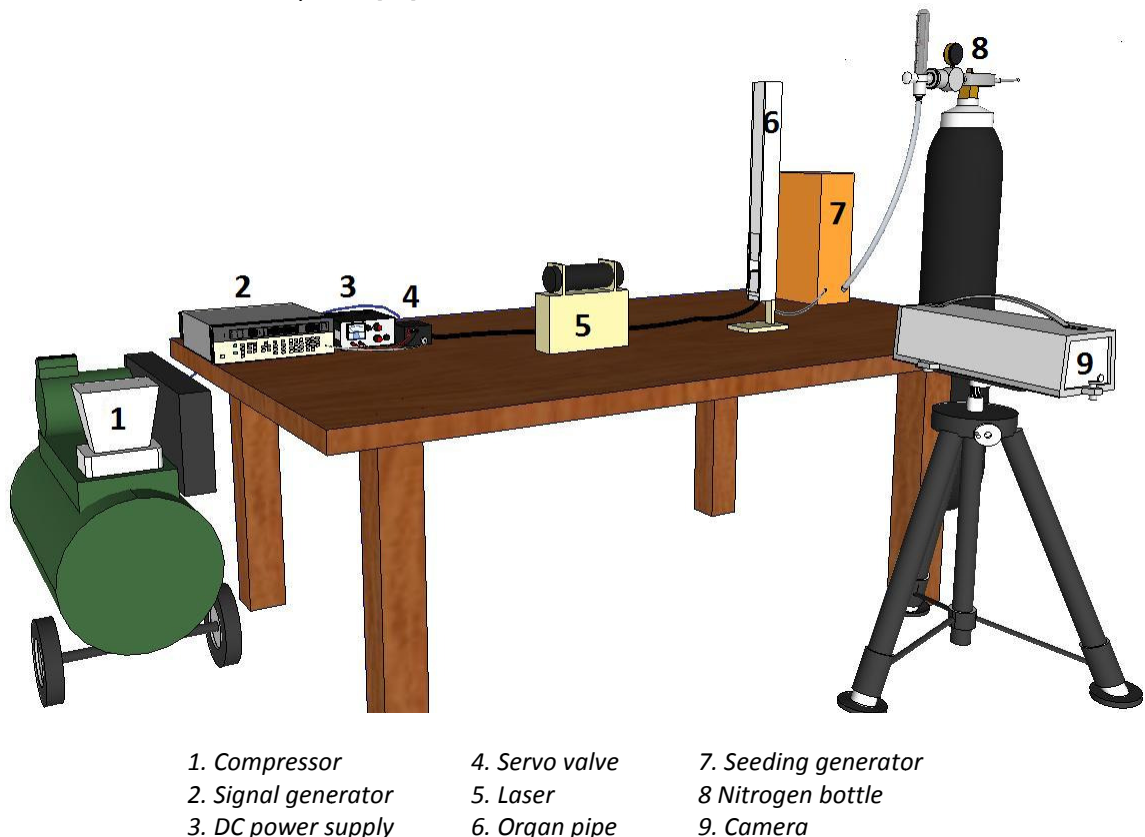
1. Compressor   4. Servo valve   7. Seeding generator
2. Signal generator   5. Laser   8 Nitrogen bottle
3. DC power supply   6. Organ pipe   9. Camera

Figure 67: Schematic representation of the PIV set-up.

Figure 67 shows the schematic representation of the set-up used for the PIV measurements. The same Nd:YLF laser *(5)* as for Schlieren set-up was used for these measurements. A cylindrical lens was mounted on it, in order to produce a sheet of light instead of a circular beam. The particles were generated with a seeding generator *(7)*, driven on nitrogen *(8)*. The organ pipe *(6)*, driven by compressed air *(1)* was placed in the laser beam. The camera *(9)* was placed perpendicular on the direction of the beam. Because the recordings were only intended for visualization, they were not subjected to the software.

As for the Schlieren measurements, the PIV recordings discussed below are added in AVI format on the included CD.

For low jet velocities, i.e. low blowing pressures, in the order of 50 mV, the recorded images show a clear development of vortices (Figure 68). However, for these low pressures, no sound is produced. When the pressure is raised to a level at which sound is generated, these structures could not be recorded any more. Only the initial development of the jet could be clearly visualized. Figure 69 shows how the jet emerges from the flue, and forms a pair of vortices due to friction at the sharp edges of the flue exit. Behind this head vortex, an alternating series of vortices is induced, like drawn in Figure 6 (a). At a time of 1.6 ms, the jet hits the labium. While on that moment the flow is still clearly visible, 0.4 ms later, the turbulence has already washed away the 2 dimensional structures in the top part of the jet. At 2.8 ms after the emerging of the jet, only a cloud of seeding is observed.

$t = 0 \, ms = 0T$ $t = 3.5 \, ms = 1T$ $t = 7 \, ms = 2T$
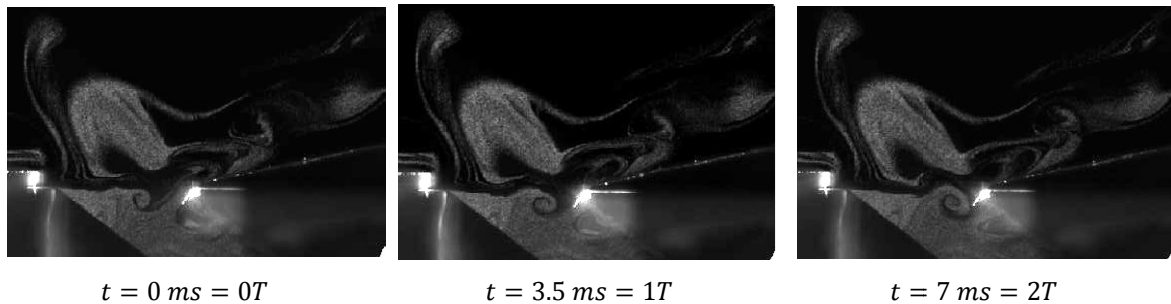
Figure 68: PIV flow visualization of the flow development for low jet velocities.

The reason for that can be found in two factors. First, the seeding supply poses a problem. When a square wave controls the servo valve, the jet leaves the flue with a velocity of about 10 m/s. This relatively high velocity quickly drags away the seeding when the valve is opened. Different positioning of the seeding hose was tested, but no good results could be obtained. For example, the images from Figure 68 are recorded by inserting the seeding directly in the resonator Figure 70 (a). Therefore, the jet emerging from the flue only contains air, and is colored black, while the white colored seeding is blown perpendicular to it and so reveals the vortices. The images of Figure 69 are recorded by applying the seeding to the pipe foot (Figure 70 (b)). Therefore, the jet already contains the seeding and is clearly distinguishable from the black background. For low jet velocities, the supply of the continuously new seeding is fast enough to continuously keep enough seeding in and around the jet for both configurations, but not for higher velocities. A second reason can be found in the three dimensional character of the created vortices. Because a 2D PIV measurement is done, only the particles that remain in the light sheet can be traced. So, a lot of information is lost because of the velocity component in the third dimension. Turbulence is inherently present in a blown organ pipe. Recorders on the other hand, are dimensioned in order to obtain a laminar flow throughout the whole mouth. Recorders, and as a matter of fact, all woodwinds containing no reed, have a mouth geometry similar to the organ pipe. Recorders are however designed with a lower mouth width, and operate by a lower jet velocity. In order to produce the desired sound strength, an organ pipe needs to be driven by higher jet speeds, and therefore turbulence is inevitable. This turbulence will add noise to the sound. Sometimes, this effect is wanted to reach a desired timbre, in other cases, the effects of turbulence are tried to be minimized. [42]

$t = 0\ s$ $t = 0.4\ ms$ $t = 0.8\ ms$

$t = 1.2\ ms$ $t = 1.6\ ms$ $t = 2.0\ ms$

$t = 2.4\ ms$ $t = 2.8\ ms$ $t = 3.2\ ms$
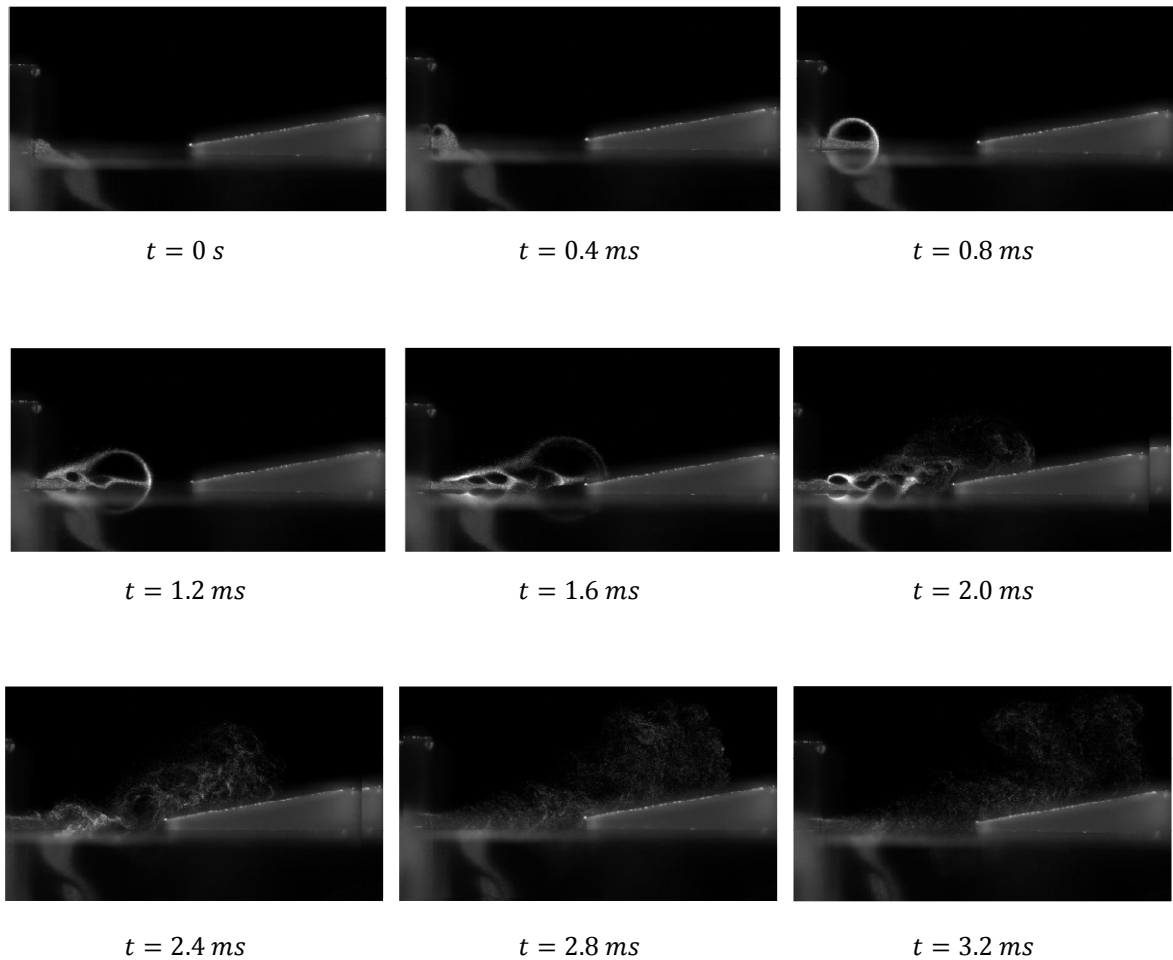
Figure 69: Flow visualization of the first milliseconds of the flow using the PIV technique.

(a)   (b)

Figure 70: Two different ways to insert the seeding.

5.3.3   LDV measurements

Parallel with the Schlieren and PIV measurements, the flow behavior was also observed by using the Laser Doppler Vibrometry technique. In paragraph 5.2.3, this technique was used to obtain measurements in the frequency domain, but it is also possible to do measurements in time. Recalling equation 5.4, it is clear that the LDV measures differences in pressure, which can be afterward post processed to obtain the frequency information. Now however, the measured pressure distribution was imaged as a contourplot, whereof qualitative information could be extracted, precisely like for the Schlieren images. Since the LDV

technique has as main purpose the determination of the velocities of the testobject, the corresponding legend of the contourplot has units of micrometer per seconds (Figure 71). Equation 5.3 shows that an increment in optical path length corresponds to an increase in index of refraction. Combining equation 3.2 with the ideal gas law learns that a positive variation in refractive index is caused by an increase in pressure. Thus, a higher pressure corresponds to an increase in optical path length, which is the same result as a positive velocity. Therefore, by considering a positive velocity as a compression, and a negative velocity as a rarefaction, the obtained images can be interpreted in terms of pressure.
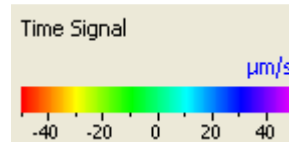
Figure 71: Legend corresponding to the LDV measurements.

As explained in paragraph 5.2.3, the laser scans points in a preliminary defined area. Two sets of measurements were performed: for a first series of measurements, the test area was restricted to the mouth of the pipe, while the other measurements the whole resonator was observed. In what follows, the results of a measurement of the flow in an open pipe, induced by a square wave driven valve opening are discussed. The mouth geometry was chosen to be the same as that of Figure 60: a labium angle of 10 °, flue height of 1 mm and a mouth width of 16 mm. Figure 73 shows the first milliseconds of the flow in the mouth of the pipe. The same visualization area is chosen as for the Schlieren images. Here however, the boundary of the flue exit is not shown on the figure, and the boundary of the labium is cut out. This is done because the Plexiglas would otherwise disrupt the measurements. Because perpendicular incidence of the laser beam on the organ pipe is only possible for one single measure point, for all other points, there will be a geometric shift between the intersection with the front and back side of the pipe. Therefore, the boundary of the selected test area cannot be taken too narrow in order not to have interference with the back of the pipe. For clearance, the imaged part is identified on Figure 72.
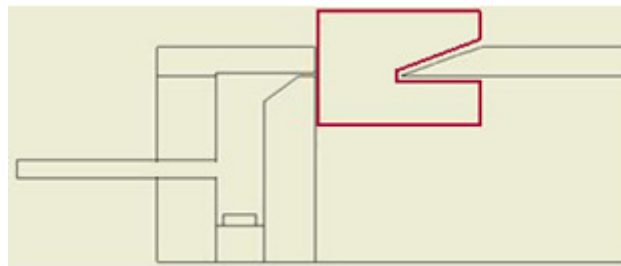
Figure 72: Illustration of the part visualized on the following images.

At 15.58 ms after opening the valve, a compression is noticed at the flue exit, corresponding to the emanating jet. Because the time between the opening of the valve and the release of the jet in the pipe mouth is dependent on the length of the connection between these two components, and to stay consistent with the time labeling of the Schlieren images, this event is labeled to be the start of the time scale. To be more precise, the recorded image just before the one which shows the emerging of the jet, is set to t = 0. Because the images are recorded with a frame rate of 20 000 f/s, all recorded time data is thus subtracted by 15.53 ms, so that all images are related in time to the moment at which the jet is first detected in the mouth. The detected compression slowly travels to the labium, and touches it at about 0.75 ms after the first compression in the mouth was noticed. The development of the resulting vortex shedding is shown in Figure 74. On the first two images, the alternating zones of compression and rarefaction point on the vortices formed on the emerging jet itself. As soon as the jet touches the labium, the latter will play a part in the creation of the pressure zones. At t = 0.93 ms, the region outside the pipe is entirely dominated by a rarefaction, while the entire zone inside the pipe is at higher pressure. This two-part division however does not stand long; 0.10 ms later, a large part of the test zone is again subjected to the atmospheric pressure, and only spots of rarefaction and compression, corresponding to the development of the jet are observed.

$t = 0.2\ ms$

$t = 0.3\ ms$

$t = 0.4\ ms$

$t = 0.5\ ms$

$t = 0.6\ ms$

$t = 0.7\ ms$
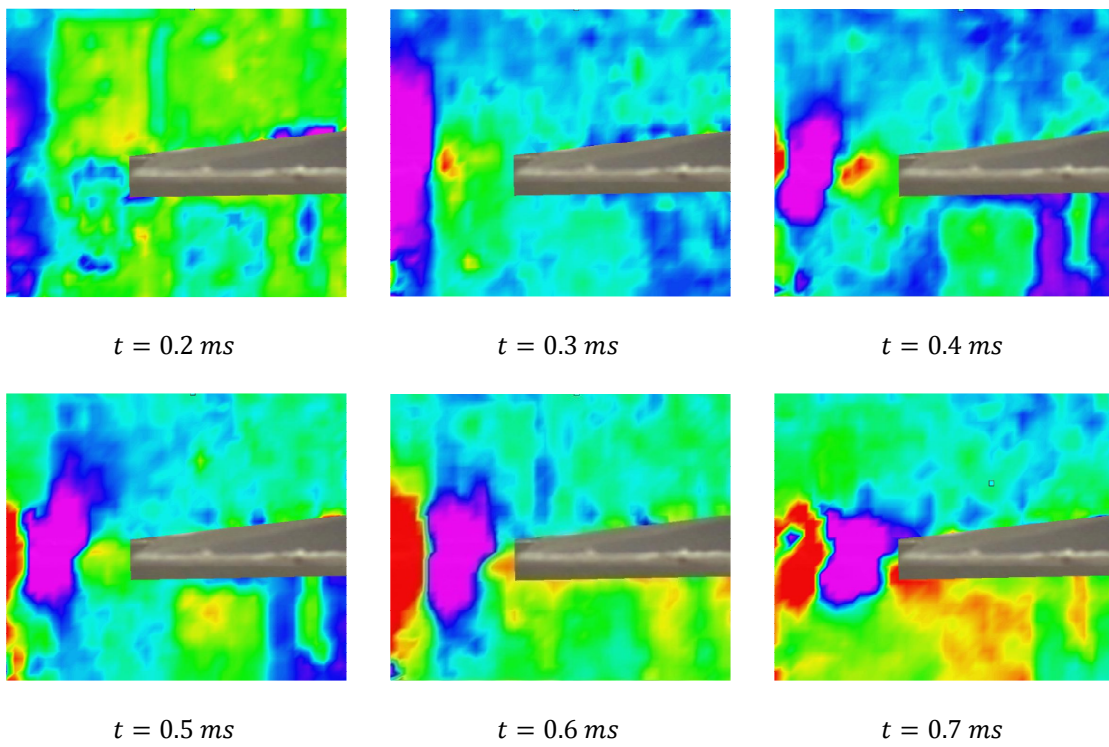
Figure 73: Visualization of the first milliseconds of flow using the LDV technique.

$t = 0.73\ ms$

$t = 0.78 ms$

$t = 0.83\ ms$

$t = 0.88\ ms$

$t = 0.93 ms$

$t = 0.98\ ms$

$$t = 1.03 \; ms \qquad\qquad t = 1.08 \; ms \qquad\qquad t = 1.13 \; ms$$
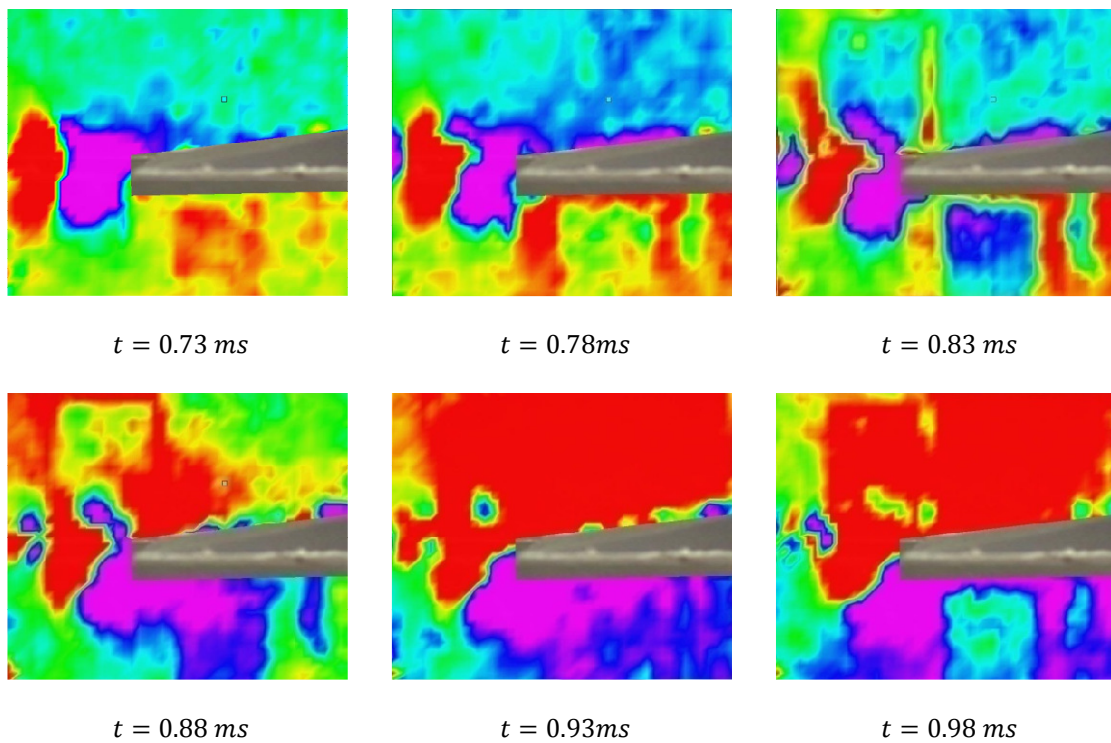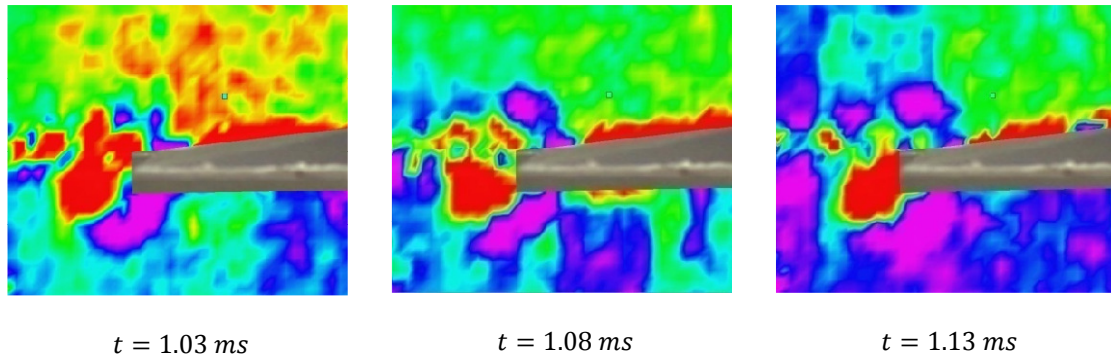
Figure 74: Vortex shedding development after contact with the labium.

$$t = \frac{1}{9}T \qquad\qquad t = \frac{2}{9}T \qquad\qquad t = \frac{3}{9}T$$

$$t = \frac{4}{9}T \qquad\qquad t = \frac{5}{9}T \qquad\qquad t = \frac{6}{9}T$$

$$t = \frac{7}{9}T \qquad\qquad t = \frac{8}{9}T \qquad\qquad t = \frac{9}{9}T$$

Figure 75: Visualization of one period of the flow at the mouth of the pipe in steady state.

At about 4.5 ms after the emerging of the jet, large areas with the same pressure appear. However, the images are not totally uniform; many spots with other pressure exist, next to larger areas with the predominating pressure. Images with large areas of compression alternate with images with areas of rarefaction. Every cycle, the homogeneity in pressure increases, and at t = 13.5 ms, images with totally uniform pressure are observed. The period of this pressure cycle has a mean value of 1.2 ms. Around t = 20.5 ms, this phenomenon decreases: again images containing a lot of spots with zero pressure are observed. At this moment, the period of the pressure waves changes from 1.2 to 2.2. The observed behavior is thus a transition phenomenon. A full compression is again observed at t = 25 ms, while the period corresponding to the rarefaction is still characterized by a major amount of neutral pressures. A full rarefaction is only again detected from a time of t = 33 ms. From that moment, again strong alternations of compression and rarefaction are detected. At 74 ms after the emerging of the jet, the frequency again changes. It switches to a mean period of 3.2 ms, which corresponds to the fundamental frequency of the pipe. The quasi steady state is thus started from that moment. In contrast to the first frequency change, no strong influence on the pressure zones is observed. One period of the pressure oscillations is shown in Figure 75.

To investigate what happens in the meantime in the resonator, also LDV measurements for that part of the pipe were performed. Because now a larger area was to be recorded, the camera had to be shifted backwards. This implies that the effect of the displacement of the interse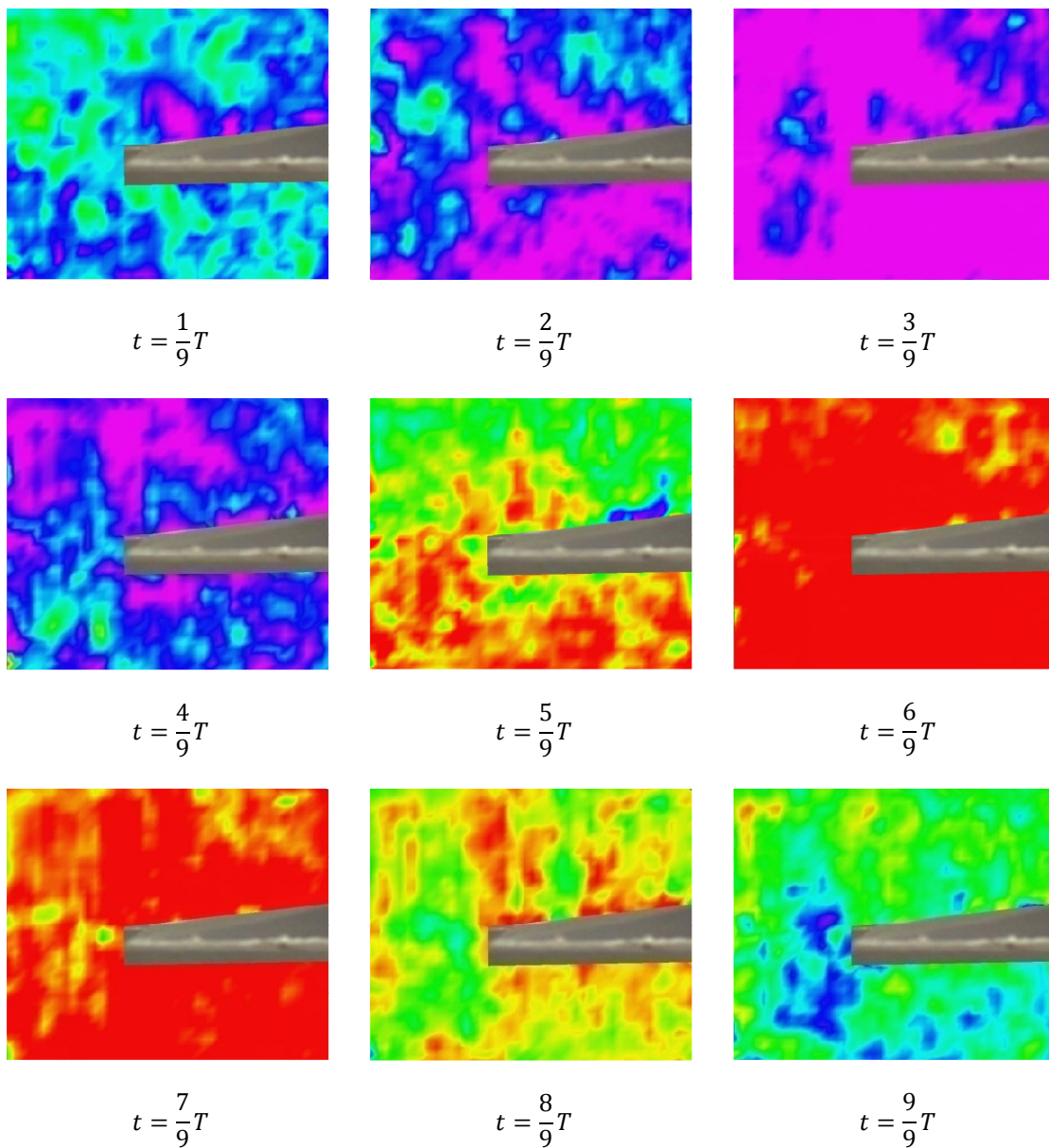ction points with the front and backside is larger, and therefore a larger distance of the testzone to the plexi boundaries had to be ensured. Therefore, the left boundaries of the images below do not correspond to that of the zooms above, but more or less to the middle of the distance between the flue exit and labium tip (Figure 76). This has to be taken into account when comparing the following pictures to those above.
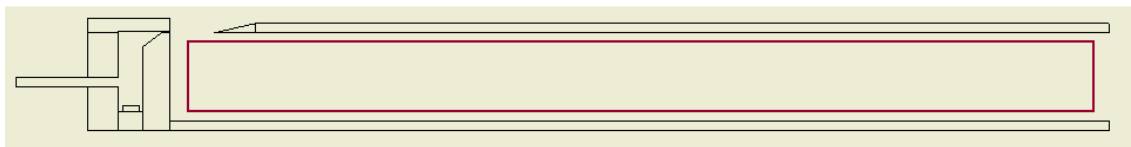
Figure 76: Illustration of the part visualized on the following images.

The first milliseconds of the flow in the resonator are shown in Figure 77. The first compression in the resonator is detected 16.02 ms after the opening of the valve. This indeed correspond to what was found above, taking into account the boundary shift. The alternating rarefactions and compressions introduced in the mouth of the pipe are transmitted to the resonator.

$t = 0.49\ ms$

$t = 0.93 ms$

$t = 1.41\ ms$
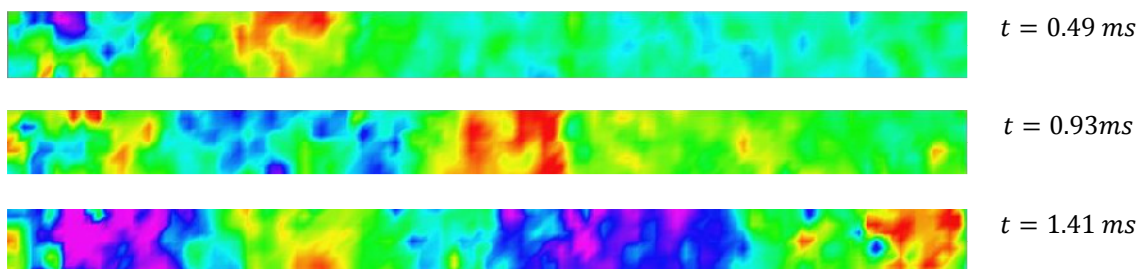
Figure 77: Visualization of the first milliseconds of the flow in the resonator.

At about t = 10 ms, a quasi uniform pressure is observed in the pipe. The alternations of compression and rarefaction happen with a period of approximately 1.2 ms, which was expected from the frequency observed in the mouth of the pipe. While for the compression already an almost uniform pressure is observed, the period corresponding to the rarefaction still contains large zones with zero pressure. Every period, the pressure wave seems to get stronger, and at t = 15 ms, a pipe with uniform pressure is observed. The transition to a higher frequency starts a little bit later than in the mouth of the pipe; at t = 22 ms, the pressure in the pipe starts again to be more divided; large areas with zero pressure are present. This transition zone last till a time of t = 27 ms. Then again stronger standing waves are visible, however not as strong as before; many spots with zero velocity are present. The last transition is situated

at t = 69 ms, then the frequency changes to the fundamental value. As for the observations of the mouth, no strong transition zone is observed during this period. One period of the flow during the quasi static behavior is shown in Figure 78. The alternation of the compression and rarefaction is clearly shown. However, during the compression time, zones with rarefactions are observed. This can be attributed to the influence of the higher harmonics. This phenomenon is characteristic for the quasi steady state, as it was not observed during the period before t = 69 ms.

$$t = \frac{1}{12}T$$

$$t = \frac{2}{12}T$$

$$t = \frac{3}{12}T$$

$$t = \frac{4}{12}T$$

$$t = \frac{5}{12}T$$

$$t = \frac{6}{12}T$$

$$t = \frac{7}{12}T$$

$$t = \frac{8}{12}T$$

$$t = \frac{9}{12}T$$

$$t = \frac{10}{12}T$$

$$t = \frac{10}{12}T$$

$$t = \frac{12}{12}T$$
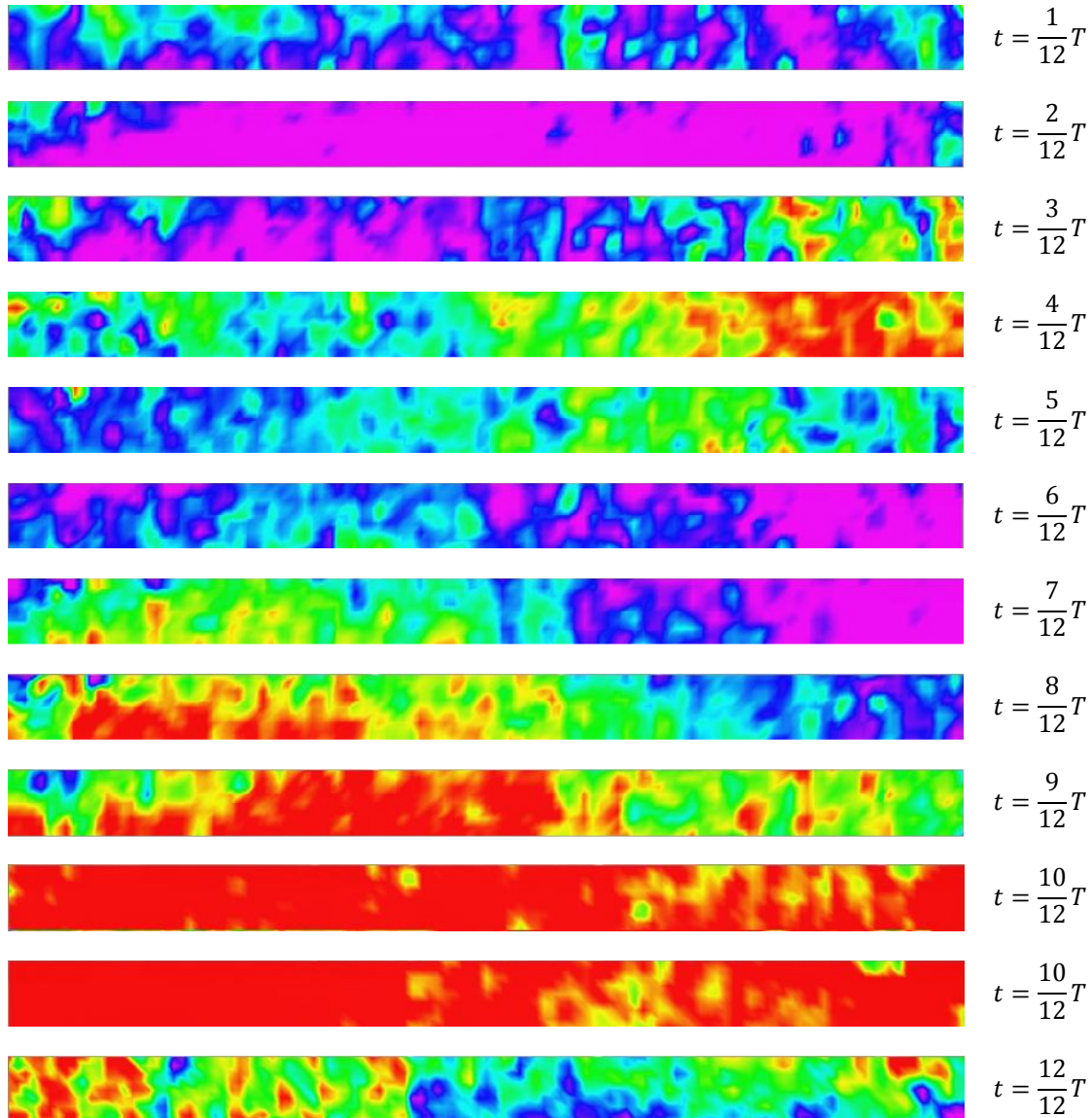
Figure 78: Visualization of one period of the flow in the resonator.

5.3.4   Conclusions

The airflow in the mouth of an organ pipe was visualized using three different techniques, each based on the measurement of a different quantity. The Schlieren technique reveals the flow by converting the phase differences, induced in the light wave during the passing of the density inhomogeneities introduced by the CO_2, to a difference in illuminance on the screen. Since the Schieren technique is sensible for variations in refractive index, it is the derivative of the density that is imaged. The PIV technique, on the other hand, tracks the displacement of seeding particles that follow the movement of the flow, while LDV is based on the measurement of pressure differences. Therefore, the different techniques will highlight different aspects of the flow in the organ pipe. Schlieren measurements have shown to be ideally suited

for the visualization of the flow in the pipe mouth for both the transient and the quasi steady state. The evolution of the jet can be clearly observed, however this is restricted to the global movement. The overall view of the obtained images is dominated by turbulence, which makes it impossible to detect small structures. The PIV measurements on the contrary, shows a beautiful development of the jet, whereby an alternating series of vortices can be detected behind the head vortex. This technique, however, fails to deliver interesting images for later periods of the flow development, and is therefore less interesting for this application. The LDV technique is the only studied technique that allows flow visualization in the resonator. This is very interesting, since the flow development in the pipe mouth can in that way be linked to the behavior in the resonator. The color scaled image allows the different pressure zones to be clearly distinguished. However, the interpretation of the obtained images is not so straightforward as for the results of the other two techniques, where the flow related to the organ pipe could be clearly distinguished from the surrounding air.

6   Conclusions

The mystery behind the generation of sound in organ pipes has intrigued people for at least 200 years. Until now, only a part of the underlying physical aspects has been revealed, and therefore, the pursuit of a better understanding continues. The problem is studied by different approaches, using a variety of measurement techniques.

In this thesis, the sound spectrum emitted by a representative organ pipe was studied, and the influence of the blowing pressure and mouth geometry was analyzed. Both the flue height and mouth width of the pipe were made variable, while above that, labia with three different angles were tested. It has been shown that all these parameters have a significant influence on the frequency and amplitudes of the generated harmonics. Increasing the blowing pressure, results in an increase in both the frequency and amplitude of the harmonics. Progressively more harmonics are locked in, but when the pressure is made to high, the pipe is overblown, and the second harmonic takes over from the fundamental tone. Lowering the mouth width and flue height results in the same conclusions. Most of the observed trends could be explained by theoretical considerations, though some characteristics, in particular the influence of the labium angle, remain unclear.

For the visualization of the flow in the pipe mouth, the Schlieren technique has been proven useful. Despite the expensive parabolic mirrors, a good Schlieren configuration can be set up for a reasonable budget. This in contrast to the PIV technique, which requires the use of an expensive double pulsed laser. Aligning the optics of a Schlieren configuration requires some skills, but once acquainted with the technique, clear visualizations can be obtained in a short time. The Schlieren technique is ideally suited for the visualization of both the transient and steady state of the sound production. The jet development and the flow oscillations can be clearly observed, however, no quantitative data can be distracted from the measurements. The major drawback of this technique is that only the global characteristics of the jet movement can be observed; only the oscillation dominated by the fundamental frequency can be distinguished, while the higher frequencies, which are determinative for the sound quality, remain hidden.

The Particle Image Velocimetry technique gives rise to a complete different kind of images. Because of its two-dimensional character, clear flow visualizations can only be obtained for the early stage of the jet development. As soon as the jet becomes turbulent, a lot of information is lost because of the velocity component in the third dimension.

The Laser Doppler Vibrometry technique can be employed in an unconventional way to visualize the flow behavior in the organ pipe. While this technique is mostly used for the determination of vibration amplitudes and frequencies of surfaces, it can also be employed for the visualization of acoustic waves in fluids, as proposed by Zipser and Franke. The obtained image is a color scaled representation, indicating zones of rarefaction and compression. A positive aspect of this technique is that, in addition to the flow in the pipe mouth, also the pressure fluctuations in the resonator itself can be visualized. This allows the behavior of the jet to be related to that of the flow in the resonator. Because of the color scale, the transient behavior can be studied in more detail. It has been observed that in the early state of the attack transient, the oscillations are carried out with a higher frequency. During two transition zones, this frequency is suddenly lowered to finally settle for the fundamental frequency. Outside these zones, strong alternations of compression and rarefaction are observed, while the transition zones are characterized by large spots of atmospheric pressure, next to the dominating compression or rarefaction. This behavior was observed for both the pipe mouth and the resonator.

It is clear that optical techniques are perfectly suited for the study of the flow in organ pipes. Because of their non-intrusive character, the obtained measurements reflect the real flow and can therefore be directly interpreted. The optical techniques used in this thesis allow a two dimensional, or integrated two dimensional measurement, which results in a clearly recognizable image and therefore facilitates the interpretation of the results. Because every technique is based on the measurement of a different physical quantity, each technique highlights other aspects of the organ pipe behavior. And therefore, the secrets of the sound production in organ pipes can only be revealed by using a wide range of measurement techniques.

References

[1]   Paál G., Angster J., Garen W., Miklós A. (2006), A combined LDA and flow-visualization study on flue organ pipes, *Experiments in Fluids,* 40:825-835.

[2]   Angster J., Wik T., Taesch C. Miklós A. (2005), Experiments on the influence of pipe scaling parameters on the sound of flue organ pipes, *Forum Acousticum 2005*, Budapest, 603-609.

[3]   Helmholtz, H. von (1954), *On the Sensation of Tone*, New York, Dover publications.

[4]   Lord Rayleigh (1945), *The Theory of Sound*, New York, Dover publications.

[5]   Brown G. B. (1937), The vortex motion causing edge-tones*, Proc. Phys. Soc. Lond,.* 49: 493-507.

[6]   Brown G. B. (1937), The mechanism of edge-tone production*, Proc. Phys. Soc. Lond,.* 49: 508-521.

[7]   Powell A. (1961), On the edgetone, *J. Acoust. Soc. Am*., 33: 395-409.

[8]   Powell A. (1961), Vortex action in edgetones, *J. Acoust. Soc. Am*., 34: 163-166.

[9]   Cremer L. (1965), Berechnung der selbsterregten Schwingungen von Orgelpfeifen, 5th *International Congress on Acoustics,* Liège, paper L65.

[10]   Ising H. (1965), Uber die Tonbildung in Orgelpfeifen, 5th *International Congress on Acoustics,* Liège, paper M55.

[11]   Bechert D. (1965), Schwingungen eines akustisch gesteurten ebenen Freistrahls, 5th *International Congress on Acoustics,* Liège, paper L35.

[12]   Coltman J. M. (1968), Sounding mechanism of the flute and organ pipe, *J. Acoust. Soc. Am.,* 44: 983-992.

[13]   Elder S. A. (1972), On the mechanism of sound production in organ pipes, *J. Acoust. Soc. Am*., 54 (6): 1554-1564.

[14]   Fletcher N. H. (1976), Jet-drive mechanism in organ pipes, *J. Acoust. Soc. Am.,* 60 (2): 481-491.

[15]   Fabre B. (1992), *La production de Son dans les Instruments à Embouchure de Flûte : Modèle Aéro-Acousitque pour la Simulation Temporelle*, PhD thesis, Université du Maine, Le Mans, France.

[16]   Verge M.-P. (1995), *Aeroacoustics of confined jets with applications to the physical modeling of recorder-like instruments,* PhD thesis, Technische Universiteit Eindhoven, Eindhoven, the Netherlands.

[17]   Dequand S. (2001), *Duct Aeroacoustics: from Technological Applications to the Flute*, PhD thesis, Technische Universiteit Eindhoven, Eindhoven, the Netherlands.

[18]   Verge M., Fabre B., Mahu W., Hierschberg A., van Hassel R., Wijnands A., de Vries J. And Hogendoom C. (1994), Jet formation and jet velocity fluctuations in a flue organ pipe, *J. Acoust. Soc. Am,.* 95: 1119-1132.

[19]   Fletcher N. H. (1976), Transients in the speech of organ flue pipes – a theoretical study, *Acustica*, 34: 24-233.

[20]   Angster J., Miklós A. (1992), Transient sound spectra of a variable length organ pipe, *International Symposium on Musical Acoustics*, Tokyo, Japan, 159-162.

[21]   Dequand S., Willems J.F.H., Leroux M., Vullings R., van Weert M., Thieulot C. and Hirschberg A. (2003), Simplified models of flue instruments: Influence of mouth geometry on the sound source, *J. Acoust. Soc. Am,.* 113: 1724-1735.

[22]   Johansson E.-L., Benckert L. and Gren P. (2003), Particle image velocimetry measurements of velocity fields at an organ pipe labium, *Proceedings of the Stockholm Music Acoustics Conference*, Stockholm Sweden, 1: 321-324.

[23]   Hall D. E. (2002), *Musical Acoustics*, Third edition, USA, Brooks/Cole.

[24]   Thistlethwaite N. and Webber G. (1998), *The Cambridge companion to the organ*, Cambridge, Cambridge University Press.

[25]   Vanlanduit S. and Van Overmeire M., *Akoestiek en geluidshinder,* Course notes, Vrije Universiteit Brussel.

[26]   Everest F. A. and Pohlmann K. C. (2009), *Master Handbook of Acoustics*, Fifth edition, USA, Mc Graw Hill.

[27]   The Open University, *Reflection at the end of an air column*, consulted March 2011.http://openlearn.open.ac.uk/mod/oucontent/view.php?id=397877&section=1.5.7.

[28]   Fishbane P., Gasiorowicz S. and Thornton S. (2005) *Physics for Scientists and Engineers*, Third edition, USA, Pearson Prentice Hall.

[29]   Carl R., *Oscillations at a Free Edge*, consulted April 2011, http://hyperphysics.phy-astr.gsu.edu/hbase/music/edge3.html#c2.

[30]   Colin Pykett (2009), *How the flue pipe speaks,* consulted May 2011, http://www.pykett.org.uk/how_the_flue_pipe_speaks.htm.

[31]   Fletcher N. H., Mode locking in nonlinearly excited inharmonic musical oscillators, *J. Acoust. Soc. Am.* 64 (6), 1566-1978.

[32]   Mayinger Franz and Feldmann Oliver (2001), *Optical measurements, techniques and applications*, Germany, Springer.

[33]   Holder D.W. and North R.J. (1963), *Notes on Applied Science No 31; Schlieren Methodes,* England, National Physical Laboratory.

[34]   Settles G.S. (2001), *Schlieren and Shadowgraph Techniques*, Germany, Springer-Verlag.

[35]   Wikipedia, *Laser Dopler Vibrometer*, consulted March 2011. http://en.wikipedia.org/wiki/Laser_Doppler_vibrometer.

[36]   Zipser L., Franke H.,(2007), Refracto-Vibrometry: a convenient method for visualizing ultrasound, *19th International congress on acoustics*.

[37]   Iverson P. and Krumhansl C. (1993), Isolating the dynamic attributes of musical timbre, *J. Acoust. Soc. Am.* 94, 2595-2603.

[38]   Saldana E. L. and Corso J. F. (1964), Timbre cues and the identification of musical instruments, *J. Acoust. Soc. Am.* 36, 2021-2026.

[39]   Mahu W., Peters M., Verge M., Wijnands A., Fabre B. and Hirschberg A. (1993), Attack transient of a flue organ pipe, *Topics in applied mechanics,* 163-171.

[40]   De Greef J. P. (2010), *Houten orgelpijpen, theorie en praktijk,* eigen uitgave.

[41]   Abromovich G.N. and Schindel L. (1963), *The theory of turbulent jets*, The MIT press.

[42]   Information gained by a personal conversation with Prof. dr. ir. Hirschberg

[43]   Menn Naftaly (2004), *Practical Optics*, USA, Elsevier Academic Press.

[44]   Hecht Eugene and Zajac Alfred (1974), *Optics*, USA, Addison-Wesley publishing company.

[45]   Möller K. D. (1988), *Optics*, USA, University Science Books.

[46]   Wikipedia, *Curved mirrors,* consulted April 2011, http://en.wikipedia.org/wiki/Curved_mirror.

Images on the chapter front-pages:

Chapter 1   Elgar E. (1899), *Salut d'Amour,* transcribed for organ by C. J. Grey, first two measures.

Chapter 2   Image drawn by Dom Bédos de Celles (1766), published in the book *L'art du facteur d'orgue*.

Chapter 3   Schlieren image captured by Gary Settles

Chapter 6   Elgar E. (1899), *Salut d'Amour,* transcribed for organ by C. J. Grey, four last measures.

Appendix A: Geometrical Optics

In physical optics, the functioning of an optical element or system is described using waves. On the other hand, optical phenomena can also be described in terms of rays. This method is called the geometrical optics approach. [43]

A.1   Lenses

A.1.1   Refraction at a spherical interface

Spherical waves, produced by a point source S are bent when they cross a boundary between two media. If the wave in the second medium has to be converged in to a point P, the interface has to be well shaped. The requirement for convergence is fulfilled if each ray must travel the same optical path length. Referring to Figure 79 , with $n_2 > n_1$, this can be written as:

$$l_0 n_1 + l_i n_2 = s_0 n_1 + s_i n_1 \tag{A.1}$$
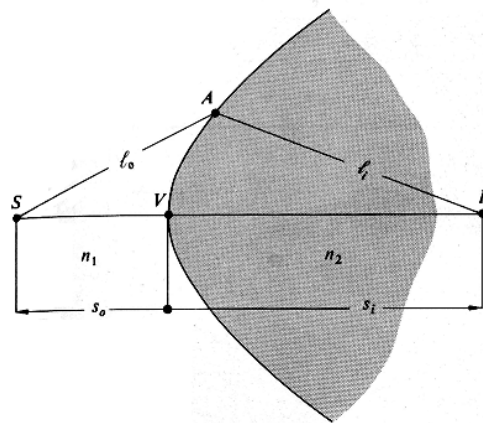

Figure 79: Refraction at a Cartesian oval-shaped interface. [44]

If s_0 and s_i are chosen, the right-hand side is fixed and the equation becomes that of a Cartesian oval. S and P are called conjugated points; a point source at either location will be perfectly imaged at the other.

In addition, some other shaped interfaces can be used (Figure 80). An incident plane wave can be converted to a spherical wave by an ellipsoidal or hyperbolical interface and vice versa. In both cases, the incident rays converge toward or diverge from the farthest focus of the ellipse or hyperbola.
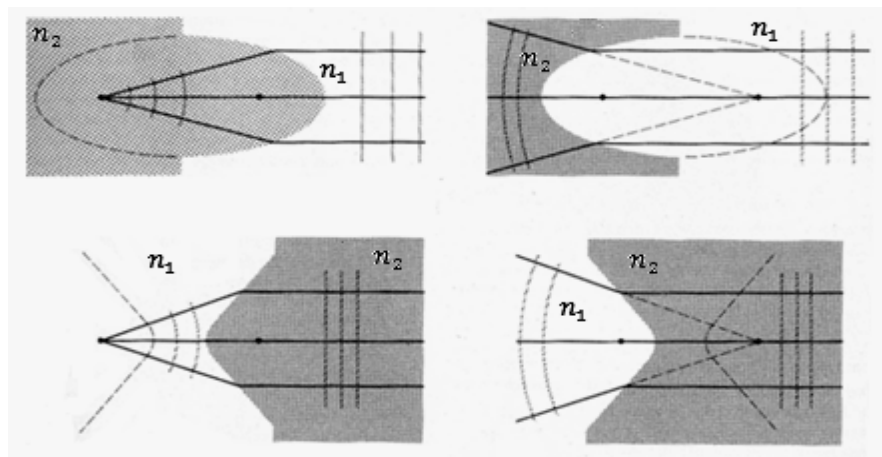

Figure 80: Refraction at ellipsoidal and hyperbolical interfaces. [44]

Because spherical surfaces are easier to fabricate comparing to hyperbolic or spherical ones, this kind of lenses are encountered the most. [44] Consider a wave, emerging from the point source S (Figure 81). Because of the spherical interface that separates the denser medium with refractive index n_2 from the first, the rays are deflected towards the optical axis. Applying the sine-theorem gives:
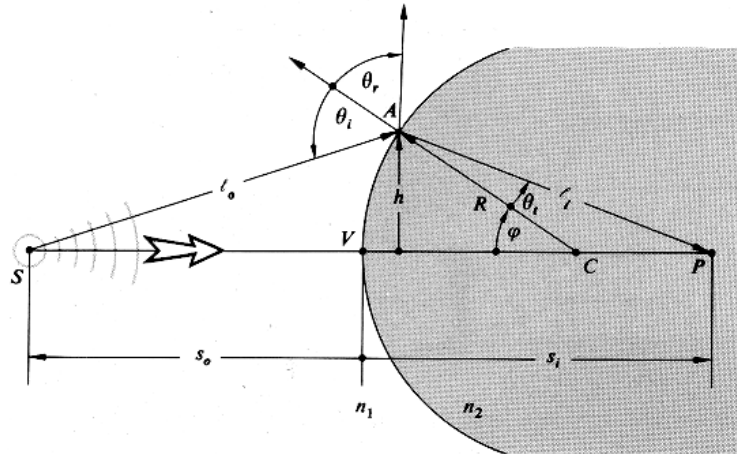

Figure 81: Refraction at a spherical interface. [44]

$$\begin{cases} \dfrac{s_0 + R}{\sin(\pi - \theta_i)} = \dfrac{l_0}{\sin \varphi} & \text{(A.2)} \\[4mm] \dfrac{s_i - R}{\sin \theta_t} = \dfrac{l_i}{\sin(\pi - \varphi)} & \text{(A.3)} \end{cases}$$

Arranging the terms and implementing Snell's law:

$$\sin \theta_i = \frac{n_2}{n_1} \sin \theta_t \tag{A.4}$$

yields:

$$\begin{cases} \dfrac{s_0 + R}{l_0} = \dfrac{\sin \theta_i}{\sin \varphi} & \text{(A.5)} \\[4mm] \dfrac{s_i - R}{l_i} = \dfrac{n_1}{n_2} \dfrac{\sin \theta_i}{\sin \varphi} & \text{(A.6)} \end{cases}$$

Combining equation A.5 and A.6 gives:

$$\frac{s_0 + R}{l_0} = \frac{n_2}{n_1} \frac{s_i - R}{l_i} \tag{A.7}$$

By only considering light rays having small angles with the optical axis, the so called paraxial approximation is used. Because φ is small, one can write:

$$\sin \varphi = \varphi \tag{A.8}$$

$$\cos \varphi = 1 \tag{A.9}$$

And therefore:

$$l_0 \approx s_0 \ \text{and} \ l_i \approx s_i \qquad \text{(A.10)}$$

So finally, equation A.7 gives, after rearranging the terms [45]:

$$\frac{n_1}{s_0} + \frac{n_2}{s_i} = \frac{n_2 - n_1}{R} \qquad \text{(A.11)}$$

At this point, it is important to introduce a sign convention; all the quantities as shown in Figure 81 are positive. This leads to the conventions summarized in Table 14. Most quantities are related to the point V, as defined in Figure 81, while other are related to the so called focal points, which are described in the next paragraph.

Table 14: Sign conventions for spherical refracting surfaces and thin lenses. [44]

Quantity	Symbol	Sign convention
Object position	s_0	+ left of V
Object focal length	f_0	+ left of V
Image position	s_i	+ right of V
Image focal length	f_i	+ right of V
Lens radius of curvature	R	+ if C is right of V
Object height	y_0	+ above optical axis
Image height	y_i	+ above optical axis
|Object focal point- object position|	x_0	+ left of the object focal point, F_0
|Image focal point- image position|	x_i	+ right of image focal point F_i

A.1.2   Focal points

If an object is placed in front the interface, four cases can be distinguished. Figure 82 (a) shows the case where the object is placed at infinity. The position where the image is located is then called the image focal point F_i and its distance to the point V the image focal length f_i. An expression for this length can be derived from equation A.11 as follows:

$$\frac{n_1}{\infty} + \frac{n_2}{s_i} = \frac{n_2 - n_1}{R} \qquad \text{(A.12)}$$

$$\Leftrightarrow f_i \triangleq s_{i,s_0=\infty} = \frac{n_2}{n_2 - n_1} R \qquad \text{(A.13)}$$

If the object is imaged at infinity, the object is per definition placed in the object focal point F_0 (Figure 82 (c)).The object focal distance is, by analogy:

$$\Leftrightarrow f_0 \triangleq s_{0,i=\infty} = \frac{n_1}{n_2 - n_1} R \qquad \text{(A.14)}$$

Figure 82 (b) shows the intermediate case, where the object is located between infinity and the object focal point. However, when the object is placed at the right of the focal point (Figure 82 (d)), the light rays in the second medium will not converge to a point as in (b). The diverging light can be traced back to a point on the object side, which is called the virtual image point. [44], [45]
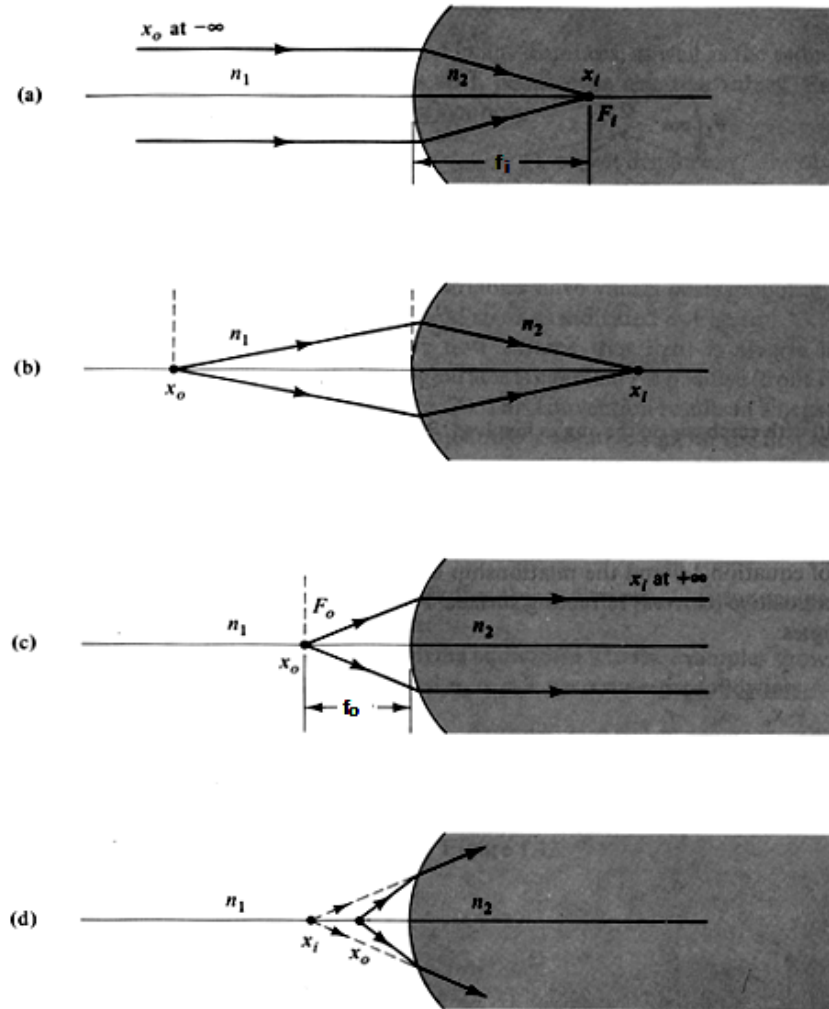
Figure 82: Influence of the object position. [45]

A.1.3 Lenses

When talking about lenses, the above theory has to be extended for two refracting interfaces. Different kind of lenses exists, ranked into two major groups. The first group, which contains the converging or convex lenses, has an increased thickness in the center and will tend to concentrate the incident light rays. On the contrary, concave or diverging lenses are thinner at the center and will diverge the light.

Consider a lens of refraction index n_l, inserted in a medium of lower index n_m (Figure 83). Because the object point S is situated on the left of the object focal point of the first interface, a virtual image point P' will be formed on the object side at a distance s_{i1}. This point will serve as object point at distance s_{o1} for the second lens, forming an image in point P. With the sign conventions summarized in Table 14, s_{i1} appears to be negative, because it is located on the object side of the interface. Therefore, one can write:

$$s_{02} = -s_{01} + d \tag{A.15}$$

Equation A.11, applied on both interfaces yields:

$$\frac{n_m}{s_{01}} + \frac{n_l}{s_{i1}} = \frac{n_l - n_m}{R_1} \tag{A.16}$$

$$\frac{n_l}{-s_{01} + d} + \frac{n_m}{s_{i2}} = \frac{n_m - n_l}{R_2} \tag{A.17}$$
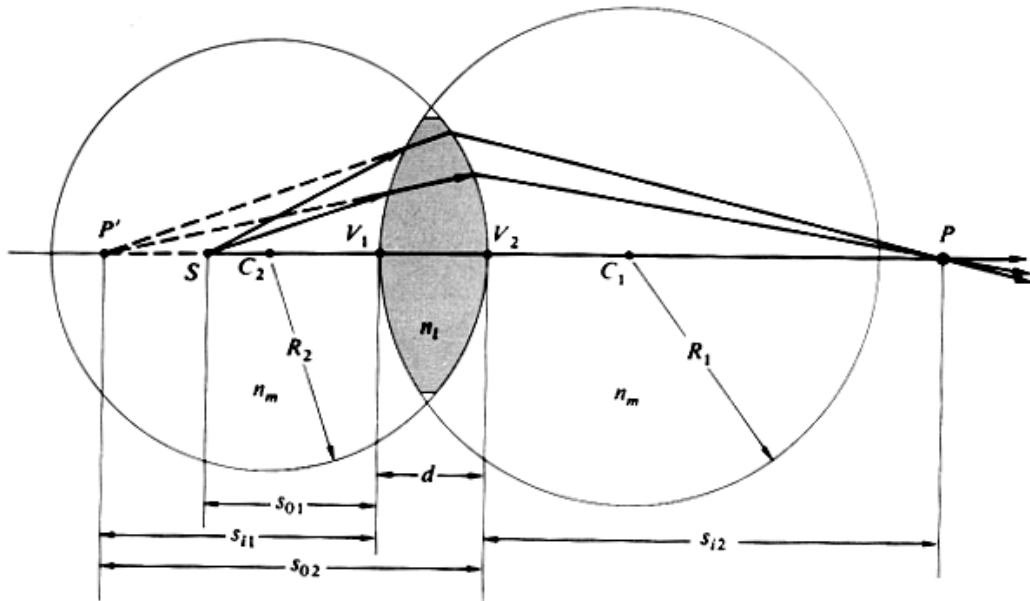
Figure 83: Image forming for a spherical lens. [44]

Combining these equations, assuming thin lenses ($d \rightarrow 0$) and taking air to be the surrounding medium ($n_m = 1$) gives so called the tin-lens equation:

$$\frac{1}{s_{01}} + \frac{1}{s_{i2}} = (n_l - 1)(\frac{1}{R_1} - \frac{1}{R_2})$$

(A.18)

Substituting the definition of object- and image focal length in the previous equation yields that $f_i = f_0$. With the Gaussian lens formula:

$$\frac{1}{s_{01}} + \frac{1}{s_{i2}} = \frac{1}{f}$$

(A.19)

equation A.18 can be simplified:

$$\frac{1}{f} = (n_l - 1)(\frac{1}{R_1} - \frac{1}{R_2})$$

(A.20)

A.1.4   Effect of a finite light source

The above theory presumed a point source, but in reality the source will have finite dimensions. To find the image of the source, the image of all source points has to be located. This is graphically easily done for thin lenses, which can be replaced by their center plane. When the positions of the focal points are known, three rays can easily be found to link the each object point with his image. The first one is the undeviated ray trough O. Two other rays are found by expressing that a ray, passing through a focal point will exit the lens at the other side parallel with the optical axis (Figure 84). When the image if found, the magnification M can be defined:

$$M = \frac{y_i}{y_0}$$

(A.21)

With the sign conventions made in Table 14, a positive magnifications denotes an erect image and a negative magnification an inverted image. Whether the image is minified or magnified depends on the object location. A summary of the possibilities is given in Table 15.
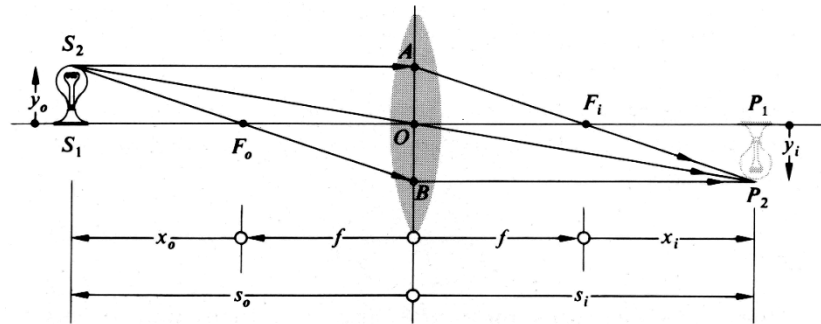
Figure 84: Image location for a thin lens. [44]

Table 15: Imaging characteristics of thin lenses. [44]

Convex lenses				
Object location	**Image type**	**Image location**	**Image orientation**	**Relative image size**
$\infty > s_0 > 2f$	Real	$f < s_i < 2f$	Inverted	Minified
$s_0 = 2f$	Real	$s_i = 2f$	Inverted	Same size
$F < s_0 < 2f$	Real	$\infty > s_i > 2f$	Inverted	Magnified
$s_0 = f$		$\pm\infty$		
$s_0 < f$	Virtual	$|s_i| > s_0$	Erect	Magnified

Concave lenses				
Object location	**Image type**	**Image location**	**Image orientation**	**Relative image size**
Anywhere	Virtual	$|s_i| < |f|$	Erect	Minified

A.2   Stops

Because of the finite dimensions of a lens, only a part of the light emitted by a source will be collected. Similarly, also other elements can block a part of the emitted light and thus determine which rays will pass the system to form an image. Such an element is called an aperture stop. Its diameter determines the number of rays from a certain object point that reach their image point, and thus the amount of irradiance in the image (Figure 85).

Another kind of stop, also shown on Figure 85, is the field stop. This element limits the size of the object that can be imaged, which is often necessary in order to obtain a good image quality.
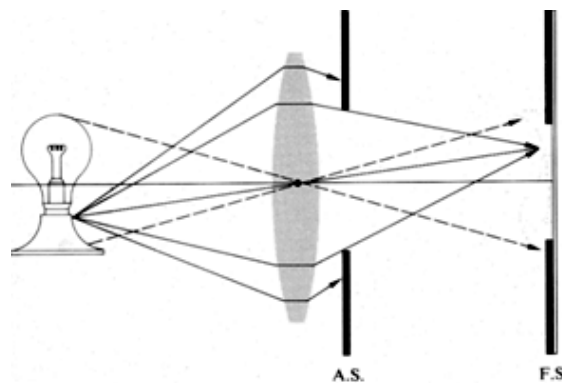

Figure 85: Aperture stop (A.S.) and Field stop (F.S.). [44]

Not only the aperture stop itself is an important concept in optics, also its image is meaningful. The image of the aperture stop, as seen from an axial point on the object through the optical elements placed ahead this stop, is called the entrance pupil. Similarly, the exit pupil is the image of the aperture stop, as seen from an axial point on the image plane. Obviously, when no optical components are placed between the aperture stop and the image, the aperture stop itself will serve as the exit pupil. The same applies for the entrance pupil, if nothing is placed between the stop and the object (Figure 86, Figure 87).
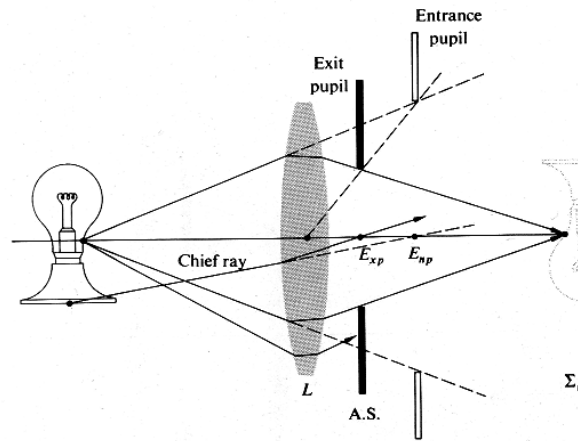

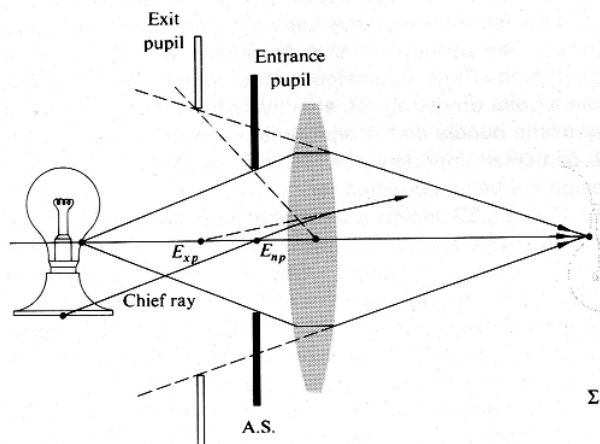**Figure 86:** Entrance and exit pupils for a rear aperture stop. [44]

Figure 87: Entrance and exit pupils for a front aperture stop. [44]

Both figures contain a so called chief ray. This is a ray, coming from an off-axis object point which passes through the center of the aperture stop. Furthermore, the chief ray enters the optical system along a line directed towards the midpoint of the entrance pupil, and leaves the system along a line that contains the middle of the exit pupil. This ray, also called the principal ray, is the central ray of the whole bundle and is especially useful in the analysis of aberrations.

A large entrance pupil, as shown on Figure 87, will allow the lens or mirror to gather a large amount of energy. To be precisely, the pupil diameter and energy amount have a directly proportional relation. Neglecting losses, this energy will be spread across the image. The energy per unit area per second, i.e. the flux density, will be inversely proportional to the image size, whereof it can be shown that it is proportional with the square of the focal length. Therefore, if the entrance pupil is circular, the flux density in the image plane will vary as $(\frac{D}{f})^2$. The square root of this quantity, $\frac{D}{f}$ is called the relative aperture, dough its inverse, the f-number $f/\#$ is more often used:

$$f/\# = \frac{f}{D} \tag{A.22}$$

A.3 Mirrors

A.3.1 Planar Mirrors

Consider a point source that sends spherical light waves towards a plane mirror (Figure 88). Using some basic goniometry, the image location can easily be found. Because of the law of reflection, which says that the incident angle ϑ_i equals the reflection angle ϑ_r, it is clear that $|s_0| = |s_i|$. Thus, the object and image are equidistant from the mirror surface.
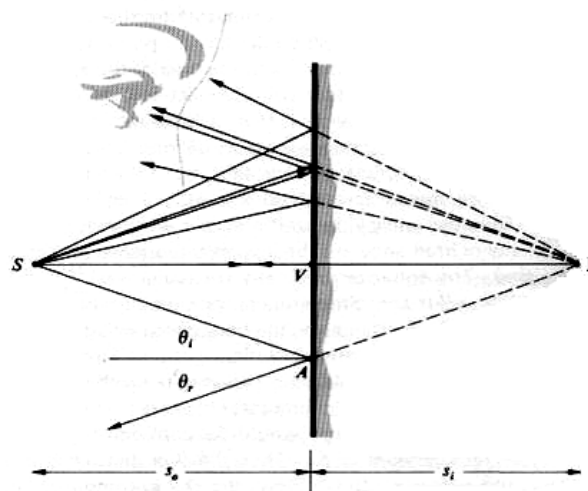
Figure 88: Reflection on a plane mirror. [44]

Unlike the sign conventions made for lenses, here s_0 and s_i are chosen to be positive if located on the object side of V. This choice leads to a positive magnification M for an erect image, like in the case of lenses.

A.3.2 Curved Mirrors

As for lenses, different kinds of interfaces are possible for mirrors. Suppose an incident plane wave has to be reflected into a converging spherical wave (Figure 89). Therefore, the optical path length for all rays must be equal:

$$W_1 A_1 + A_1 F = W_2 A_2 + A_2 F \tag{A.23}$$

For a plane Σ parallel to the incident wavefronts one can write:
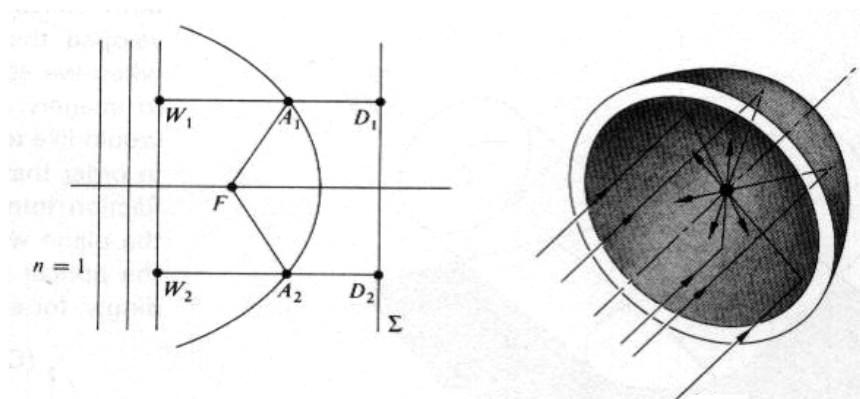
$$W_1 A_1 + c + A_2 D_2 \tag{A.24}$$

Figure 89: Reflection from a curved mirror. [44]

Thus, incident plane waves will be converged when they are reflected from a surface wherefore $A_n F = A_n D$, i.e. from a parabolic surface. Both convex and concave parabolic mirrors exist and have similar characteristics as observed for lenses. These characteristics are listed in Table 16 and illustrated in Figure 90.

Table 16: Imaging characteristics of curved mirrors. [44]

Concave mirrors				
Object location	**Image type**	**Image location**	**Image orientation**	**Relative image size**
Anywhere	Virtual	$|s_i| < |f|$	Erect	Minified

Convex mirrors				
Object location	**Image type**	**Image location**	**Image orientation**	**Relative image size**
$\infty > s_0 > 2f$	Real	$f < s_i < 2f$	Inverted	Minified
$s_0 = 2f$	Real	$s_i = 2f$	Inverted	Same size
$F < s_0 < 2f$	Real	$\infty > s_i > 2f$	Inverted	Magnified
$s_0 = f$		$\pm\infty$		
$s_0 < f$	Virtual	$|s_i| > s_0$	Erect	Magnified

Concave

Convex
$\infty > s_0 > 2f$

Convex
$s_0 = 2f$

Convex
$F < s_0 < 2f$

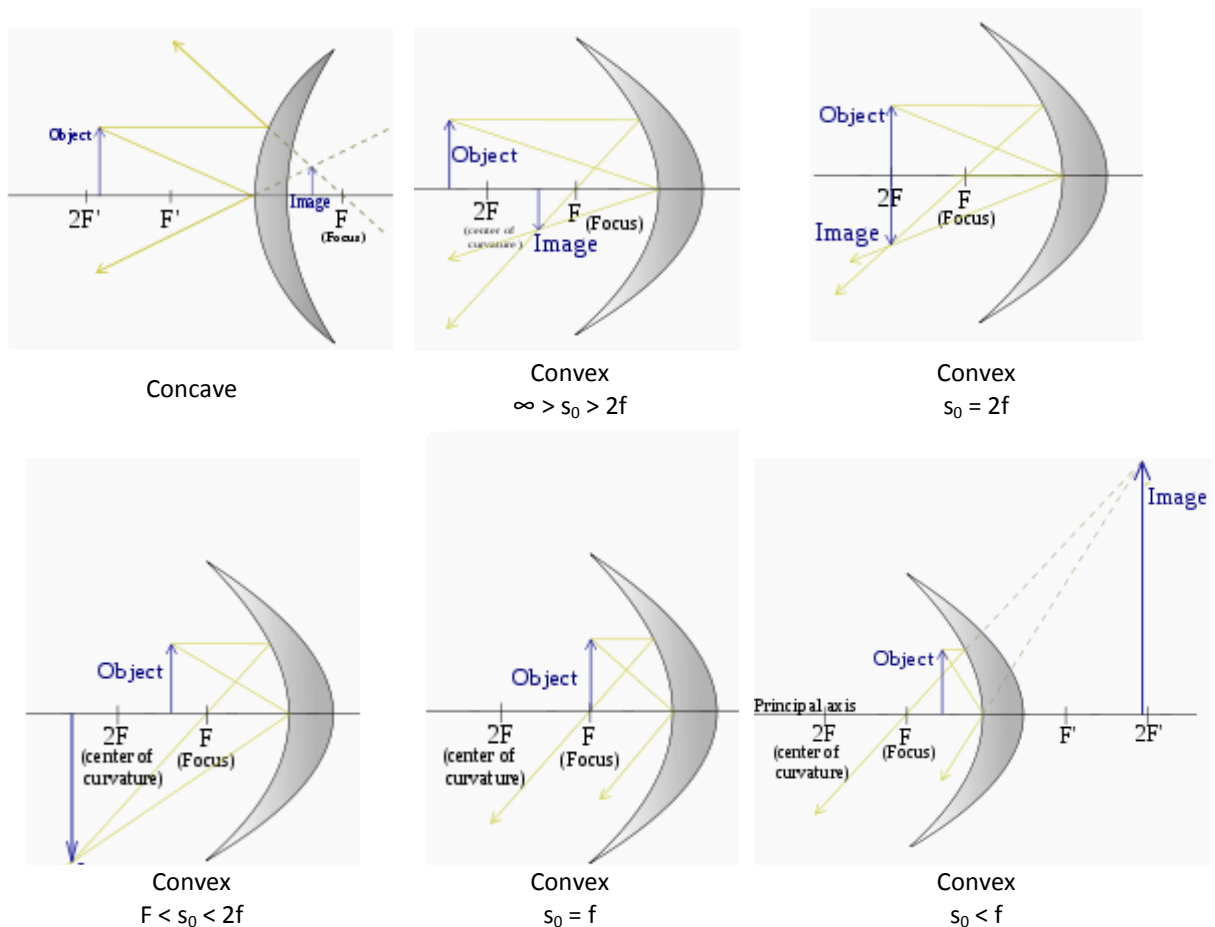Convex
$s_0 = f$

Convex
$s_0 < f$

Figure 90: Imaging characteristics for curved mirrors.[46]

A.4 Aberrations

In the theory developed above, the paraxial approximation was used. However, reality deviates from this approximation, and these aberrations have to take into account. Two major groups of aberrations exist: chromatic aberrations arise from the fact that the refractive index varies with the frequency of the incident light, where monochromatic aberrations also occur when the light is monochromatic.

A.4.1 Monochromatic aberrations

Monochromatic aberrations can be divided into two subcategories. The first category exists of the aberrations which make the image unclear, such as spherical aberration, coma and astigmatism. Other aberrations deform the image, as for example distortion and Petzval field curvature.

A.4.1.1 Spherical aberration

Spherical aberration is caused by a variation in focal length for nonparaxial rays. As shown in Figure 91, the marginal rays are bent stronger, so that they will cross each other in a point ahead of the focal point. The distance between this intersection and the focal point is called the longitudinal spherical aberration (L.SA). The height above the optical axis of a given ray, at the focal point position is known as the transverse spherical aberration (T.SA).
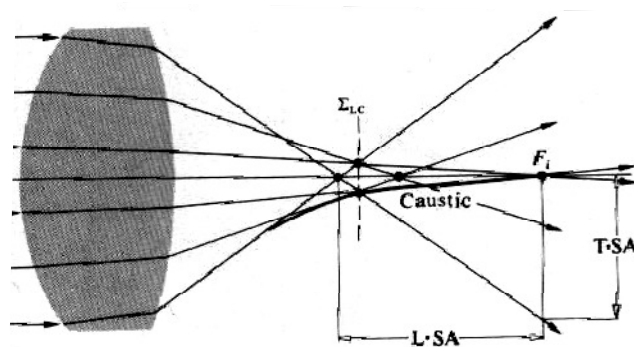

Figure 91: Spherical aberration for a lens. [44]

Spherical aberration can evidently be reduced by minimizing the aperture. But because this also reduces the amount of light entering the system, other solutions have to be thought of. When aperture and focal length are fixed, the amount of aberration varies with the object distance and lens shape. It can be shown that the deviation will be minimal when the incident ray makes approximately the same angle as the emerging ray. When the object is placed at infinity, a simple lens with almost flat rear side will yield a minimum aberration. However, if the object and image distances are to be equal, the lens should be equiconvex.

A.4.1.2 Coma

When the object is placed off-axis, coma can occur. This aberration is due to the fact that the magnification depends on the height at which the ray crosses the lens. When the marginal rays reach the image plane in a point, closer to the optical axis than the principal ray does, the coma is said to be negative (Figure 92 (a)).The magnification is the least for these outer rays and the corresponding image will be smaller than for the other rays. When the opposite is true, one speaks about positive coma (Figure 92 (b)).

Because of its asymmetric behavior, coma must tried to be avoid. The amount of coma is proportional to the offset angle, and like spherical aberration, dependent on the shape of the lens. When the object is placed at infinity, a concave meniscus lens will have a large negative coma. The coma diminishes when the lens becomes planar-convex and is almost zero for a convex-planar lens. Further bending of the lens to a convex-meniscus lens will lead to a large positive coma. When coma has to be minimized for an optical

configuration where the object is placed at a finite distance, a system of lenses can to be used in order to obtain the desired focal length and conjugate points.
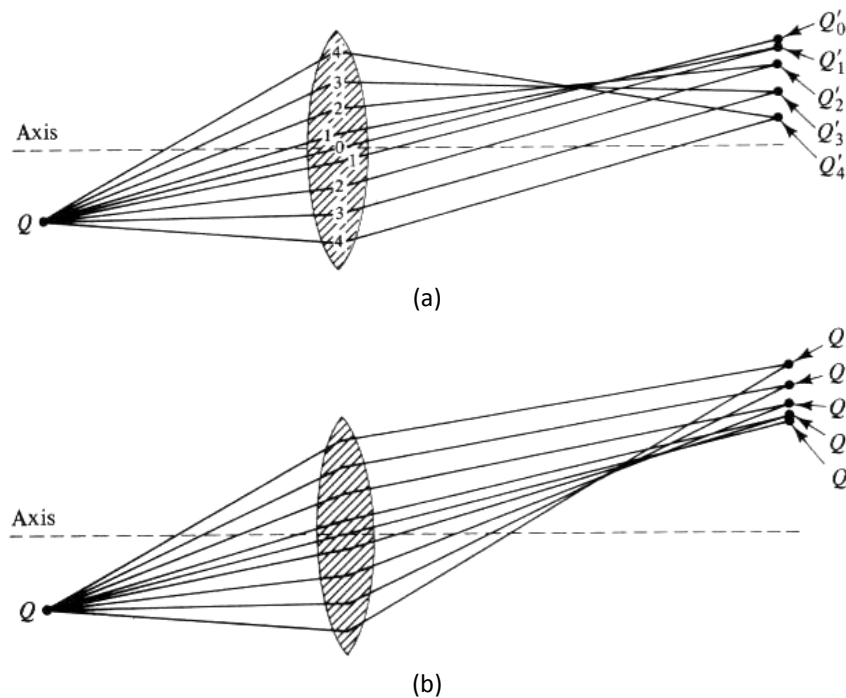

(a)

(b)

Figure 92: (a) Negative coma, (b) Positive coma. [44]

A.4.1.3 Astigmatism

When the object is located on an appreciable distance from the optical axis, a third monochromatic aberration, called astigmatism, occurs. The incident cone of rays will strike the lens asymmetrically. The plane that contains both the principal ray and the optical axis is called the meridional or tangential plane. The plane perpendicular to the meriodional plane, passing through the principal ray is the sagittal plane. Rays propagating in the meriodional plane will focus on a different point that the rays in the sagittal plane will do. These focal points are respectively called the tangential focus (F_T) and the sagittal focus (F_S) (Figure 93). For simplicity, consider the case where no spherical aberration and coma occurs. The initially circular cross section of the beam leaving the lens becomes elliptical until the tangential focus is reached. There, the ellipse degenerates into a line which is called the primary image. Moving further, the cross-section opens again and becomes a circle, known as the circle of least confusion. After this point, the cross section again deforms into a line, but this time aligned in the meridional plane. This line is called the secondary image and is located at the sagittal focus.
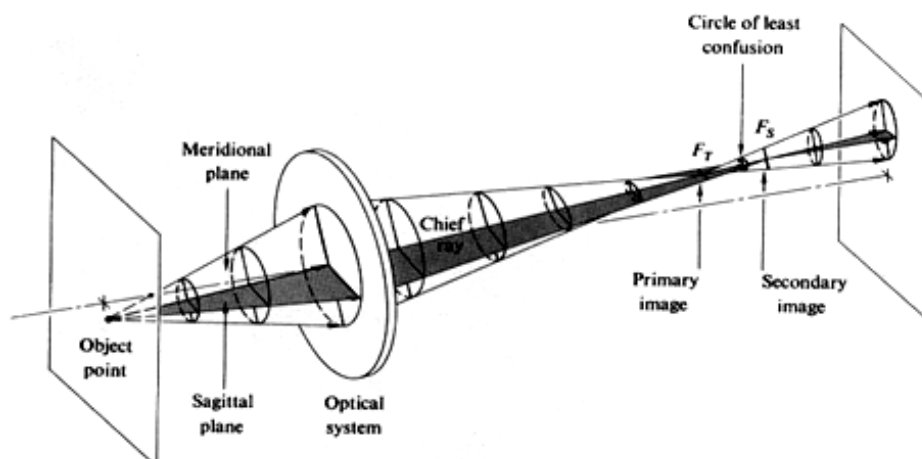

Figure 93: When the object is placed off axis, astigmatism occurs and a sagittal and tangential focus is formed. [44]

The influence of astigmatism is again proportional to the offset angle; putting the object further off-axis increases the diameter of the circle of least confusion. The quality of the image will decrease, as the edges will become blurred.

A.4.1.4 Field curvature

Even when an optical system is free of all aberrations discussed above, a planar object normal to the optical axis would be imaged as a plane only in the paraxial region. At finite apertures, the image will be curved because of the Petzval field curvature. A spherical segment σ_0 will be imaged as a spherical segment σ_i, but flattening out the object to a plane σ_0' will form a paraboloidal surface Σ_P, called the Petzval surface. Because the Petzval surface curves inward for a positive lens and outward for a negative, a proper combination of lenses can eliminate the field curvature.
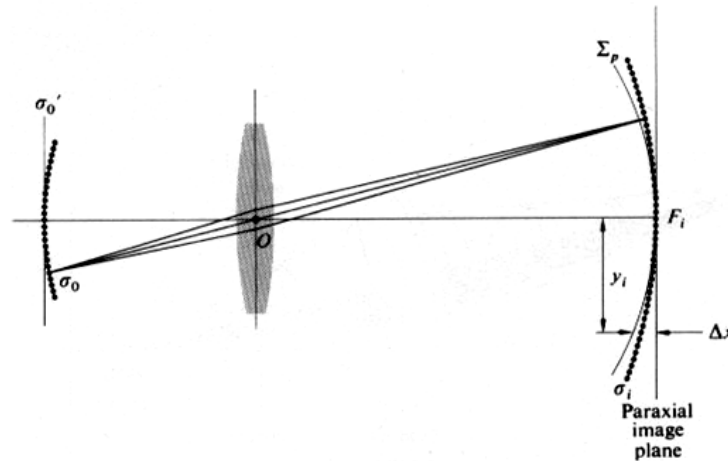

Figure 94: Field curvature causes an object in a flat plane σ_0' to be imaged on a paraboloidal surface Σ_p.

A.4.1.5 Distortion

The last of the five monochromatic aberrations is called distortion. When no other aberrations are present, distortion causes a misshaping of the image, even though each point is sharply focused. It is caused by the fact that the magnification is a function of the vertical image distance y_i. When each image point is displaced radially outwards from the center, whereby the most distant points have the largest displacement, one speaks about positive or pin-cushion distortion. Similarly, when the points move radially inwards the center and MT decreases with axial distance, the aberration is called negative or barrel distortion (Figure 95).
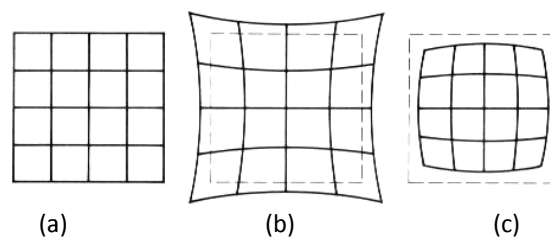

| (a) | (b) | (c) |

Figure 95: An object (a) can be misshaped by (b) pin-cushion distortion, (c) barrel distortion. [44]

A.4.2 Chromatic aberrations

Chromatic aberrations arise from the fact, that the thin-lens equation, predicting the focal length of lens (equation A.20) is dependent of the index of refraction, which on his turn is function of the wavelength of the incident light. Because the refractive index decreases with increasing wavelength, the focal length will increase as well. Therefore, the different colors in a beam of light will be focused in different point, as shown in Figure 96. Furthermore, for an off-axis object point, the focal points associated with different wavelengths will be positioned at different heights above the optical axis (Figure 97). Therefore, a lens

with chromatic aberration, illuminated with white light will produce an area, consisting of overlapping images with different size and colors. [44], [45]
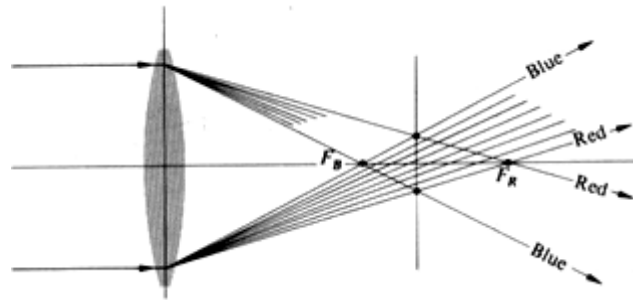

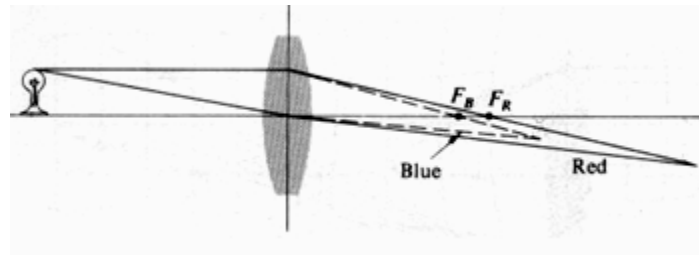**Figure 96:** Chromatic aberration. [44]

Figure 97: Chromatic aberration for an off-axis object. [44]

Appendix B: CD contents

The attached CD contains all discussed Schlieren and PIV measurements. For the Schlieren measurements, the name of each AVI file contains information about the visualized state (transient/steady), the configuration of the pipe (open/closed) and the mouth geometry (mouth width W and labium angle).

Name file	Discussed in paragraph	Image shown on page nr
Transient_Square_Open_W16_labium10	5.3.1.1 Transient State	48-49
Transient_Sine_Open_W16_labium10	5.3.1.1 Transient State	48-49
Transient_Saw_Open_W16_labium10	5.3.1.1 Transient State	48-49
Transient_Square_Stopped_W25_labium10	5.3.1.1 Transient State	50-51
Transient_Sine_Stopped_W25_labium10	5.3.1.1 Transient State	50-51
Transient_Saw_Stopped_W25_labium10	5.3.1.1 Transient State	50-51
NoSound_W23_labium10	5.3.1.2.1 Open pipe	53
Steady_Open_W16_labium10	5.3.1.2.1 Open pipe	54
Overblow_open_W9_labium10	5.3.1.2.1 Open pipe	55
Steady_Open_W18_labium20	5.3.1.2.1 Open pipe	56
Steady_Open_W13_labium30	5.3.1.2.1 Open pipe	58
Steady_Stopped_W26_labium10	5.3.1.2.2 Stopped pipe	59
Steady_Stopped_W26_labium20		
Steady_Stopped_W26_labium30		
PIV_LowSpeed	5.3.2. PIV measurements	61
PIV_Sound	5.3.2. PIV measurements	62